Dissertation

submitted to the

Combined Faculty of Natural Sciences and Mathematics
of Heidelberg University, Germany

for the degree of

Doctor of Natural Sciences

Put forward by

Dominick Cichon
born in: Mannheim, Germany

Oral examination: 20 January 2021

Liquid xenon detector physics with XENON1T and HeXe

Electric noise stability, background discrimination studies and measurements of the scintillation pulse shape

Referees: PD Dr. Teresa Marrodán Undagoitia
Prof. Dr. Stephanie Hansmann-Menzemer

Zusammenfassung

Verflüssigtes Xenon (LXe) ist ein beliebtes Detektionsmedium bei Experimenten, die nach seltenen Ereignissen suchen, die von über das Standardmodell hinausgehenden Theorien vorhergesagt werden. Unter anderem wird es in Zwei-Phasen-Zeitprojektionskammern (TPCs) von Experimenten wie XENON1T verwendet, die versuchen, Wechselwirkungen von Dunkle-Materie-Teilchen sowie den neutrinolosen Doppel-Beta-Zerfall zu messen. Ein genaues Verständnis der Prozesse hinter der Signalen solcher Detektoren ist dabei nötig, um störende Untergrundereignisse von den gesuchten Signalen so gut wie möglich trennen zu können.
In dieser Arbeit werden Analysen vorgestellt, die sich mit der Physik von LXe TPCs befassen. Im ersten Teil wird für das XENON1T-Experiment die zeitliche Entwicklung elektrischer Störsignale betrachtet. Weiterhin wird ein Auswahlkriterium, das entwickelt wurde, um Wechselwirkungen, die in der Gasphase der TPC stattfinden, auszuschließen, auf höhere Energieskalen erweitert. Zuletzt wird untersucht, ob die Pulsform des LXe-Szintillationslichts es erlaubt, zwischen Kernrückstoß-Interaktionen und Elektronrückstoß-Untergrundereignissen, die von Zerfällen in oder auf den Reflektorpanelen der TPC verursacht werden, zu unterscheiden. Die Pulsform ist auch Thema des zweiten und letzten Teils. Hier wird sie mit Hilfe der TPC des HeidelbergXenon-Systems (HeXe) für Konversionselektronen aus Zerfällen von ^{83m}Kr sowie für α-Teilchen aus den Zerfällen von ^{222}Rn und dessen Töchtern in Abhängigkeit von der elektrischen Feldstärke gemessen.

Abstract

Liquefied xenon (LXe) is a popular detection medium for experiments searching for rare interactions proposed by beyond the Standard Model theories. It is employed in dual-phase time projection chambers (TPCs) used by experiments such as XENON1T, which attempt to measure particle dark matter interactions as well as the neutrinoless double-beta decay. A precise understanding of the processes behind the signals of such detectors is necessary to discriminate between background and signal events as well as possible.
This work presents analyses regarding LXe TPCs physics. In the first part, the temporal evolution of electric noise in the XENON1T experiment is examined. Furthermore, a selection criterion, which has been developed to exclude interactions happening in the TPC's gas phase, is extended to higher energy scales. Finally, it is investigated whether the LXe scintillation pulse shape allows to discriminate between nuclear recoils and background electronic recoils which originate from decays in or on TPC reflector panels. The pulse shape is also the topic of the second and final part. There, its electric field strength dependence is measured, using the TPC of the HeidelbergXenon (HeXe) system, for conversion electrons coming from ^{83m}Kr decays as well as for α-particles from decays of ^{222}Rn and daughters.

To my family and friends.

Contents

1 Introduction

Detectors employing liquid xenon (LXe) as a target medium are popular tools in searches for physics beyond the Standard Model (BSM), particularly regarding both the nature of dark matter and the mechanism by which neutrinos acquire mass. The utilization of such detectors for measuring rare interactions predicted by the aforementioned BSM physics provides the greater context for the work featured in this thesis.

This introductory chapter provides information necessary for motivating and understanding the main analyses of this work, which are presented in Chapters 3 and 6. Section 1.1 contains brief summaries illustrating the concepts behind dark matter and the neutrinoless double-beta decay, which are both being searched for with LXe detectors such as XENON1T (Chapter 2). Section 1.2 details the microphysics involved in interactions with LXe and gives an explanation to why it is well-suited for detecting rare processes. It also describes the working principle of a dual-phase LXe time projection chamber (TPC), which is the type of detector to which the setups utilized in this work and specified in Chapters 2 and 4 belong to.

For additional information about LXe detectors in particle physics, the reader is referred to [1, 2].

1.1 The search for new physics

1.1.1 Dark matter

Up to now, several astrophysical observations have been made which suggest the presence of non-luminous, non-baryonic matter in the universe which makes up about 84 % of the total matter content [3]. It is called *dark matter*. While, at the time of writing, only indirect evidence exists, the inferred properties of dark matter strongly point towards BSM physics.

Hints towards the existence of dark matter were already found during the early 20th century. It has been observed by Fritz Zwicky, for example, that the galaxies which make up the Coma Cluster move so fast, that the mass inferred from luminous matter would be insufficient to keep the cluster gravitationally bound [4]. During the late 1970s and early 1980s, Vera Rubin and colleagues measured the rotation curves of spiral galaxies and made a similar observation [5, 6]. According to Newtonian gravity, one would expect the orbital velocity of a star on a circular trajectory at a distance r to the galactic center to be proportional to $r^{-1/2}$ if the bulk of the luminous mass is within the orbit and if only visible matter is taken into account. However, the measured rotation curves do not decrease towards larger r as expected. Instead, they converge to a constant velocity and remain there even at large distances to the visible galactic matter, pointing towards an invisible matter component within which the visible matter is embedded, a *dark matter halo*.

Further observations which can also be explained by assuming the existence of dark matter allow to gain insight into the latter's properties. An example is the study of the matter distribution of the 1E 0657−558 galaxy cluster, also called *Bullet Cluster*. It is the result of a past merger between two galaxy clusters. Its matter distribution has been determined by measuring optical distortions induced by gravitational lensing, and by measuring the flux of X-rays emitted by the intracluster medium (ICM), which makes up most of the cluster's baryonic mass [7]. The distributions extracted from both approaches do not match as seen in Fig. 1.1.

with most of the cluster's mass being located in diffuse clouds at a significant distance to the ICM while being invisible in the optical and X-ray spectrum. In addition, the progenitor clusters can be made out in the mass distribution. Their ICM clouds interacted with each other during the collision and slowed down, making them lag behind the cluster galaxies as a result. This is, however, not the case for the invisible components, which seem to have passed through each other and the ICM clouds with no significant interactions. Accordingly, dark matter can only interact weakly with itself and baryonic matter. The only Standard Model particles which come into question are the three neutrinos and their antiparticles. As they do not interact electromagnetically, there are not subject to first-order interactions involving photons, which would explain the lack of light associated with dark matter. Furthermore, they only couple directly to the gauge bosons of the weak force, resulting in generally small interaction cross-sections compared to other Standard Model forces. However, results from N-body simulations regarding structure formation in the universe are incompatible when assuming dark matter to be made out of Standard Model

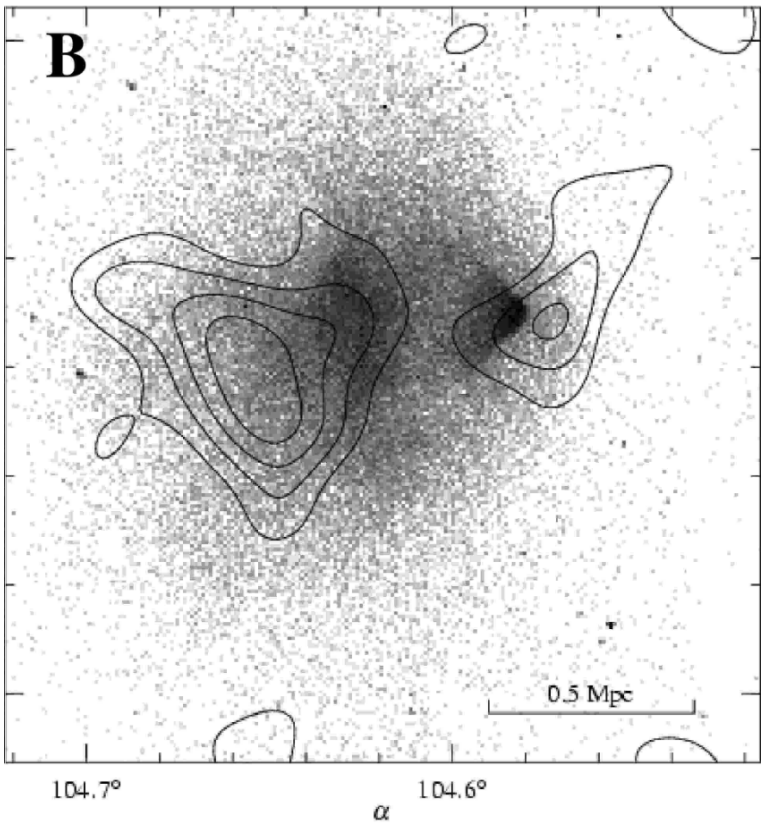

Figure 1.1: X-ray image of the bullet cluster in greyscale, overlaid with the mass distribution contours as inferred from gravitational lensing. Image taken from [**Clowe2004**.]

neutrinos [8]. Because neutrinos were produced at relativistic energies following the Big Bang, they would have influenced cosmological evolution to result in a larger scale of galaxy clustering than observed. As a consequence, there are no Standard Model particles fulfilling all criteria necessary to make up dark matter.

The perhaps most striking evidence for BSM physics being involved in dark matter lies within the fluctuations of the cosmic microwave background (CMB). Its angular power spectrum, determined by quantum fluctuations after the Big Bang, interactions between particles in the primordial universe and cosmological evolution, is explained well by the ΛCDM model [3]. This model postulates the existence of new kinds of non-baryonic particles produced at non-relativistic speeds after the Big Bang. A promising class of candidates for such particles are *weakly interacting massive particles (WIMPs)*, which range in mass between $\mathcal{O}(1\,\mathrm{GeV})$ and $\mathcal{O}(1\,\mathrm{TeV})$ [9]. Such particles are predicted by popular BSM models which have initially been conceived to solve particle physics problems unrelated to dark matter, such as supersymmetry (SUSY) [10]. Following the ΛCDM interpretation, the contribution of dark matter to the total energy content of the universe must correspond to $\sim 27\,\%$ to result in the CMB as observed today. When assuming a self-annihilation cross-section at the order typical for weak interaction processes and assuming a dark matter particle mass of $\mathcal{O}(100\,\mathrm{GeV})$ yields the same result for the amount of relic dark matter present in today's universe [9]. As this is consistent with the properties of WIMPs, this coincidence is sometimes called the *"WIMP miracle"*.

The detection of WIMPs can be, in principle, accomplished in three different ways. One of them is to search for Standard Model particles which are expected to be produced during WIMP annihilation, such as γ-rays, electrons and positrons. This approach is called *indirect detection* and involves experiments measuring cosmic rays and photons. Another approach is *collider production*, i.e. producing WIMPs via particle collisions. The third method is called *direct detection* and aims to detect interactions of WIMPs with Standard Model particles. Because the solar system is embedded within the Milky Way's dark matter halo, a non-zero flux of particle dark matter on earth is expected. WIMPs are predicted to preferably interact with nucleons by recoiling elastically off them. The differential interaction rate dR/dE_R for an observer stationary relative to the halo is approximately given by [12]:

$$\frac{dR}{dE_R}(E_R) \approx \frac{R_0}{E_0 r}\, F^2(E_R)\ \exp[-E_R/(E_0 r)], \tag{1.1}$$

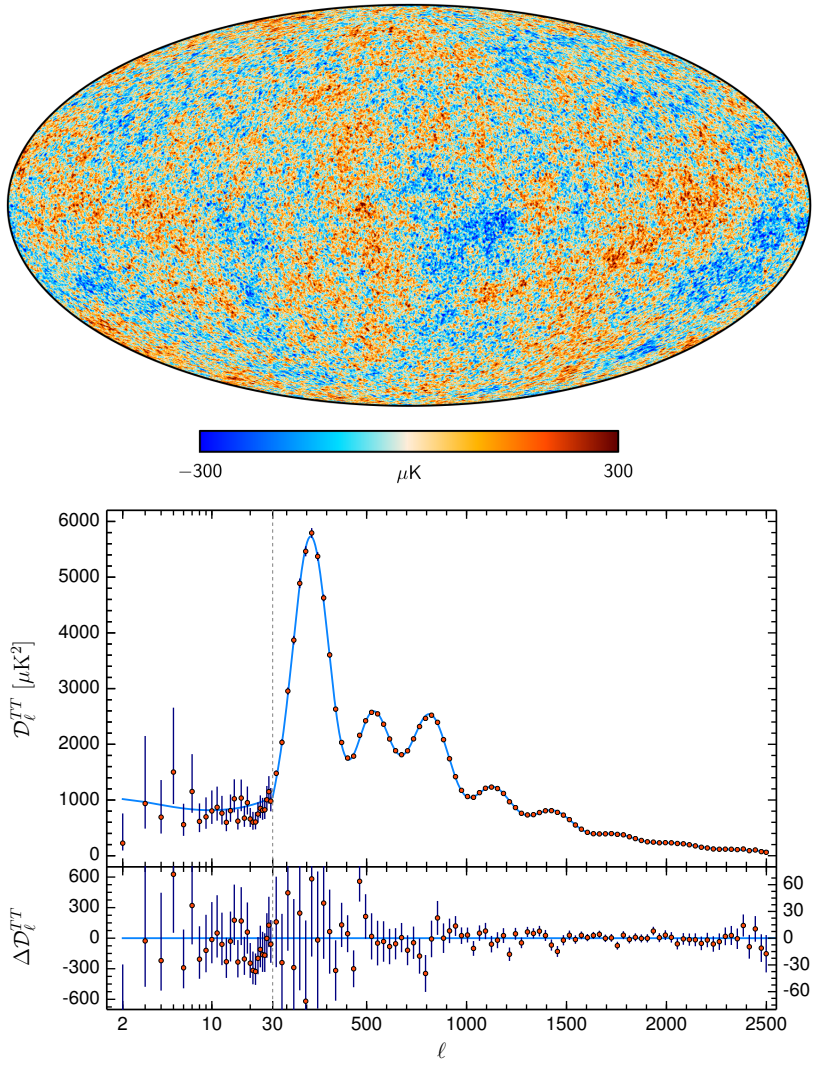

Figure 1.2: Top Planck 2018 temperature map of the CMB (taken from [11]). Bottom: Fit of the ΛCDM model to the angular power spectrum of the map above (taken from [3]).

with E_R being the energy of the recoiling nucleus, E_0 the most probable incident particle energy, $r = 4m_\chi m_t/(m_\chi + m_t)^2$ a kinematic factor which includes the dark matter particle mass m_χ and the target nucleus mass m_t, and $F^2(E_R)$ a nuclear form factor to correct for the spatial extent of the target nucleus. According to the equation above, one expects a purely exponential recoil energy spectrum modulated by the target nucleus form factor.

For a WIMP with a cross-section corresponding to the one obtained in the "WIMP miracle", the expected rate is. As the rate is so low, it is imperative for direct detection experiments to precisely model and minimize background radiation.

1.1.2 Neutrinoless double-beta decay

One of the currently investigated questions in the field of neutrino physics regards the fundamental nature of neutrinos themselves [13], which would give insight into the mechanism via which they acquire mass. It is either possible for them to be *Dirac* or *Majorana* fermions, with the former corresponding to fermions described by the Dirac equation (as all other Standard Model fermions). The latter correspond to fermions described by the Majorana equation, which are their own antiparticles. Were neutrinos confirmed to be Majorana fermions, it would be possible for their masses to result from the *seesaw mechanism*. This mechanism would give an explanation for why neutrinos are significantly less massive compared to other Standard Model fermions.

As neutrinos being their own antiparticles would allow for processes which violate lepton number conservation, one way to test the Majorana fermion hypothesis is to search for such processes. One of them is the *neutrinoless double-beta decay*, which is analogous to the observed two-neutrino double-beta decay from the Standard Model. The difference is, that no neutrinos are emitted along the two β-particles as the neutrino lines are connected in the corresponding Feynman diagram.

A potential nuclide to undergo neutrinoless double-beta decay is ^{136}Xe, which is utilized by the EXO-200 experiment [14]. At the time of writing, no observation of neutrinoless double-beta decay has been reported.

1.2 Detecting particles with liquid xenon

1.2.1 Properties and particle interaction microphysics

Xenon, the heaviest stable noble gas, possesses a multitude of properties[1] in its liquid state which make it useful for detecting particle interactions. Among them is its high nuclear charge of $Z = 54$, which, together with a density of about $2.9\,\mathrm{g/cm^3}$, results in a large stopping power especially for charged particles. With a liquefaction temperature of about $-108\,^\circ\mathrm{C}$, it is less challenging to keep xenon in its liquid state compared to other liquefied gases, such as argon, which liquefies at roughly $-186\,^\circ\mathrm{C}$. It is also easier to maintain a large, homogeneous detection volume with LXe compared to, for example, crystal-based scintillators.

Further advantages of using LXe become clear when examining the microphysics responsible for signal generation, summarized in [16] and depicted in Fig. 1.3. When a particle interacts with either the nucleus or one of the shell electrons of a xenon atom, the latter can be ionized or excited, with the average energy to produce a quantum (either ionization or excitation) being $\sim 13.7\,\mathrm{eV}$ [17]. It is energetically favorable for an excited xenon atom to form a dimer with another xenon atom. This results in the formation of an excited dimer, or *excimer*. The different possible spin orientations of the excimers' outer electron yield two possible excimer states: a *singlet state*, or a *triplet state* (usually denoted as ${}^1\Sigma_u^+$ respectively ${}^3\Sigma_u^+$ in literature) [18]. In the singlet state, the optically active electron couples to the remaining dimer shell electrons to yield a total spin of $S = 0$, while in the triplet state they combine to $S = 1$. The singlet state can decay directly into the $S = 0$ ground state, as no change in total spin is involved. On the other hand, the triplet state would need to go through a forbidden transition with $\Delta S \neq 0$. It can still decay via spin-orbital coupling which mixes the singlet and triplet states. This results in the singlet state lifetime, which is usually cited as $\sim 3\,\mathrm{ns}$, being shorter than the one of the triplet state, which is roughly $\sim 25\,\mathrm{ns}$. Both states decay under radiative disassociation of the excimer, emitting a vacuum-ultraviolet (VUV) photon. The photon emission spectrum peaks at a wavelength of about 175 nm [19]. Because the energy levels of the xenon dimer system differ from those of a single atom, there is no efficient re-absorption of the emitted light, making xenon transparent to its own scintillation light. In addition to the scintillation signal from excimer decay, ionization electrons provide an additional

[1] Chemical properties in the following are taken from [15] if not stated otherwise.

avenue to probe the amount of energy deposited if they escape recombination. As seen in Fig. 1.3, recombination yields excimers, which causes the charge and prompt scintillation signals to be correlated with each other. Experiments capable of measuring both achieve, as a consequence, an improved energy resolution compared to those which measure only one of them. In addition, the relative fraction of initially created electron-ion pairs and excited xenon atoms, as well as the recombination dynamics of the resulting electron-ion cloud, depend on the energy loss per unit length of a particle. Correspondingly, the ratio between the charge and the prompt scintillation signal allows to determine the particle which deposited its energy into the xenon.

Besides the signal ratio, another avenue for interaction type discrimination is the *pulse shape* of the prompt scintillation signal. The pulse shape is typically modelled by the following photon emission time probability density function:

$$p(t) = \frac{f_s}{\tau_s} e^{\frac{-t}{\tau_s}} + \frac{1 - f_s}{\tau_t} e^{\frac{-t}{\tau_t}}, \tag{1.2}$$

with the effective singlet fraction f_s and the effective singlet and triplet lifetimes τ_s respectively τ_t. Particles which experience a larger stopping power compared to other particles also cause denser tracks. Because recombination occurs faster the higher the ionization track density is, scintillation should occur faster compared to particles which cause less dense tracks. This also implies, that the pulse shape depends on electric field strength which affects recombination efficiency. Past measurements of electronic recoil (ER) interactions [18, 20, 21] indicate, that this is indeed the case. Even at zero field, different f_s values have been measured for α-particles and fission products, with the latter experiencing a higher stopping power in LXe compared to the former. It has been proposed by the scientists who made this measurements [22] that this could be caused by *superelastic collisions*, where free electrons scatter with singlet state excimers and convert them to the triplet state. This reaction would be favored when ion recombination is slow, as it is the case for particles which experience less stopping power.

1.2.2 Dual-phase time projection chambers

For detecting rare events such as particle dark matter interactions and the neutrinoless double-beta decay, TPCs which use xenon as a target have proven themselves to be a useful tool, managing to deliver competitive results. They achieve the latter by exploiting the properties of LXe, being able to reconstruct

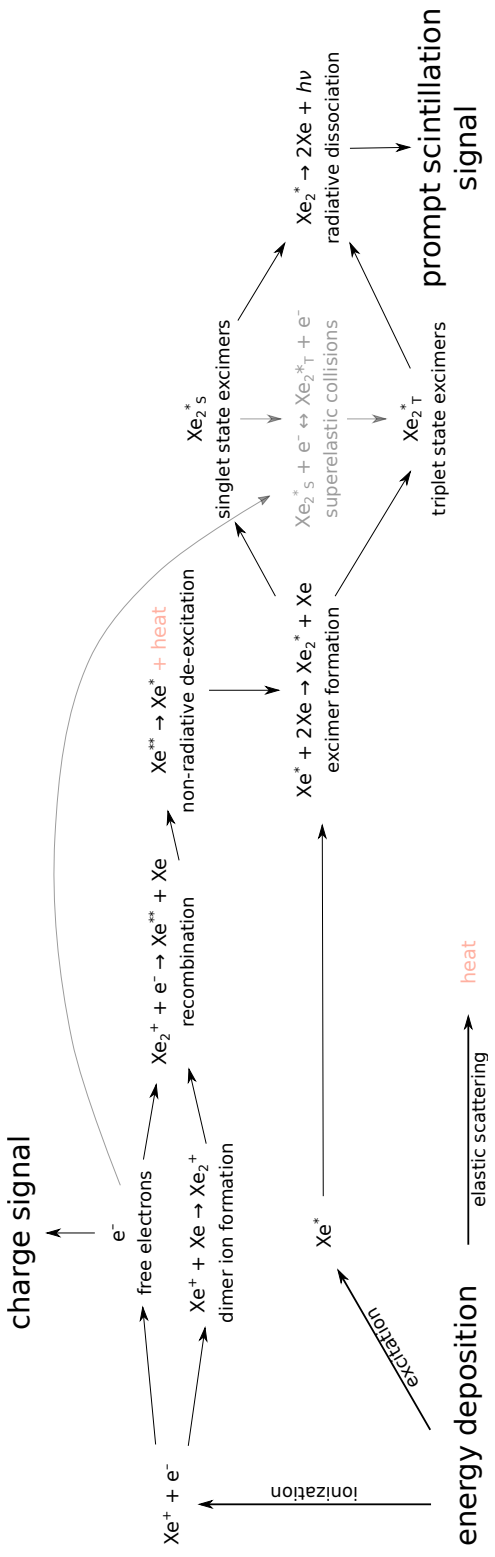

Figure 1.3: Diagram summarizing the microphysics involved in signal generation after a particle interacting with xenon. Losses in detectable energy are indicated by the corresponding components being colored in red.

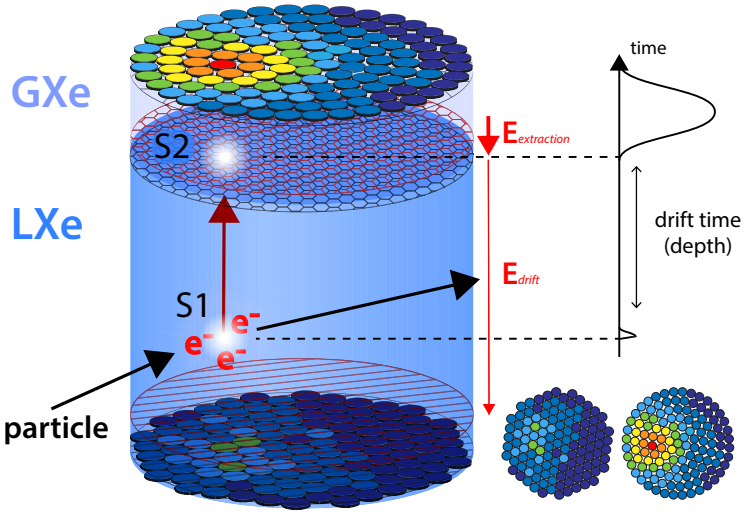

Figure 1.4: Diagram illustrating the working principle of a dual-phase LXe TPC. It depicts an incoming particle interacting with the LXe target, resulting in both prompt scintillation (S1 signal) and the generation of ionization electrons. The latter are drifted and extracted into the GXe phase via the fields generated by the indicated HV grids, and cause proportional scintillation (S2 signal). On top and bottom of the cylindrical volume, heatmaps indicate the amount of light seen per photosensor for this example interaction. On the right-hand side, a top-down view of the hit patterns and an example waveform show the information used for reconstructing the position of the interaction site. The figure is a variant of a diagram taken from [26], provided by the author of the cited work, and has been modified.

the position of an interaction and to discriminate between particle interaction types. The following paragraphs describe how particles are detected with a dual-phase LXe TPC, such as XENON1T [23], LUX [24] or PandaX-II [25]. In addition, a schematic displaying an example detector is shown in Fig. 1.4.

When a particle interacts with the xenon target, both excimer formation and ionization occur. Photons from the radiative deexcitation of the former make up the prompt scintillation signal, called *S1*. Ionization electrons which escape recombination are drifted by an electric field, the *drift field*, towards the liquid-gas interface. Another, stronger field in the interface region, the *extraction field*, accelerates the electrons into the GXe phase. There, they cause proportional scintillation by inelastically scattering with the xenon atoms therein, which

makes up the *S2* signal. Both S1 and S2 signals are detected by photosensors capable of sensing VUV light and converting it into a charge. As these sensors utilize the photoelectric effect for conversion, charge is given in units of PE, the average charge generated when a photoelectron is created. The duration of each scintillation signal allows to distinguish between S1 and S2 signals. The former occur on a timescale of $\mathcal{O}(10\,\mathrm{ns})$, which is the scale of the triplet excimer state, while the latter have a duration of $\mathcal{O}(1\,\mu\mathrm{s})$ due to diffusion of the ionization electron cloud on its way towards the amplification region and the timescale of the amplification process itself.

Because the S2 signal is delayed relative to the S1 signal by the time the ionization electrons need to drift, the delay time allows to determine the position of the initial interaction along the drift field axis. Sensor hit patterns of the S2 signal are used to determine the two remaining coordinates, allowing for 3D position reconstruction. Caused by the high stopping power of LXe, the inner TPC volume is shielded by the outer ones, also called *self-shielding*. As a consequence, background particles from outside the detector are stopped in the outer layers. This can be exploited together with position reconstruction to select an inner volume with an improved signal-to-background ratio. Further background discrimination is possible by determining the type of a particle interaction via the ratio between its S2 and S1 signals. As the amount of ionization electrons which are able to escape recombination depends on the geometry and density of the ionization track, the *S2/S1 ratio* differs with the energy loss of a particle. This allows to discriminate between ERs, where a particle recoils off a xenon shell electron, and nuclear recoils (NRs), where it recoils off a xenon nucleus. The auxiliary use of the S1 pulse shape for discrimination, in addition to the S2/S1 ratio, has been uncommon with dual-phase TPCs up to now. However, recent studies indicate interest in employing it for future analyses.

To maintain the performance of a LXe TPC, it is important to remove impurities dissolved in the xenon, such as H_2O and O_2. The former has a large absorption cross-section for VUV photons, resulting in diminished S1 and S2 signals. The latter is capable of binding ionization electrons. As a consequence, the size of an S2 signal depends, in addition, on the time the electron cloud spends in the LXe before being amplified when impurities are present. For these reasons, the xenon within the TPC is typically circulated through a getter during operation which is capable of binding and thus removing reactive impurities.

2 The XENON1T experiment

The XENON1T experiment [27] operated at a depth of 3.6 km water equivalent between 2016 and 2019 in the underground sections of the Laboratori Nazionali del Gran Sasso (LNGS) near L'Aquila, Italy. It was a dark matter direct detection experiment with the primary task of searching for particle dark matter, especially WIMPs. For this purpose, it employed a tonne-scale dual-phase xenon TPC (as described in Section 1.2.2) which allowed to significantly constrain the parameter space for WIMP-nucleon interactions. The strictest limit is at a WIMP mass of 30 GeV/c^2, which rules out spin-independent (SI) elastic WIMP-nucleon scattering cross-sections above 4.1×10^{-47} cm^2 at 90 % confidence level [23]. At the time of writing this thesis, the limits set for this interaction type are world-leading at WIMP masses above 6 GeV/c^2. XENON1T also managed, as the first experiment ever, to observe the two-neutrino double electron capture decay mode of ^{124}Xe at $T_{1/2} = (1.8 \pm 0.6) \times 10^{22}$ a [28]. In addition, the relative energy resolution at $\mathcal{O}$(1 MeV) (reaching $\sim$ 0.8 %) surpassed experiments specifically designed for that energy range via novel photosensor saturation correction algorithms [29], even though the detector had been engineered for measuring interactions at $\mathcal{O}$(10 keV). Future experiments utilizing dual-phase xenon TPCs will be able to employ the techniques developed to simultaneously search for particle dark matter interactions and the neutrinoless double-beta decay of ^{136}Xe while achieving competitive sensitivities for both [30, 31]. Finally, an excess of ER interactions has been observed below 7 keV [32], potentially hinting towards new physics. However, the origin of that excess cannot be precisely determined with XENON1T data alone, which also allows for tritium-induced background as a possible scenario. At the time of writing, XENONnT [33], an upgrade of XENON1T which is projected to be sensitive to WIMP-nucleon cross-sections as low as 1.4×10^{-48} cm^2, is in commissioning. Besides probing the WIMP-nucleon parameter space even further, it is expected to be able to differentiate between the two possible sources of the ER excess mentioned above at the 5σ level or higher [32]. Also, it will employ secondary photosensor readout channels with reduced amplification to minimize saturation effects at energies above $\mathcal{O}$(10 keV), which should result in an

even better energy resolution compared to XENON1T, facilitating the search for the ^{136}Xe neutrinoless double-beta decay [29].

This chapter gives a general overview of the XENON1T detector, recapitulating information available in [23, 27, 34, 35] unless noted otherwise. Focus is given to the TPC, the digitizers used for data acquisition (DAQ), the calibration sources employed, and the corrections applied to signals by the data processor, as an understanding of these topics is crucial for the analyses detailed in Chapter 3.

2.1 Time projection chamber

XENON1T's TPC (Fig. 2.1) was built using low-radioactivity materials exclusively which had been selected according to an extensive screening campaign [36–38]. It contained 2 t of LXe in its sensitive volume, with 3.2 t having been used in total when including the LXe surrounding the TPC. The sensitive volume was delimited by interlocking polytetrafluoroethylene (PTFE) panels which were arranged such, that its inner volume was approximately cylindrical with a diameter of 96 cm. Because of PTFE reflecting LXe scintillation light with a probability close to 100 % [39–41], the panels also aided in increasing the amount of photons collected by the two arrays of Hamamatsu R11410-21 photomultiplier tubes (PMTs) [42]. Of these PMTs, 127 were mounted in the top one and 121 in the bottom one. They observed the LXe drift volume and the GXe amplification region, recording both S1 and S2 signals. The drift volume had a length of 97 cm, with an electric field of about 120 V/cm respectively 81 V/cm, depending on the science run (SR), having been applied over it via the cathode and gate grids at its ends. Both grids were connected to each other via 74 copper field-shaping rings linked in series which had been placed equidistantly along the drift volume's length. Connections between the rings themselves and the gate grid were established by two 5 GΩ resistors per link, while the cathode grid and the bottom-most field-shaping ring were linked via two 25 GΩ resistors. Resistor values and grid shapes were optimized based on electric field simulations in order to define the electric potential such, that it changed evenly over the drift volume, resulting in a homogeneous drift field. Drifted ionization electrons were accelerated into the GXe phase by a 10 kV/cm extraction field defined between gate and anode grid to generate the S2 signal. In addition to the anode, gate and cathode grids, screening meshes

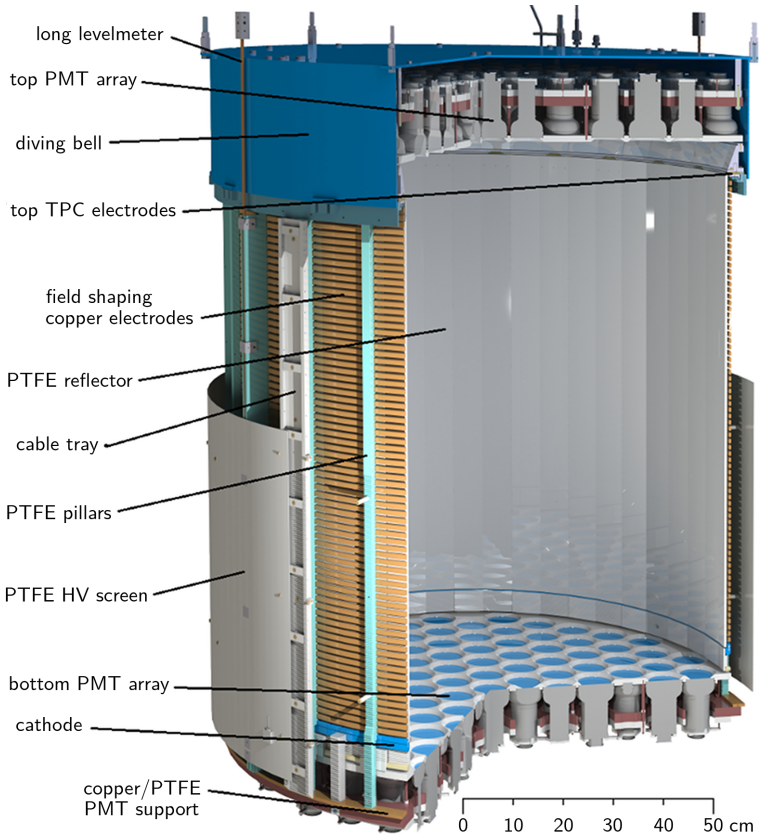

Figure 2.1: Render of the XENON1T TPC CAD model. The top TPC electrodes consist of both the anode and gate grids. Figure taken from [27] and modified.

had been placed in front of the PMT arrays to shield them from the grid potentials. These meshes were set to a voltage which minimized the strength of the electric fields between the PMTs and the anode respectively cathode.

The TPC was submerged entirely in LXe during operation. In order to maintain the GXe phase necessary for proportional scintillation, the top PMT array as well as the gate and anode grids were located within a diving bell structure. To pressurize the bell, purified xenon was flushed through it. An exhaust tube through which GXe could leave the bell allowed to set the height of the LXe phase relative to the gate grid by adjusting the tube's position via a motion feedthrough. Monitoring the height were six custom-made capacitive levelmeters. Four had a range of 10 mm with a precision of 0.03 mm and were used for the primary measurement of the LXe level. The other two had a range of

1360 mm with a precision of 2 mm for determining the LXe height while filling and emptying the TPC.

To thermally insulate the TPC to be able to maintain a LXe phase, it was contained within a double-walled cryostat made out of low-radioactivity stainless steel selected according to the screening campaign mentioned above. The cryostat's inner vessel of 1.1 m diameter and 1.96 m height was contained within the 1.62 m diameter and 2.49 m height outer vessel. To sustain an insulation vacuum, the volume between the two was continuously pumped. Surrounding the cryostat was a concrete tank of 9.6 m diameter and 10.2 m height containing 730 m^3 of deionized water. The tank's walls were clad with reflective foil and instrumented with PMTs for detecting Cherenkov light created by muons passing the tank. In case of a muon crossing, the resulting signal could then be recorded, allowing to reject interactions containing NRs caused by muon-induced neutrons with an efficiency of 99 %. To connect the cryostat to the other XENON1T subsystems, a cryogenic pipe was used which passed through the water tank. It allowed for xenon in- and outflow and to lead sensor cables to feedthroughs which connected them to the outside.

2.2 Cryogenics, xenon storage and purification

The cryogenic system (Fig. 2.2) consisted of three cooling towers for the continuous liquefaction of xenon. Two of them used pulse tube refrigerators (PTRs) with a cooling power of 250 W each, one of them running during operation and the other one on standby as backup. The third tower utilized liquid nitrogen for cooling to maintain liquefaction in case of a total loss of power. Xenon was stored in a spherical stainless-steel vessel of 2.1 m diameter and 2.8 cm wall thickness, called *ReStoX*. It is capable of withstanding pressure differences up to 73 bar, making it possible to store 7.6 t of xenon as either gas, liquid, or supercritical fluid. During operation, ReStoX was continuously cooled down using liquid nitrogen to keep the xenon inside in the liquid phase. Pipes which connected ReStox to the inner cryostat allowed to directly fill LXe into the latter and to also quickly recuperate LXe in case of an emergency.

To clean the xenon target inside the TPC, it was continuously extracted from the LXe phase by CHART QDrive pumps and flushed through SAES PS4-MT50-R hot gas purifiers before having been led back to the GXe phase above the TPC. Part of the backflow was diverted into the diving bell to build up the pressure needed to maintain the GXe phase of the amplification region. A heat

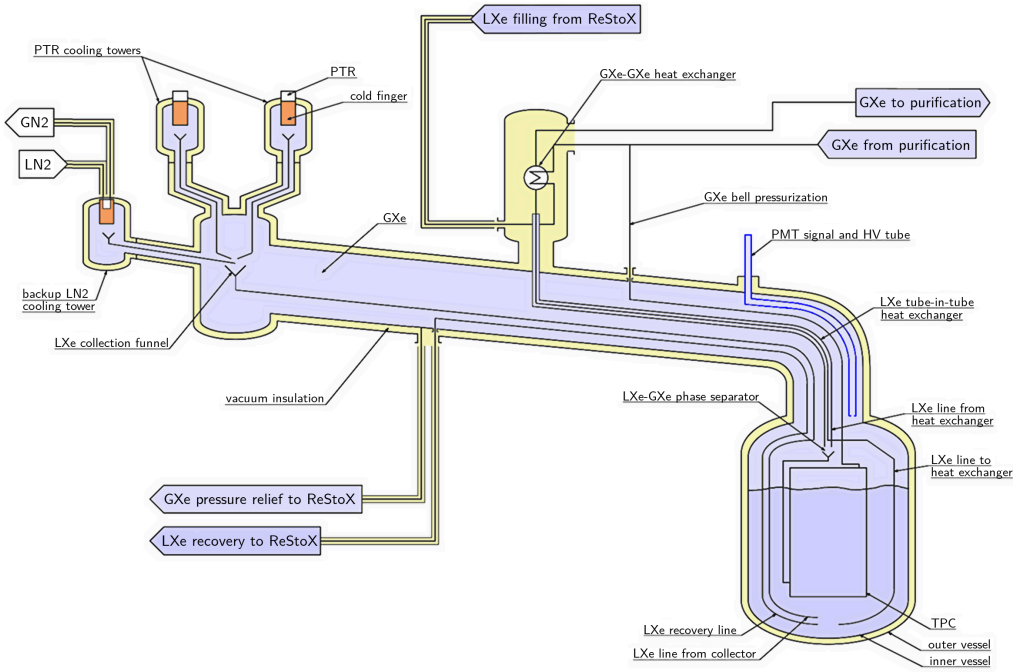

Figure 2.2: Diagram of the XENON1T cryogenic system and TPC vessels. The xenon liquefaction loop, the GXe purification loop and the filling/recovery connections to xenon storage (ReStoX) are indicated by the labelled lines. Figure taken from [27] and modified.

exchanger was employed to vaporize the outgoing xenon utilizing the heat of the ingoing xenon in order to reduce cryostat heat intake caused by circulation through the purification system.

2.3 Data acquisition and processing

The signals of each PMT were amplified by a factor of 10.0 ± 0.2 using Phillips Scientific Model 776 amplifiers [43] before having been fed into CAEN V1724 digitizer modules [44] for recording. This digitizer type houses several flash ADC boards which allow to record up to 8 channels simultaneously with a sampling rate of 100 MHz and a bandwidth of 40 MHz. It has a resolution of 14 bit over a dynamic range of 2.25 V. The maximum acquisition window size is about 5 ms. It allows to only keep samples above or below a certain threshold to save storage space via a feature called *Zero Length Encoding (ZLE)*. Due to rapid digitization and sufficient on-board memory available, data can be recorded without dead time as long as readout occurs fast enough. For XENON1T, the digitizers were running with a customized firmware which made it possible to continuously digitize signals above the set ZLE threshold without the need of receiving a trigger signal. This readout mode is called *self-trigger mode*, with the employed ZLE thresholds being referred to as the *self-trigger thresholds*. All digitizers were read out continuously during operation by DAQ readout computers which stored the recorded chunks of data into a buffer database for temporary storage.

A background program called *event builder*, which is part of the XENON1T data processing framework *pax* [45], periodically scanned the buffer database for periods in time where multiple chunks of data had been recorded within a certain timespan. Such an occurrence was treated as a software trigger signal. If a trigger was found, all data chunks within a window of 1 ms, centered on the trigger signal, were grouped into an *event* and permanently saved to disk. Afterwards, the stored data was processed by the pax data processor. It used the data chunks to reconstruct the PMT waveforms during an event, searched for S1 and S2 signals in them and determined signal parameters such as area, position in waveform, and signal type. Interaction vertex coordinates were reconstructed using a neural network trained with Monte Carlo (MC) PMT hit pattern data from photon propagation simulations of the full detector [46] together with the delay between S1 and S2 signal. The former gives the X and Y coordinates on a plane parallel to the gate grid, with $X = Y = 0$ on the

central TPC axis. The latter yields Z, with $Z = 0$ at the gate grid and assuming negative values below.

2.4 Calibration sources

Due to the self-shielding of xenon dual-phase TPCs and the dimensions of the one used for XENON1T, external calibration sources employing β- or γ-radiation could not be used to determine the response of the inner volume to ERs. To solve this issue, XENON1T utilized radionuclides for ER calibration which can be mixed homogeneously into the xenon target itself and decay fast enough for the ER rate to reach its pre-calibration value within $\mathcal{O}(1\,\mathrm{d})$. These nuclides are the noble gases $^{83\mathrm{m}}$Kr [47, 48] and ^{220}Rn [49]. The former was used to determine the light collection efficiency over the TPC volume for both S1 and S2 signals, while the latter was utilized to study the detector's response to ER signals, especially those in the region of interest (ROI) for the SI elastic WIMP-nucelon scattering search.

The response to NRs was measured via two different external neutron sources. One of them is an Am-Be source where the α-decays of the former produce neutrons through (α, n) reactions with the latter [50]. The other one is a neutron generator which emits neutrons created via deuterium-deuterium fusion at energies between $\sim$ 2.2 MeV and $\sim$ 2.7 MeV [51]. The neutrons produced by both sources enter the detector from the outside and scatter elastically off xenon atoms, resulting in NR signals.

2.5 Signal corrections

The reconstructed size of S1 and S2 signals depends on several factors. One of them is the location of an interaction inside the TPC as the light collection efficiency varies over the detector volume due to geometry effects. The arrangement of the PMTs, which all have different detection efficiencies and, in some cases, had to be switched off because of operational issues, also plays a role. S2 signals are, in addition to variations in light collection efficiency, also affected by a non-constant thickness of the amplification region caused by grid sagging and warping as well as residual tilts of the liquid-gas interface. Because the amount of proportional scintillation photons per ionization electron depends

on that thickness, this results in an additional position dependence. Furthermore, impurities within the xenon, such as O_2, are able to temporarily bind ionization electrons, reducing the amount of electrons crossing the liquid-gas interface. Finally, S2s above a certain size, found to be $\mathcal{O}(10^5\,\mathrm{PE})$, are too large to fit entirely into the dynamic range of the V1724 digitizer and are, as a consequence, clipped. In cases where one or more PMTs receive large amounts of light such, that either the PMTs themselves or the electronics involved in the signal chain are not operating in their linear regime, the signal is distorted in addition to being clipped.

To account for these effects, different corrections are applied. Effects depending on position are corrected for by dividing the detector volume into several sub-volumes and determining the average sizes of S1 and S2 signals induced by $^{83\mathrm{m}}$Kr which, based on the reconstructed interaction coordinates, occurred within these sub-volumes. This allows to map the detector response to S1 and S2 signals based on their reconstructed position and to normalize their sizes to the average response over the entire volume (Fig. 2.3). S2 size reduction due to impurities is compensated by determining how much proportional scintillation light had been lost because of them. The relative loss of ionization electrons per amount of time they spend in the LXe is assumed to be constant, resulting in an exponential decay of the number of electrons N_e:

$$N_e = N_{e,0}\, e^{-t_{\mathrm{drift}}/\tau_e} \tag{2.1}$$

Here, $N_{e,0}$ is the number of ionization electrons initially produced by the interaction which escaped recombination, and t_{drift} is the *drift time*, which is the delay between the S1 and S2 signal. The parameter τ_e describes the average time for an electron to attach to an impurity and is called *electron lifetime*. It is determined by fitting Eq. (2.1) to the drift time dependence of S2 signal sizes as seen in calibration data. The last effect, which is signal distortion caused by waveform clipping or non-linearities of the electronics involved, is corrected for at the waveform level by summing up waveforms of signal channels which are not affected by clipping to build a *template waveform* [29]. In channels affected by clipping, the waveform samples immediately before the signal clips are used to scale the template, which then replaces the rest of the clipped signal. This, for example, significantly improves S2 size reconstruction at high energies.

To differentiate between uncorrected and corrected quantities, the corrected S1 and S2 sizes are called *cS1* respectively *cS2*.

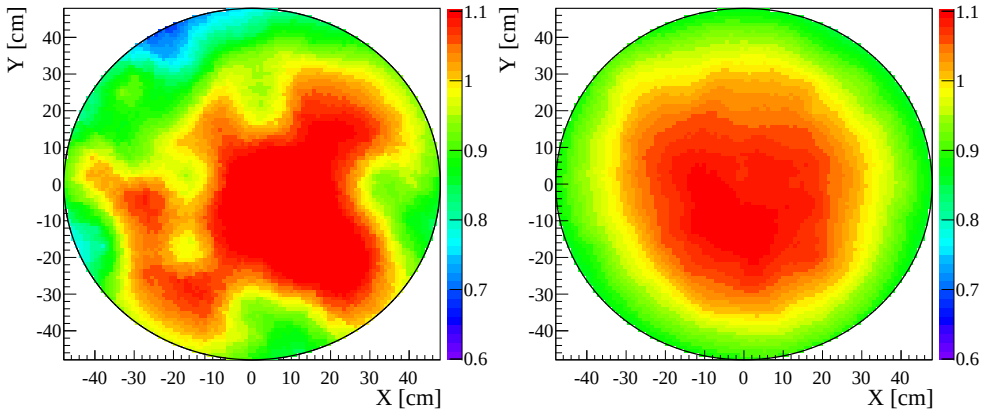

Figure 2.3: S2 *XY* light collection maps used for signal size correction. They were determined using ^{83m}Kr data. The color axis indicates the amount of an S2 signal's light seen relative to the average over the entire *X*-*Y* plane. Left: Top PMT array. Right: Bottom PMT array. The top array's map is less uniform compared to the one of the bottom array, because of the S2 signals being produced close to the top array. This leads to their light being spread over less PMTs. Local effects affecting light collection such as PMTs which were switched off are more pronounced as a consequence compared to the bottom array, over which S2 light spreads more evenly. Figure taken from [27] and modified.

3 Detector physics studies for XENON1T

In the search for rare events with XENON1T, considerable effort has been spent to comprehend the detector's response to particle interactions and to understand background event populations. Most of the latter can be discriminated against signal events, NRs in the case of SI WIMP-nucleon interactions, efficiently via use of the S2/S1 ratio. However, there are types of background for which other techniques have to be employed.

The studies presented in this chapter are concerned with analyses related to background signal sources in XENON1T. In Section 3.1, sources of electric noise are investigated. The stability of different noise components over the course of both published SRs is determined and the influence of a noise filter is quantified. Section 3.2 regards the identification of *gas phase events* in XENON1T. Such events are caused by physical interactions in the GXe phase of a dual-phase LXe TPC. Consequently, they do not yield S2/S1 ratios as expected from interactions in the LXe phase. Finally, Section 3.3 regards the application of pulse shape discrimination (PSD) in XENON1T data to aid in discriminating NRs against ERs. This could be especially helpful in cases where the S2/S1 ratio of an interaction is modified by signal losses, which could cause an ER to mimic a NR. A notable example is *surface background*, which is caused by particle interactions at or close to the PTFE panels enclosing the TPC [23].

3.1 Electric noise stability

The WIMPs searched for by XENON1T are expected to have recoil spectra which decrease exponentially towards larger energies (see Eq. (1.1)). Because of that, it is important to keep electric noise at a minimum. Otherwise, noise-induced artefacts could be mis-identified by the data processor as signals from proper physical interactions, resulting in an increased number of background

events at low energies and, consequently, a reduced signal sensitivity. Larger amounts of noise would also necessitate higher ZLE thresholds in order to avoid deadtime, caused by the digitizers recording data faster than the rates at which the readout computers can fetch it. Furthermore, low noise is also important at $\mathcal{O}(1\,\mathrm{MeV_{ER}})$ or higher, which is the energy scale of the double-beta decay of ^{136}Xe, a candidate for neutrinoless double-beta decay. The sensitivity to the latter process depends on the detector's energy resolution, which deteriorates with noise. As a consequence, it is essential to identify sources of electric noise and to monitor their stability over the course of the experiment. Both are done by analyzing Fourier spectra of waveforms with a length of 1 ms which contain no physical signals, called *noise waveforms* in the following, via the discrete Fourier transform (DFT) [52]. The waveforms were recorded during periodic PMT calibration measurements conducted over the lifetime of XENON1T by triggering the V1724 digitizers at a rate of 1 kHz. While taking noise data, the ZLE data reduction algorithm was switched off to retain every sample.

Before calculating the spectra of the noise waveforms, the latter are preprocessed to facilitate the identification of spectral components. First, the average value of all samples of a waveform is subtracted from that waveform to reduce direct current (DC) contributions at $f = 0\,\mathrm{Hz}$, which correspond to a constant baseline offset and are not of interest. Second, a *window function* [53] is applied to each waveform in order to reduce spectral leakage. Spectral leakage is caused by a waveform necessarily being of finite length. Because the DFT assumes a periodic continuation of its input, discontinuities arise if samples at both ends of the waveform are not close to zero. A window function mitigates these discontinuities by making the waveform smoothly transition to zero at its ends. This comes with the cost of a worse spectral resolution. Here, leakage reduction is prioritized for identifying spectral components at different orders of magnitude, as smaller peaks might be drowned out by leakage from larger peaks. The window function chosen is the *Blackman window*, which provides a compromise between leakage reduction and spectral peak width. Reducing spectral leakage is also the main reason for subtracting the waveform mean in the first step, as DC contributions in the spectrum would also leak. Finally, the complex DFT coefficients are calculated using the fast Fourier transform (FFT) algorithm [54]. The absolute values of the coefficients constitute the *amplitude spectrum*, which gives a measure of noise strength.

An example can be observed in Fig. 3.1, where the spectrum of a single noise measurement is shown. It has been generated by averaging the absolute values of the Fourier coefficients over the measurement's first 50 events. Notable

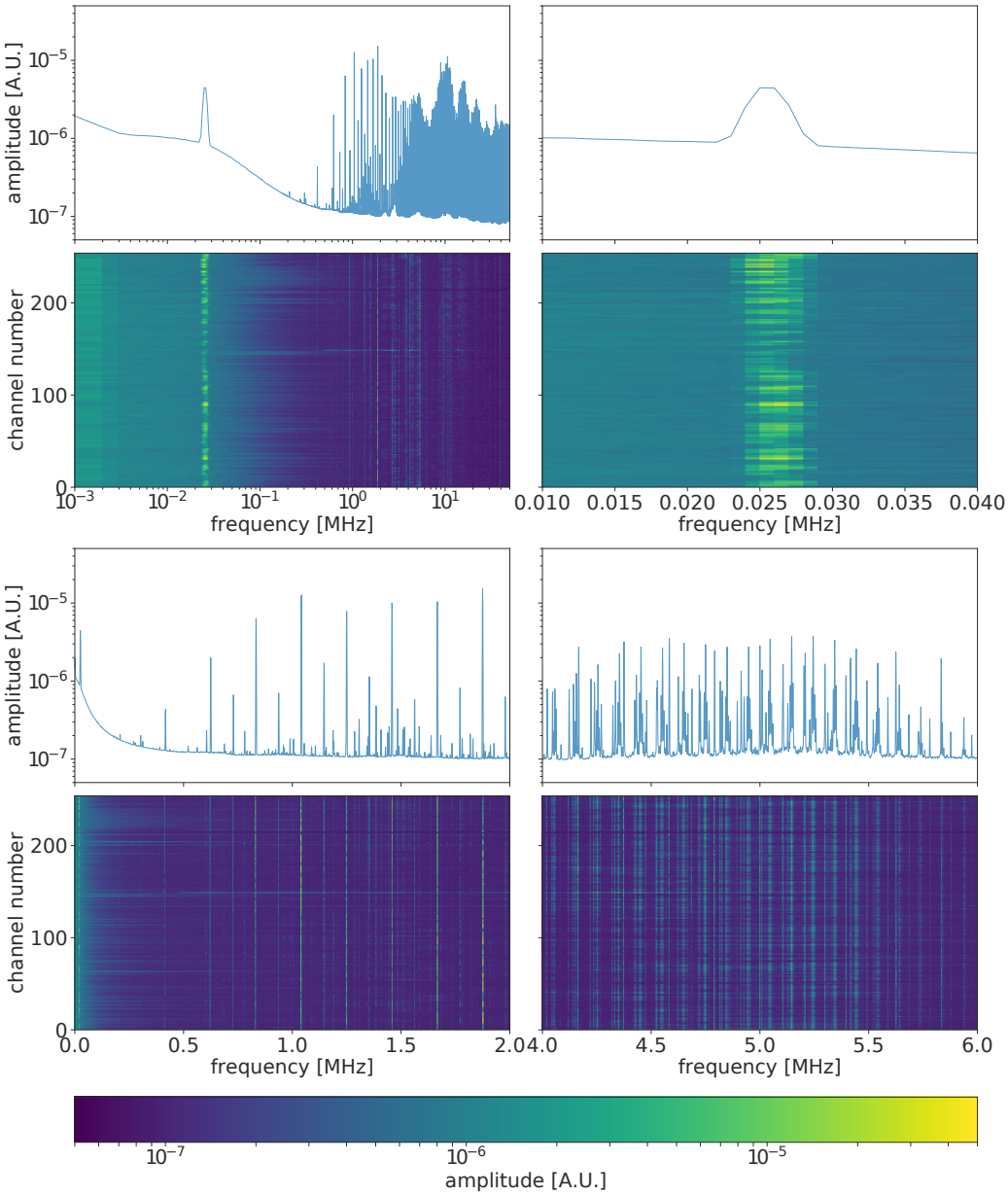

Figure 3.1: Full amplitude spectra extracted from noise samples taken on 21 November 2016, just before filter box installation. The line graphs show the spectrum averaged over all PMTs, while the 2D histograms directly below each graph display each channel's spectrum individually on the color axis.

features that are visible in all channels which were connected to a switched-on PMT, are the peak at ~ 25 kHz, the peaks at integer multiples of ~ 104 kHz, and a collection of peaks between 4 MHz and 6 MHz, called *peak forest* in the following. The latter consists of groups of peaks which are ~ 104 kHz apart, with the distance between peaks of a group amounting to ~ 6.6 kHz.

Also of interest are the complex phases of the Fourier coefficients. They are determined in the following way: First, the complex phases of the coefficients are aligned to the complex phases of the first event in the noise measurement by multiplying them with the factor below:

$$C_{\text{align}}(f, \Delta t) = e^{-i2\pi f \Delta t}, \tag{3.1}$$

where f is the frequency associated with the Fourier coefficient and Δt is the time passed since the first event. Second, the aligned coefficients are averaged over the first 50 events of the noise measurement. Finally, the phases of the averaged coefficients are extracted. A previous noise analysis which includes XENON100 [] and XENON1T data [55] has shown, that the phases of the spectral components mentioned above correlate with the PMT cabling layout. The ~ 25 kHz component displays a phase correlating with the digitizer to which a given PMT was connected (Fig. 3.2, top). For the component with a fundamental frequency of ~ 104 kHz, the phase correlates with the HV power supply unit powering the PMT instead (Fig. 3.2, bottom). Both frequencies, including the phase correlations, are also observed in noise data from XENON100 [56]. Because XENON100 used the same type of digitizer and HV modules as XENON1T, they both are identified as the sources of the corresponding noise components. Other regions of the Fourier spectrum do not exhibit any phase correlations as evident as those outlined above.

Because of the observation of noise from the HV during XENON1T commissioning, custom-made *filter boxes* have been designed [35]. These boxes consist of passive low-pass filters for each PMT with a stated cutoff frequency of 2.8 MHz each. The PMTs are connected to their corresponding HV modules via the boxes. This removes high-frequency noise originating from the modules themselves. Their effectiveness can be observed in Fig. 3.3, where noise spectra before and after filter box installation are compared. While noise power is reduced in general by about 22 %, it is especially evident for the ~ 104 kHz multiples which are reduced by up to 80 % or more in some channels, with the average over all channels being ~ 51 %. The ~ 25 kHz peak is, in comparison, only slightly affected. This observation confirms the effectiveness of the filter box in reducing noise and is compatible with the notion, that the ~ 25 kHz

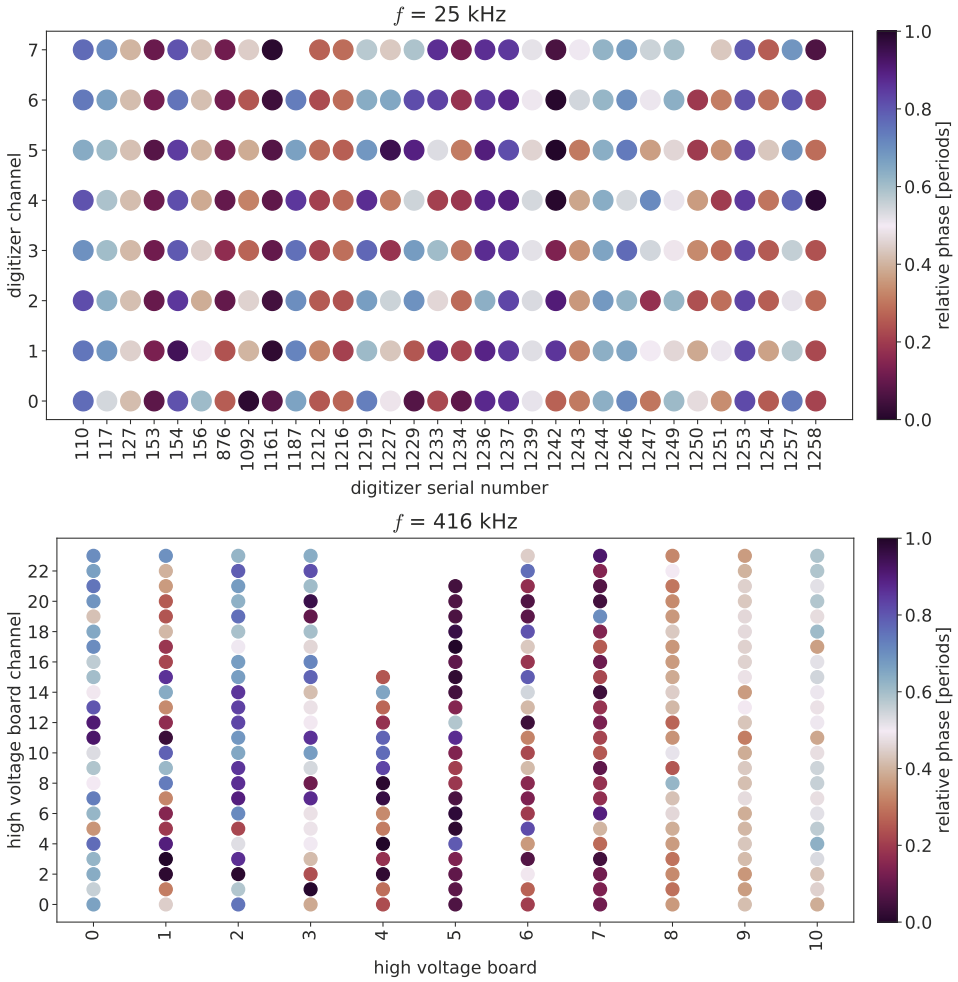

Figure 3.2: Relative phases at frequencies related to the ~ 25 kHz and ~ 104 kHz spectral components. They are averaged over 50 events, from noise samples taken on 21 November 2016, just before filter box installation. Phase correlations appear as channels on the same digitizer/HV board having similar colors. A couple of digitizers, such as 1229 and 1233, appear to have less or no correlation at all, which can be explained by the ~ 25 kHz component being weaker for them.

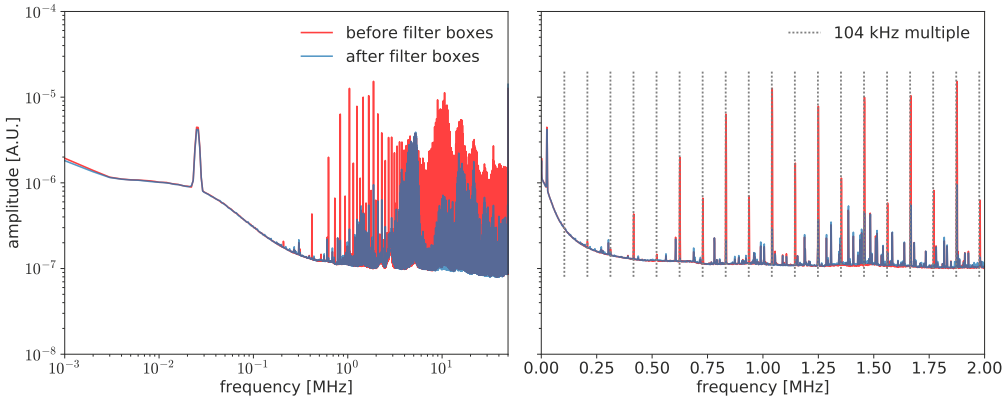

Figure 3.3: Comparison of single-event channel-averaged amplitude spectra of last noise measurement before filter box installation and first noise measurement afterwards. Left: Full frequency range (between 0 and 50 MHz). Right: Zoomed-in view. Frequencies which are multiples of 104 kHz are indicated by dotted, vertical lines.

component originates from the V1724 digitizers. According to the manual of the latter, a 1 V sawtooth signal with a frequency of 24.41 kHz can be generated by the digitizer's output connector for testing purposes. Because signals with this frequency have to be generated by on-board circuitry based on that fact, they could leak into the digitizer channels due to insufficient shielding. While the test signal generator is, based on these observations, a good candidate for being the source of the ~ 25 kHz peak, a direct confirmation would require an examination of the modules themselves.

During both SR 0 and SR 1, the evolution of the *noise amplitude sum*, defined as the integral of the amplitude spectrum over a certain frequency interval, is determined to assess whether any changes in electric noise occurred. For the SR 0 analysis, each channel's amplitude spectrum is averaged over the first 50 events of a noise measurement as noise measurements typically have at least that many events. The standard deviation of each point of a spectrum, calculated analogously to the average, is taken as the approximate error. Because the PMTs were not switched off during a noise measurement and thus still observed the LXe target, S1 and S2 signals are occasionally contained within a noise waveform. If this is the case, the Fourier spectrum of an affected waveform contains additional components which are sufficient to drastically bias the average spectrum. To remove noise measurements which are affected by having seen S1/S2 signals, the channel-averaged amplitude spectrum is calcu-

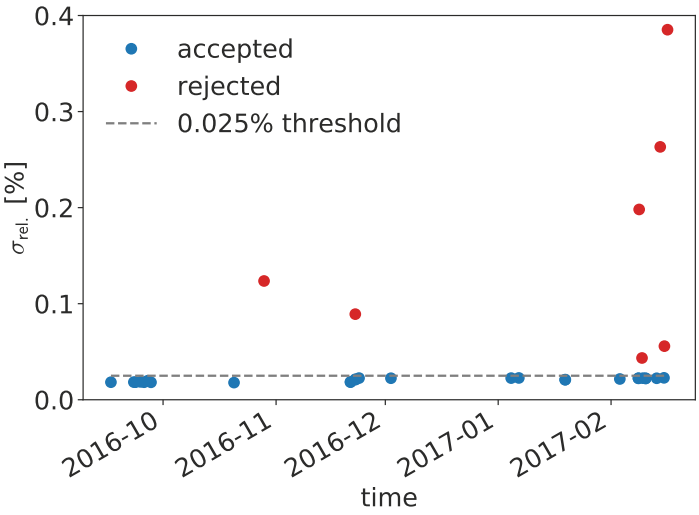

Figure 3.4: Relative error of the channel-averaged amplitude spectrum integral for all SR 0 noise measurements, including periods during XENON1T commissioning and after the end of SR 0. Measurements above the indicated threshold are rejected.

lated using each channel's event-averaged spectrum. Only channels which are connected to a PMT used in the SR are taken into account. Afterwards, the total integral of the channel-averaged spectrum is calculated together with an error estimate for the integral derived from error propagation. The SR 0 noise measurements are then divided into two groups based on the relative error of the integral (see Fig. 3.4). If the relative error is larger than 0.025 %, the noise measurement is not taken into account for the SR 0 evolution analysis.

For the SR 1 evolution analysis, the method for calculating the spectra changed to account for accidentally recorded signals. There, the first 12 events of a noise measurement are utilized to calculate the median amplitude spectrum of each channel. The median is more robust against single outliers than the average, so accidentally recorded physical signals do not bias the result as much. A trade-off of using the median is, that only a small number of events of a measurement could be processed at the same time due to computer memory constraints. Here, the number of events is chosen to be 12 to stay within the memory limits of the facilities used for this analysis. The error of each median amplitude spectrum point is estimated via a run of several noise datasets taken subsequently in short order to have independent measurements of the same noise conditions. After determining the median spectra of the first 12

events of a dataset, the standard deviation of the estimated median is calculated for every sample. The relative error is constant over the entire frequency range and determined by fitting a constant via χ^2 minimization to be 19.5 %. Local deviations from that value are explained by peak position fluctuations at $\mathcal{O}(1\,\mathrm{kHz})$, which have been observed between measurements. Afterwards, the frequency range integrals are calculated in the same way as it is done for SR 0. This way of calculating spectra is actually also preferred for SR 0 data, but a re-analysis could not be realized in time for this work due to raw data access being difficult after XENON1T ceased operation.

The evolution of the noise strength for six different intervals in the frequency spectrum is shown in Fig. 3.5 for a period around SR 0 and in Fig. 3.6 for SR 1, whith the chosen intervals being:

- $[0\,\mathrm{Hz}, \infty]$ — entire spectrum
- $[22\,\mathrm{kHz}, 30\,\mathrm{kHz}]$ — centered on $\sim$ 25 kHz component
- $[414\,\mathrm{kHz}, 418\,\mathrm{kHz}]$ — centered on multiple of $\sim$ 104 kHz
- $[4\,\mathrm{MHz}, 6\,\mathrm{MHz}]$ — contains peak forest
- $[0\,\mathrm{Hz}, 4\,\mathrm{MHz}]$ — pre-forest spectrum
- $[6\,\mathrm{MHz}, \infty]$ — post-forest spectrum

In SR 0, a sharp drop in noise amplitude can be seen at the time where the filter box was installed for frequency intervals which are dominated by HV board noise. Otherwise, the $\sim$ 25 kHz peak region only sees a slight drop after filterbox installation. Also, a gradual drop over time can be seen in the region containing the peak forest, which is attributed to the attenuation of the $\sim$ 104 kHz multiple peaks within it. Besides for the averaged median spectrum, the noise evolution is also investigated for each of the 248 PMT channels separately. Some channels display lower noise amplitudes compared to the average of other channels even before filter box installation. The former coincide with PMTs which experienced connectivity issues, caused by either a faulty signal or HV cable connection. Other channels show sudden shifts in some components (see Fig. 3.7). Some of them can be confirmed to have coincided with detector operations where PMT signal cables had been touched. The reason for other shifts is, at the time of writing, not known. Undocumented, minor detector operations involving signal cables, such as monitoring signals with an oscilloscope, cannot be ruled out.

In SR 1, noise conditions are generally stable over time except for single outliers which could not be correlated to detector operations at the time of writing. The ~ 25 kHz component shows a sudden drop at the end of May 2017 and gradually increases throughout the rest of the SR to a level slightly above the one before the drop. Because this component is attributed to the digitizers, the changes might have been caused by temperature changes in the DAQ electronis room. Confirming this requires further investigation.

3.2 Gas phase event rejection

Physical interactions do not only occur in the LXe phase of a TPC, but also in the GXe phase. They are mainly caused by radiation originating from detector components, especially radioactive trace nuclides within the PMTs [36]. Such interactions are called *gas phase events* in the following and typically result in an S2-like signal. Because gas events do not originate from the LXe volume, they need to be identified and remove if the data processor mis-classifies them as regular interactions. This is especially crucial for analyses which only use S2 signals to achieve a lower energy threshold [57], as they cannot rely on information from S1 signals.

As it can be seen in Fig. 3.8, the electrodes and PMTs at the top of the detector define three GXe regions with different electric fields each. The first one is the amplification gas gap region. Interactions within it are expected to result in a gas phase S1 signal and a gas phase S2 signal taking place at the same time, as the proportional scintillation process starts immediately. Consequently, both cannot be separately resolved in time and appear as a single S2-like signal.

The second region is delimited by the anode and the top PMT screening mesh. The anode operated at a higher voltage than the screening mesh, causing ionization electrons to drift towards the anode. The electric field is expected to rise when getting closer to the anode grid, eventually surpassing the proportional scintillation threshold and resulting in similar signals as those in region 1.

The third region is defined by the top PMT screening mesh and the top PMT array. Because each PMT has been operated at different voltages over the course of XENON1T, with some of them even having been switched off, the electric field in region 3 is more inhomogenous compared to the other regions. Because the screening mesh is set to the average voltage of the top array PMTs,

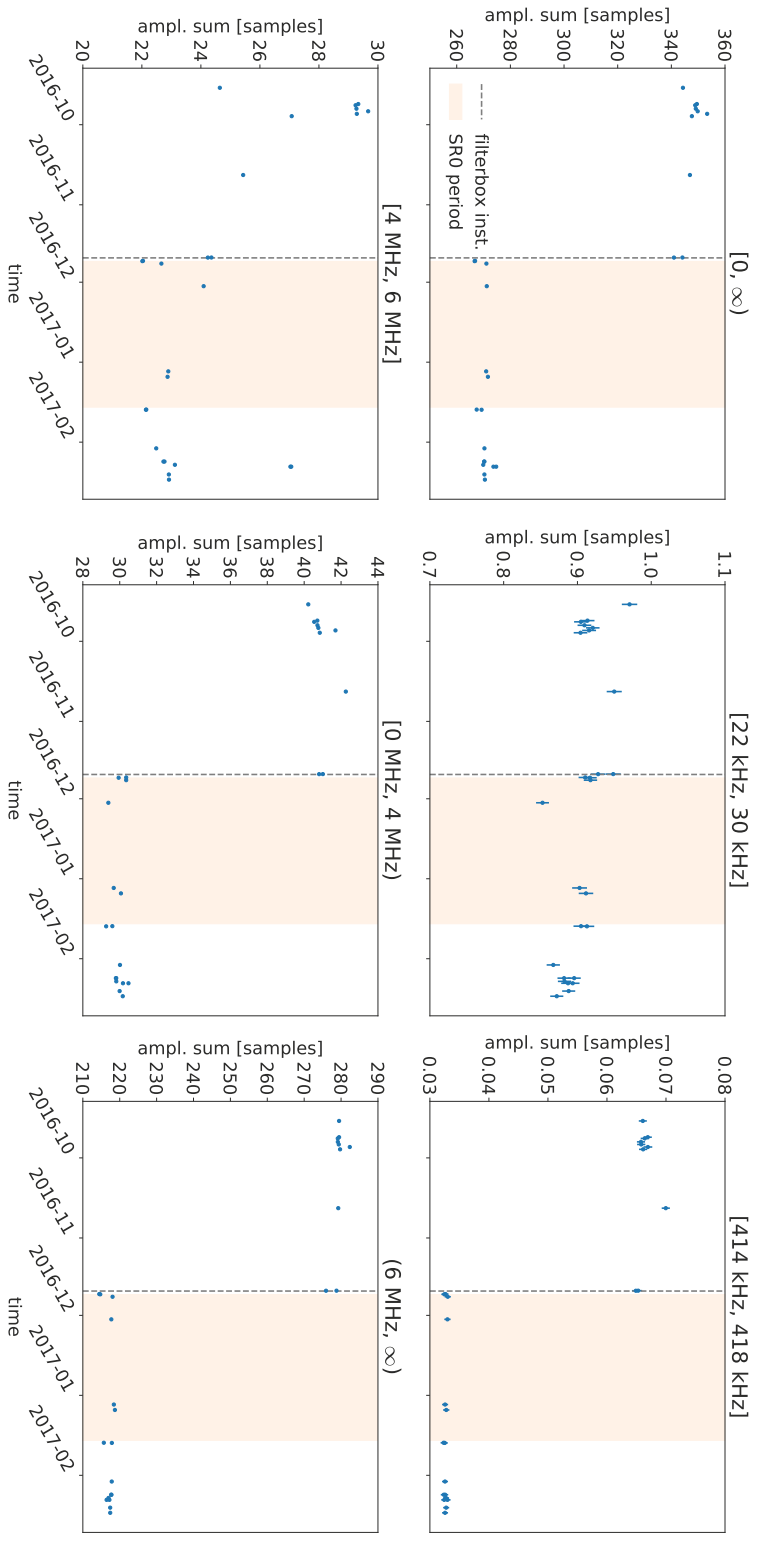

Figure 3.5: Noise evolution during XENON1T commissioning and SR 0. The amplitude sums of the six different frequency intervals of the channel-averaged spectrum are shown over time.

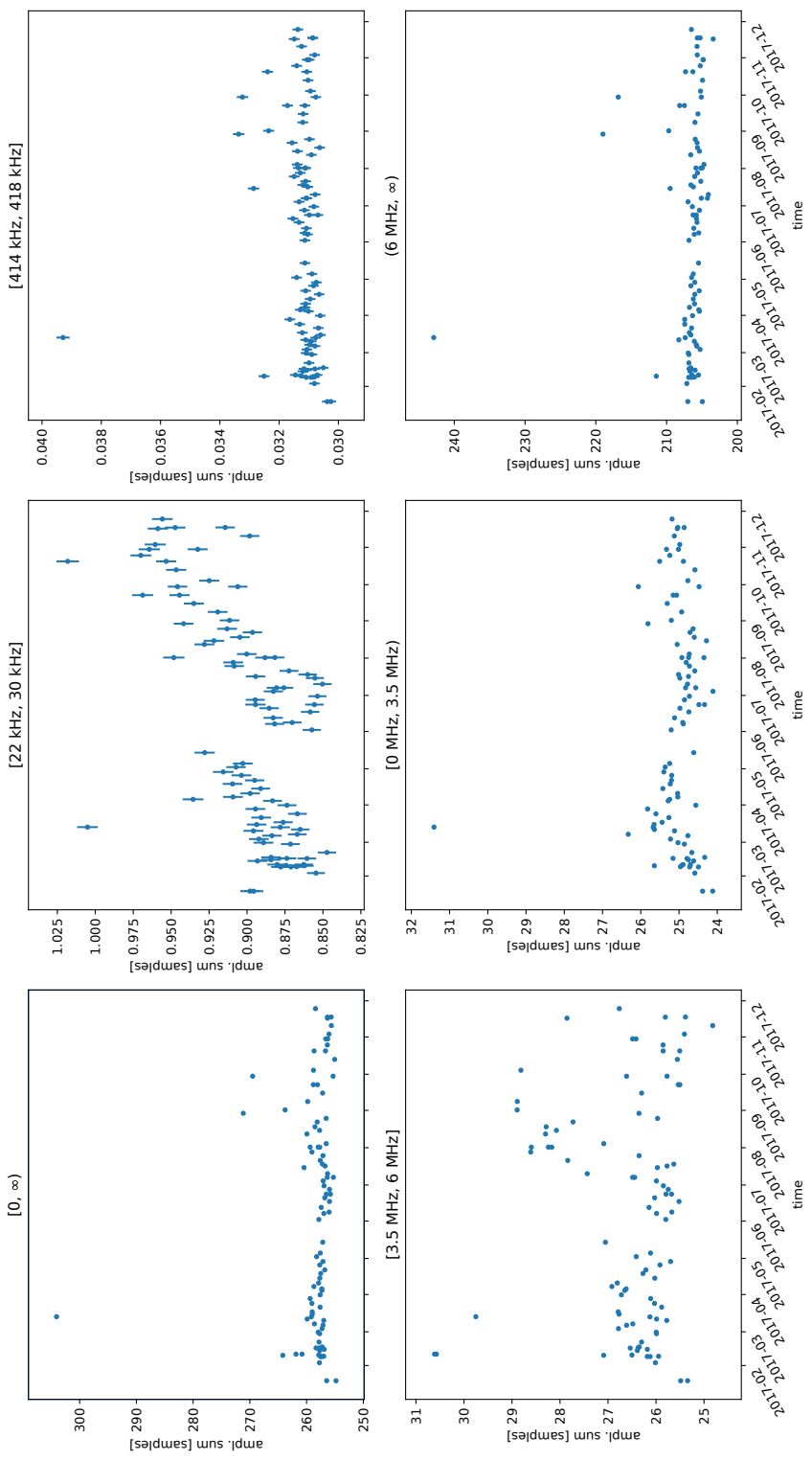

Figure 3.6: Noise evolution during SR 1. The amplitude sums of the six different frequency intervals of the channel-averaged spectrum are shown over time.

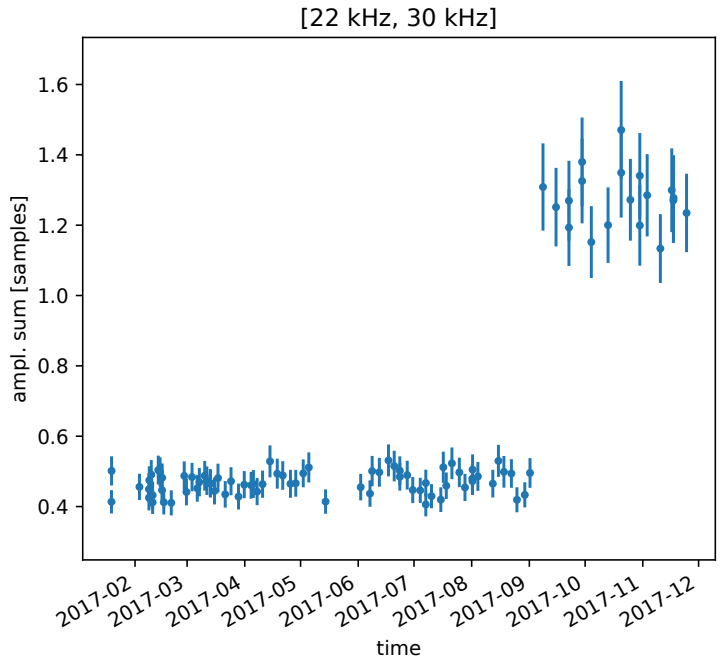

Figure 3.7: Example for a sudden shift in noise conditions correlated with PMT signal cable operations during SR 1. The presented amplitude spectrum integral is from a channel which was switched-off before the SR started.

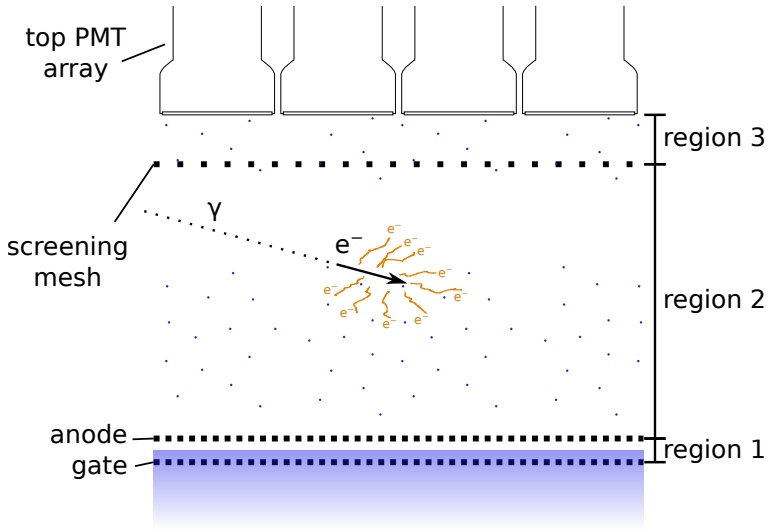

Figure 3.8: Illustration of the XENON1T TPC GXe phase region. Distances between electrodes and PMTs are to scale.

with some PMTs having been operated at higher absolute voltages, the field lines could locally point towards the top array instead of the screening mesh. In this case, ionization electrons could drift into region 2 and generate a gas phase S2. This S2 would be delayed relative to the gas phase S1, potentially making them separable in time. Here, it depends on whether the data processor correctly identifies the gas S1 if such events pose a problem or not. Regarding other gas phase S2 production mechanisms, it has to be considered, that a switched off PMT and the screening mesh in front of have a voltage difference of about $\sim$ 1550 V [27]. This could locally result in field strengths above the proportional scintillation threshold and cause signals similar in signature to those in the other regions.

As described above, gas phase events result in what appear to be lone S2 signals. If a lone S1-like signal, such as a coincidence of PMT dark pulses, accidentally occurs close in time, both gas S2 and lone S1 together can mimic a LXe interaction which takes place in the drift volume. The S2-like signals are, however, wider on average compared to true S2 signals from LXe interactions. This is because GXe is of lower density than LXe, resulting in longer particle track lengths in the former and, consequently, a larger initial dispersion of the ionization electron cloud. This feature is exploited in XENON1T analyses by applying an S2 width selection [34]. Electron clouds from interactions within the LXe broaden on their way to the liquid-gas interface due to diffusion. The dependence of the width over the drift time is well-understood and allows to reject events which do not follow it.

However, some gas events remain after applying the width criterion. To identify these, one can make use of the fact, that the light collection efficiency differs between region 1, where both gas signals and S2 signals from LXe interactions are created, and regions 2 and 3, in which only gas signals occur. Event selections based on this fact have already been designed and applied in previous XENON1T WIMP searches to guard against gas events, but they are only valid for the energy ROI of these analyses. Outside of that region, they deteriorate in performance.

In the following, the previous selections are improved upon by designing a cut which follows the same basic principles, but extends to significantly higher energies. This makes it applicable to other analyses such as neutrinoless double-beta decay searches and background spectrum matching via MC simulations. The main motivation for the cut is, as for its predecessors, to reject gas events based on only the parameters as outlined in the next section. The targeted acceptance for signal-like events is 99 %.

3.2.1 Gas event selection parameter space

The principal parameter is the *area fraction top (AFT)* of an S2 signal, AFT_{S2}. It is defined as the fraction of an S2 signal seen by the top PMT array and typically amounts to $\sim$ 0.6 for S2 signals caused by interactions in the LXe drift volume. Interactions occurring in regions 2 and 3 have a larger AFT_{S2} compared to region 1 interactions. This is due to light collection efficiency differences attributable to the grid placement and interactions in regions 2 and 3 being in closer proximity to the top array than those in region 1. The width of the of the S2 AFT parameter distribution depends on the amount of photons detected in total (see Fig. 3.9, left). A parameter proportional to that is the *raw S2 charge*, $S2_{\mathrm{raw}}$. It amounts to the total charge, in units of photoelectrons (PEs), seen by all PMTs without any kind of correction, such as those for light collection variations brought about by the TPC geometry, applied. As a consequence, any selection in AFT_{S2} must take the dependence on $S2_{\mathrm{raw}}$ into account.

One parameter space in which the gas event selection could be defined is $(S2_{\mathrm{raw}}, AFT_{S2})$. However, the AFT_{S2} parameter depends on the location in the amplification gas gap where the S2 is generated due to light collection efficiency variations. These are primarily caused by the detector geometry and PMTs which became defunct during XENON1T operation. Thus, it is preferable to apply the S2 XY correction maps (see Section 2.5) to the S2 signal contributions from both top and bottom PMT array separately and calculate AFT_{S2} with the corrected values. The resulting, correction-including AFT parameter is called $cAFT_{S2}$ in the following (see Fig. 3.9, right). Consequently, the parameter space in which the selection is defined is:

$$(S2_{\mathrm{raw}}, cAFT_{S2})$$

While spatial corrections have already been included in the definition of preceding AFT cuts, the analysis presented here has found an additional effect which needs to be corrected for. For reasons elaborated upon in Section 3.2.2, S2 area contributions from PMTs which developed a xenon leak during XENON1T operation are excluded when calculating the selection parameters. This is taken into account by the XY correction maps used here, which treat those PMTs as being switched-off.

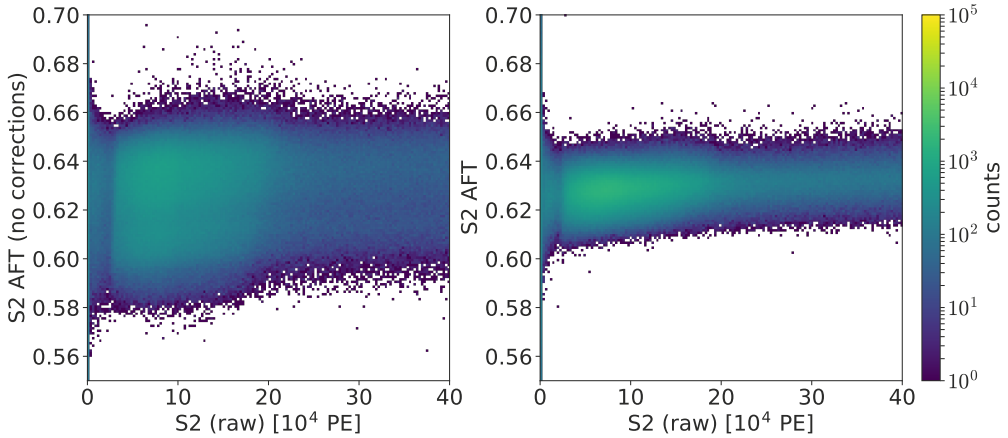

Figure 3.9: Comparison between AFT_{S2} and $cAFT_{S2}$. The distribution of the former is noticeably broader compared to the latter and depends on the location within the amplification gas gap where the corresponding S2 is generated.

3.2.2 Choosing a sample for defining the selection

To define a clean sample which contains as little gas events as possible, which is called *reference sample* in the following, ^{220}Rn and neutron generator (NG) calibration data taken during XENON1T's SR 1 is utilized. Initially, half of the available ^{220}Rn calibration data is used to retain the other half for cross-checks. The daughters of ^{220}Rn provide β-decays with Q-values up to $\mathcal{O}(1\,\mathrm{MeV})$ which yield a continuous S2 spectrum. The NG data is added in order to increase statistics at $S2_{\mathrm{raw}} < 10^4$ PE. NG events with a larger S2 size are not included, as their $cAFT_{S2}$ distribution is broader compared to ER interactions with comparable S2 sizes. The exact cause of this broadening has not been determined, although merged multiple scatters (MMSs) are likely candidates. A set of criteria, including a subset of the data quality selection from [34], is applied to calibration data events before they are considered to only contain a negligible amount of gas events:

- Standard XENON1T data quality selection criteria:
  - DAQ veto: avoids events where not all digitizer boards were ready to accept signals.
  - Flash veto: rejects events during periods where at least one PMT emitted bursts of light.

- The event must contain at least one successfully matched S1/S2 pair.
- The X and Y coordinates of the main interaction S2 must be within the central 36.94 cm of the TPC. This is to only select regions where the response of the S2 XY correction map is uniform.
- The width of the main interaction S2 must follow the expected electron drift time dependence. The corresponding selection is an extension of the S2 width cut, described in [34], to 3 $\mathrm{MeV_{ER}}$.
- The goodness of fit parameter when comparing the S2 hit pattern with the reconstructed vertex coordinates must be better than a certain threshold. The corresponding selection is an extension of the S2 pattern likelihood cut, described in [34], to 3 $\mathrm{MeV_{ER}}$.
- The reconstructed z coordinate must be at least 10 cm below the anode and 5 cm above the cathode. This is to avoid the main population of gas events, which is found to be reconstructed within the upper 10 cm of the drift volume, and to reject events which happen on the cathode. The latter result from, for example., radioactive decay of plated-out ^{222}Rn and ^{220}Rn daughters.
- The raw S1 area for events with $cS2_{\mathrm{XY}} < 300$ PE must be smaller than 6125 PE. This avoids a population of events which consist of interactions in a charge-insensitive part of the detector, such as below the cathode. Their S1 signals are large enough to photoionize impurities, resulting in a small S2 signal which does not correspond in size to the actual charge signal.
- The time between the points where 80 % respectively 50 % of the main interaction S2 area are reached must be larger than 0.65 µs. This rejects a population of events where the S2 actually consists of merged, unrelated single electron S2 signals.

Fig. 3.10 shows the selection space after the application of all selection criteria so far. Besides the main band at $cAFT_{S2} \sim 0.63$, outliers can be seen above and below it. Outliers above the band correspond to gas phase events, based on their higher-than-average $cAFT_{S2}$ value, which have not been removed by the preselection criteria. Inspection of the recorded waveforms belonging to outliers below the band indicates, that the latter result from mis-classified S1 and S2 signals. To improve on the reference sample, a loose cut in the selection space itself is applied to remove the outliers, indicated in Fig. 3.10.

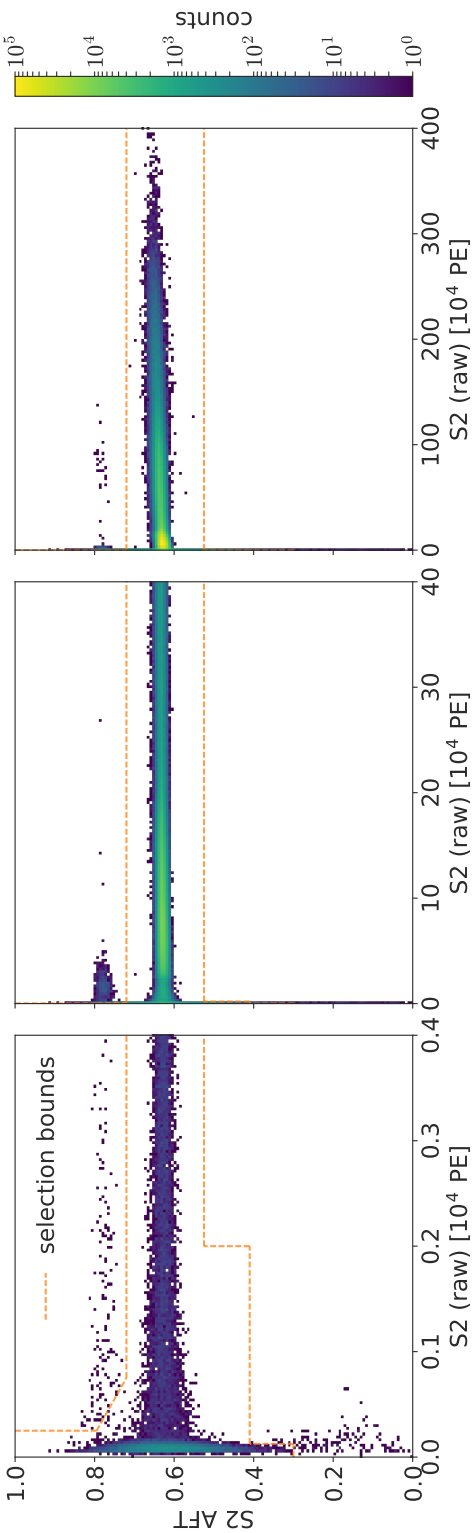

Figure 3.10: Selection space for defining the cut after applying all selection criteria besides the outlier removal. The boundaries of the latter are shown as dashed lines.

It is found that the AFT is modified by *PMT afterpulses (APs)*. APs are generated by residual gas atoms and molecules inside a PMT being ionized by the electron avalanche caused by the detection of a photon. They correspond to signals with charges up to multiple PE and occur delayed relative to the physical interaction which caused them [42]. In XENON1T, some PMTs developed a leak during operation through which xenon could enter them. This resulted in the probability for afterpulses to occur in these PMTs to rise over time. Comparing $cAFT_{S2}$ for S2 signals which occur close to one of these PMTs to signals which happen in different parts of the detector shows (Fig. 3.11), that the former have larger $cAFT_{S2}$ values on average compared to the latter. The APs of S2 signals cannot be resolved separately in time and are merged into the main signal. As a consequence, APs increase the effective average charge per PE for the affected PMT, boosting the AFT value. Because the AP probability is time-dependent, it induces a corresponding dependence of the AFT selection. To counteract the effect, contributions from AP PMTs are removed from $S2_{\mathrm{raw}}$. Also, XY correction maps which take this removal into account have been generated, originally for the high-energy reconstruction analysis. $cAFT_{S2}$ is then calculated using these maps. The result can be see in Fig. 3.11, where the difference between the AP PMT region and unaffected regions is smaller.

At the end, the reference samples is split into two halves of equal size, with only one of them being used to define the selection. This is done to estimate parameters such as acceptance and gas event rejection in a statistically independent way.

3.2.3 Defining the selection

Having defined a reference sample, the selection space is sliced in $S2_{\mathrm{raw}}$. Bin sizes vary, with a finer binning selected for regions where the S2 AFT band shape changes more abruptly. The different slicing regions are defined in. For each slice which contains at least 200 events, both the 0.5 % and the 99.5 % percentiles in $cAFT_{S2}$ are estimated numerically. To both types of percentiles, the following function is fit via χ^2 minimization to define the boundary lines of the selection:

$$f(x) = \sum_{n=0}^{5} p_n x^n + \frac{p_6}{1 + p_7\sqrt{x}} + p_8\sqrt{x} \tag{3.2}$$

A dependence of the form $\sim 1/\sqrt{S2_{\mathrm{raw}}}$ can be argued to follow from the number of photons which hit the top PMT array being distributed according to a bi-

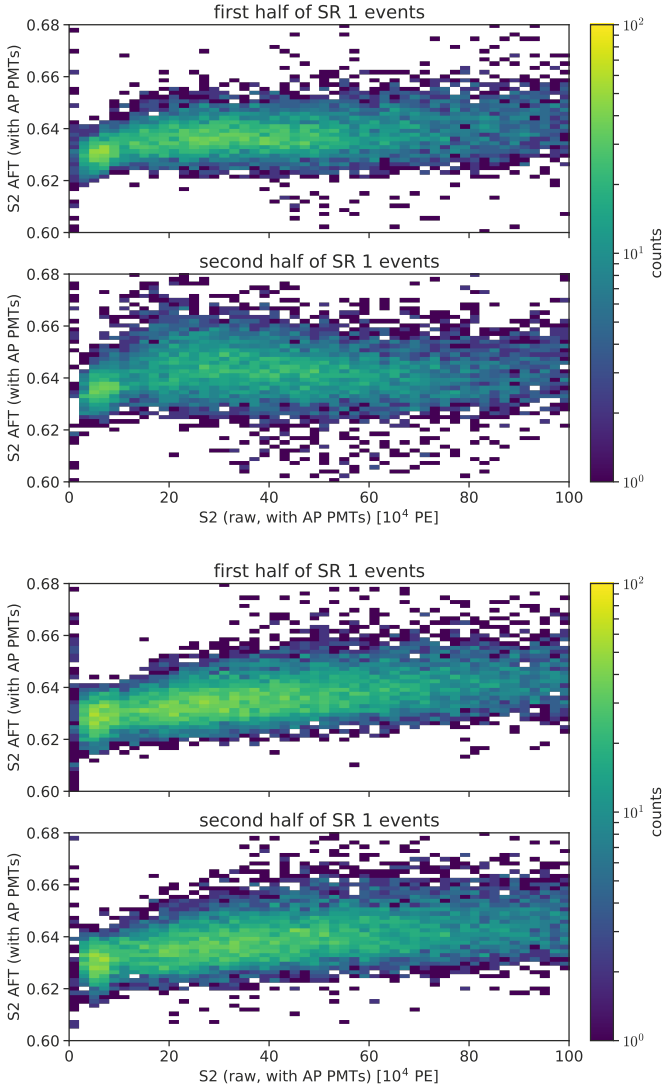

Figure 3.11: $cAFT_{S2}$ distributions when including AP PMTs. The data consists of the entirety of SR 1 science data, divided into two halves in time. Top: S2 signals which occurred in front of a PMT that developed a leak. The difference between the distributions of the two halves is evident, indicating a time dependence. Bottom: S2 signals from a reference region where no AP PMTs are located. The region has the same size as the one used for the selection in the top plot. Here, the time dependence is not as obvious (tailing towards larger $cAFT_{S2}$ can be seen to be larger in the second half when looking closely).

nomial distribution for a fixed number of initial photons. The other summands are empirical adjustments to better describe the dependence of the percentiles on $S2_{\mathrm{raw}}$. They have to accommodate changes in the shape of the main AFT band seen at S2 sizes. *A priori*, one would expect the average value of the main $cAFT_{S2}$ band to not depend on S2 size. A possible cause could be the high-energy reconstruction algorithms [29], which are needed to correct for effects related to PMT saturation and APs, not perfectly correcting the relative contributions of both arrays to the S2 size. In this context, it also has to be noted, that the high-energy corrections, while valid for both array contributions, have been optimized with a focus on the bottom array contribution. The latter is the only contribution used for energy reconstruction as the bottom array response is more homogeneous in XY compared to the top one.

The final result can be seen in Fig. 3.12. Along the selection space, the absolute relative deviation of the fit function from the estimated percentiles is, on average, smaller than 1 %. It is largest for the 99.5 % line at $S2_{\mathrm{raw}} < 750\,\mathrm{PE}$, reaching up to 9 %. This is attributed to residual gas events which remain after all preselection criteria biasing the percentile calculation, as the gas interaction AFT band starts to overlap with the main population at about 600 PE. Other deviations above 1 % could be explained by the fit function being empirical and not derived from first principles alone. Events with $S2_{\mathrm{raw}}$ above/below the largest/smallest central value of the slices used for fitting are set to always pass the defined AFT selection, as they are outside the region.

The fraction of events removed by the cut along $S2_{\mathrm{raw}}$ is calculated for both halves of the ^{220}Rn reference sample separately, with all preselection criteria applied. Working under the assumption, that the amount of events outside the main AFT band is negligible after the preselection, this gives an estimate of the cut acceptance for regular LXe interactions. Results can be seen in Fig. 3.13, which shows that both estimates are compatible with each other. Because one half has not been used for deriving the cut, the acceptance estimate using that half is not affected by biases related to overfitting. Such biases could be caused by statistics being insufficient to reliably estimate the 0.5 % and the 99.5 % percentiles. The fact that both estimates yield compatible results thus indicates, that the amount of events per slice in the half used for defining the selection is adequate.

Over the selection space, the estimated acceptance is widely compatible with the targeted 99 % value. There are three $S2_{\mathrm{raw}}$ intervals where it drops by up to 1 percentage point. In these intervals, an upward/downward bias of

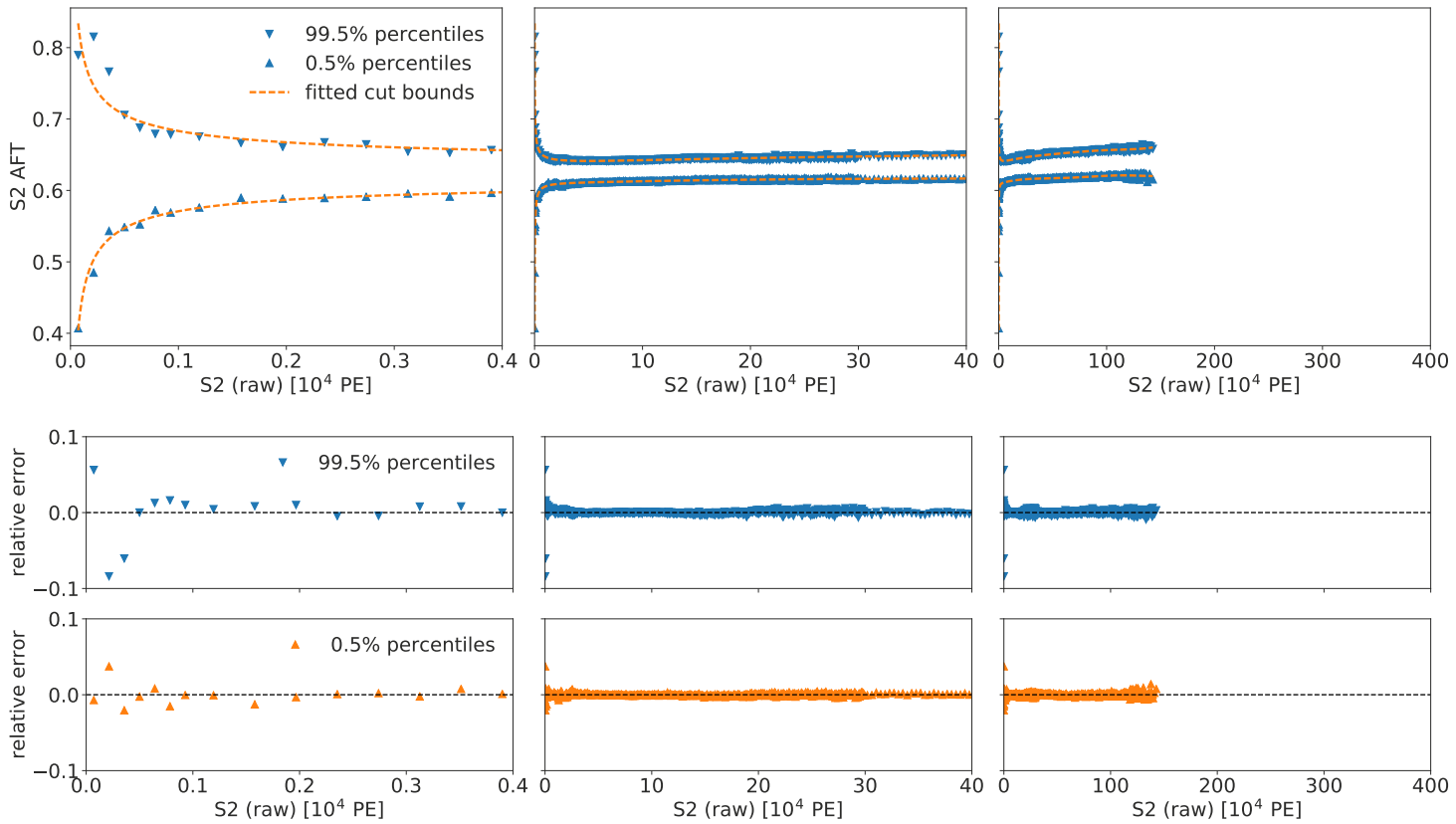

Figure 3.12: Result of the fit of Eq. (3.2) to the percentiles extracted from the cut definition sample. Top: Percentiles and bounds from fit. Bottom: Relative deviation of fitted function from percentiles. The second and third 99.5 % percentiles from the left, which show the largest deviation, are at the point, where the populations of regular S2 signals and S2-like signals from gas phase interactions start to overlap (compare to Fig. 3.10). A systematic downwards deviation from the 99.5 % percentiles between 20×10^4 PE and 30×10^4 PE can also be seen, which is attributed to the fit function being empirical.

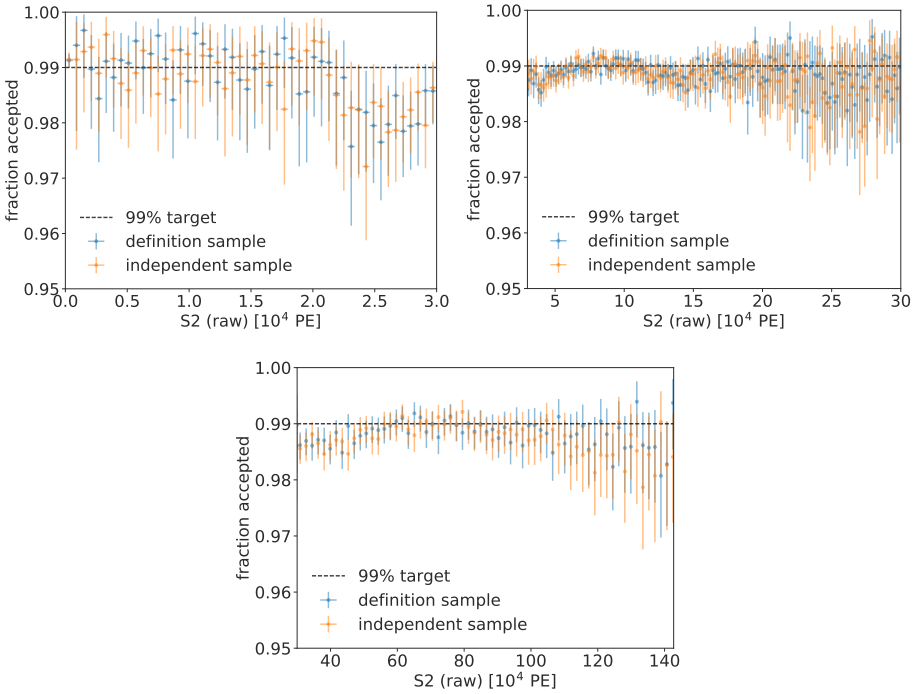

Figure 3.13: Estimated acceptance for regular S2 signals for each half of the ^{220}Rn reference sample.

the bottom/top boundaries relative to the numerical percentile estimates is observed. Accordingly, the drops are the result of the boundary line function being empirically motivated and, as a consequence, not being a perfect model for replicating percentile positions in the selection space. It must be noted, that the reported acceptance should be seen as a lower limit when it comes to single-site interactions. This is a consequence of the cuts which ought to remove multi-site interaction with merged S2 signals not having 100 % rejection power. Because β-decays in the ^{220}Rn chain can be accompanied by $\mathcal{O}(1\,\mathrm{MeV})$ γ-radiation, which results in multi-site events, some of them could remain in the reference sample. In addition, some gas phase events with $S2_{\mathrm{raw}}$ below 600 PE remain after preselection due to both AFT bands overlapping there. Following this, they are included as supposedly valid events when determining the acceptance, leading to the latter being underestimated.

3.2.4 Rejection power and cross-checks

The rejection power of the defined S2 AFT selection against gas phase interactions is estimated on a population of events within the secondary S2 AFT band above the main one as seen in ^{220}Rn calibration data. To select it, the cut list utilized for defining the AFT selection is modified to not reject gas phase events any longer:

- Standard XENON1T data quality selection criteria:
  - DAQ veto
  - Flash veto
- The event must contain at least one successfully matched S1/S2 pair.
- The X and Y coordinates of the main interaction S2 must be within the central 36.94 cm of the TPC.
- The reconstructed z coordinate must be at least 5 cm above the cathode.
- The raw S1 area for events with $cS2_{\mathrm{XY}} < 300\,\mathrm{PE}$ must be smaller than 6125 PE.
- The time between the points where 80 % respectively 50 % of the main interaction S2 area are reached must be larger than 0.65 µs.
- $cAFT_{S2}$ must be above the lower outlier boundary as defined in Section 3.2.3.

Additional selection criteria are applied to increase the ratio of gas phase events in the sample:

- The reconstructed drift time must be between 8 µs and 56.25 µs. AP clusters occurring after an S1 signal which are mis-identified as S2 signals are rejected by the lower boundary. The upper boundary is motivated by the fact, that most of the secondary AFT band population is found to lie below it.
- The S2 width must lie within 0.6 µs and 2.5 µs. This contains almost all secondary AFT band events while cutting into the main band.
- The raw S2 size *including AP PMTs* must be above 200 PE. Below this threshold, too many events remain in the main S2 AFT population. Accordingly, a reliable rejection power estimate can only be given above it. However, all XENON1T analyses which require both S1 and S2 signals also apply this criterion.

Projecting the thereby created gas phase interaction sample onto the $cAFT_{S2}$ axis shows, that the remaining events from the main AFT band can be approximately separated from the secondary band by applying a threshold of $cAFT_{S2} > 0.71$. This possible because the selection criteria as defined above strongly disfavor LXe interactions. Estimating the rejection power against this population along the $S2_{\mathrm{raw}}$ axis yields essentially 100 % efficiency above 600 PE within the region where the selection is valid. Between 200 PE and 600 PE, the rejection power drops below 80 % due to the larger variance of $cAFT_{S2}$ with less detected photons causing overlap with the reference S2 AFT population.

In addition to estimating the rejection power, the cut is applied on unblinded SR 1 science data to check for different behavior compared to calibration data. Repeating the acceptance estimation, it is evident, that significantly more events are removed above 10^5 PE compared to the target of 1 % (Fig. 3.16, top). Plotting the location of events removed (Fig. 3.16, bottom) reveals, that this drop is caused by a population within the upper 20 cm of the drift volume. As the latter's events do not distinguish themselves otherwise, there is no *a priori* reason to assume that they are supposed to be removed. This points towards an actual drop in acceptance for events with $S2_{\mathrm{raw}} > 10^5$ PE happening in the top 20 cm. A potential explanation for this is, that these events are most affected by imperfections of the high-energy corrections. This is because S2 signals from interactions with shorter drift times are larger as there is less time for impurities to bind ionization electrons. At the same time, their width is also smaller compared to S2s from interactions at lower height. This makes them

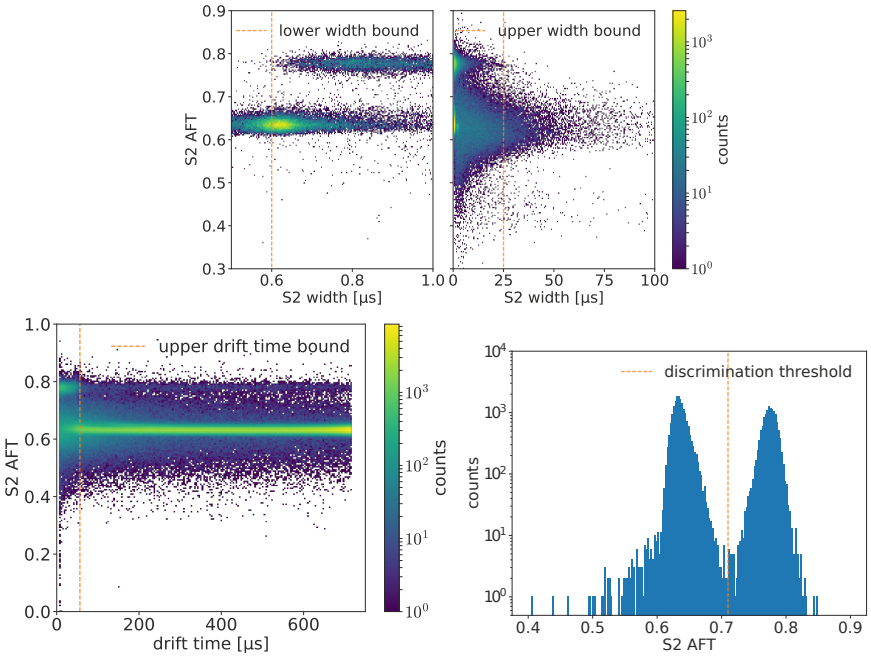

Figure 3.14: Parameter distributions relevant for selecting the gas phase event sample. Top: S2 width distribution. On average, S2-like signals from gas phase interactions are wider compared to regular S2s. Bottom-left: Drift time distribution. Gas phase events mostly have drift times below 56.25 µs assigned to them. Events from this range have S1-like signals which are broader compared to regular LXe interaction S1s occurring in front of the S2-like signal. This would point towards regions in the GXe phase where ionization electrons would need to drift first before proportional scintillation takes place, making the GXe S1 and S2 signals resolvable in time. Bottom-right: $cAFT_{S2}$ after application of all gas phase event selection criteria.

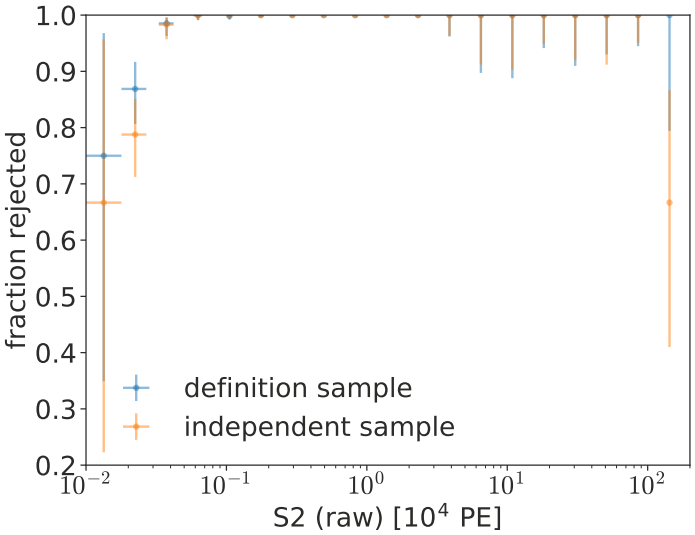

Figure 3.15: Rejection power against the gas event sample for each half of the ^{220}Rn reference sample. The drop of acceptance seen at the tail end of the $S2_{\mathrm{raw}}$ range of the independent sample is due to part of the corresponding bin including a region where the cut is invalid due to insufficient statistics for defining it. There, no events are removed as the extrapolated cut bound function does not match actual percentile positions.

more susceptible to saturation effects compared to S2s with equivalent areas, but spread out in time further. While this should also be observed in calibration data, the distribution of events in science data is markedly different. For the former, interactions are distributed homogeneously as ^{220}Rn mixes with the LXe. For the latter, events are concentrated at the edges of the drift volume as most of them are caused by background radiation originating from detector materials. Consequently, defining the cut on calibration data weighs interactions occurring in the center more compared to their actual frequency in science data, resulting in the observed difference.

A further investigation is made regarding the stability of the cut's acceptance in time (see Fig. 3.17). Up until the end of January 2018, the amount of events remaining after application of the cut is constant between 99 % and 99.5 %. During the last half-month of SR 1, it drops to about 98.5 %. Accordingly, it is, in good approximation, constant. This is in stark contrast to the version of the cut used for the SI WIMP analysis, where the acceptance drops over time as a consequence of rising AP rates.

In conclusion, the defined selection removes gas phase interactions at near 100 % efficiency for $S2_{\mathrm{raw}}$ above 600 PE. If events are constrained to $S2_{\mathrm{raw}} < 10^5$ PE or $Z < -25$ cm, acceptance for LXe interactions is close to $\gtrsim 99$ %. Otherwise, a drop down to ~ 80 % acceptance in the upper drift volume for large S2s has to be accounted for.

3.3 Exploration of pulse shape discrimination

In the SI WIMP analyses of XENON1T, surface background induced by ^{210}Pb plated-out onto the PTFE reflector panels of the TPC proves to be a major background contributor [23]. Because decays happening at or close to the panels experience charge signal losses, their S2/S1 ratio is lower compared to other ERs. This causes ER events to appear in regions of the $(cS1, cS2_b)$ space used in the likelihood analysis where NR events would be expected. Most of the surface ^{210}Pb decays are still correctly reconstructed close to the reflector panels. However, the finite position resolution of $\mathcal{O}(1\,\mathrm{cm})$ results in a significant amount of them being reconstructed closer to the central axis of the TPC. Restricting the fiducial volume to smaller radii reduces their amount, but sacrifices exposure proportional to $\Delta(R^2)$.

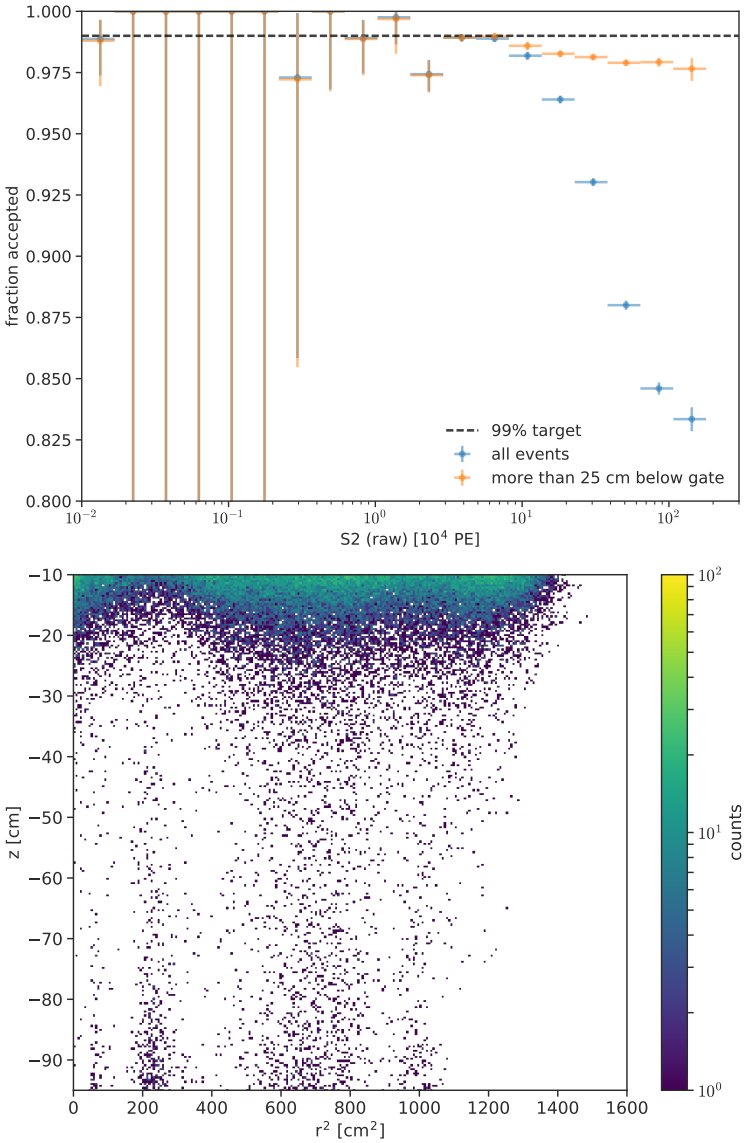

Figure 3.16: Cross-checking the derived AFT selection on unblinded SR 1 science data. Top Estimated acceptance over the S2 size range the selection has been defined for. A significant drop above 10^5 PE is visible which is almost exclusively caused by events originating from the top 25 cm of the TPC. Bottom Spatial distribution of events removed by the selection. Besides the population in the topmost 25 cm, lines at certain radii are also present. Imperfections of the S2 XY correction maps which would cause slight AFT shifts depending on position are a potential reason.

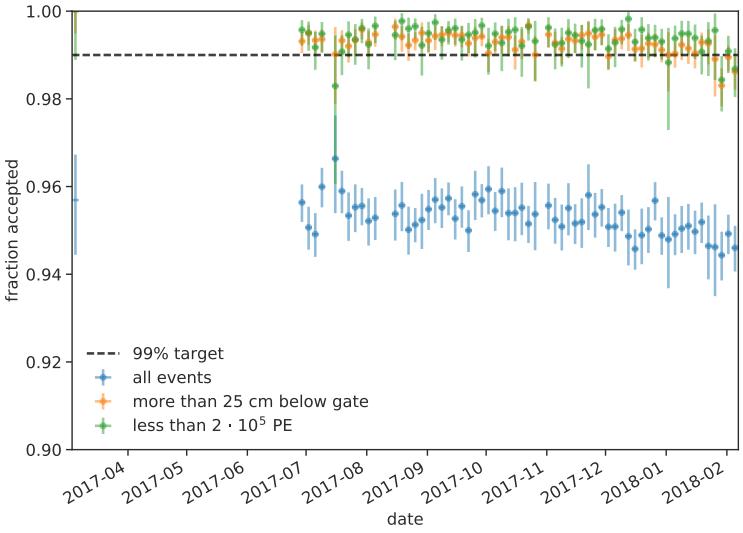

Figure 3.17: Estimated acceptance over time for different event categories using unblinded SR 1 science data. For the selection derived in this analysis, acceptance remains constant with a slight drop towards the end for all event categories.

In contrast to the charge signal, no significant loss in prompt scintillation light is observed. For example, α-decays of ^{210}Po, a daughter of ^{210}Pb, which happen on the PTFE reflector panels have S1 sizes as expected. Therefore, PSD techniques should also be applicable for surface events, which could help in discriminating between ER and NR interactions occurring on the PTFE panels. Another argument for investigating the applicability of PSD is the fact, that drift fields in TPCs tend to be weaker with longer drift lengths. This is a consequence of the challenge in needing to apply larger voltages to the field-generating electrodes to reach field strengths comparable to smaller-scale TPCs. A lower field strength results in a smaller discrimination power of the S2/S1 ratio while, at the same time, improving discrimination via PSD. As reported in [58, 59], PSD is able to compensate discrimination power losses of the S2/S1 ratio when combining both at field strengths below 200 V/cm.

In the following, ER and NR samples from XENON1T calibration data are taken to investigate the discrimination potential of PSD in the SI WIMP analysis ROI. A *prompt fraction* parameter, analogous to previous LXe studies [60], is calculated for S1 signals from both samples to see how it differs for ERs and NRs.

3.3.1 Sample selection

ER/NR samples for the PSD analysis are selected using the entireity of ^{220}Rn respectively NG calibration events recorded during SR 1 with $0\,\mathrm{PE} \leq cS1 \leq 200\,\mathrm{PE}$. To both of them, the same sets of cuts are applied as those used for defining ER and NR samples for fitting the detector's response as published in [34]. Loose, supplementary cuts, as indicated by the lines in which shows the discrimination space for both samples, are applied to remove outliers. An additional sample of surface events is defined by selecting interactions in SR 1 data which are reconstructed outside the TPC because of the finite resolution of the position reconstruction. Additional selection criteria are based on the criteria which are used in the analysis in [23] for defining a surface event sample.

3.3.2 Discrimination via prompt fraction

The applicability of PSD in XENON1T is investigated via the prompt fraction PF, defined as the fraction of a signal's area within the first 30 ns relative to the total area. While the data processor used for XENON1T analysis does, by default, not calculate this parameter, it can be estimated using area percentiles, which are available, in the following way:

$$PF = F_0 + \frac{F_1 - F_0}{t_1 - t_0}\left(30\,\mathrm{ns} + t_{\mathrm{start}} - t_0\right) \tag{3.3}$$

with t_0 and F_0 being the largest percentile and its corresponding fraction for which $t_0 - t_{\mathrm{start}} < 30\,\mathrm{ns}$ holds, and t_1 and F_1 being the smallest percentile and the fraction corresponding to it for which $t_1 - t_{\mathrm{start}} > 30\,\mathrm{ns}$ is true. Signals which have their entire area contained within 30 ns get a PF of 1 assigned to them. PF distributions for both the ER and NR samples are shown in Fig. 3.18. While they largely overlap, it can be seen, that NRs have larger PF values compared to ERs on average. This conforms to what is expected according to past LXe scintillation pulse shape studies, where NRs were found to have a larger effective singlet fraction than ERs at similar energies.

To account for the energy dependence of PF, all samples are divided into 10 even slices in $cS1$ between 0 PE and 200 PE. In each slice, a Gaussian is fitted to the corresponding PF distribution by minimizing the unbinned negative log-likelihood. Afterwards, 68 % confidence intervals are determined using the

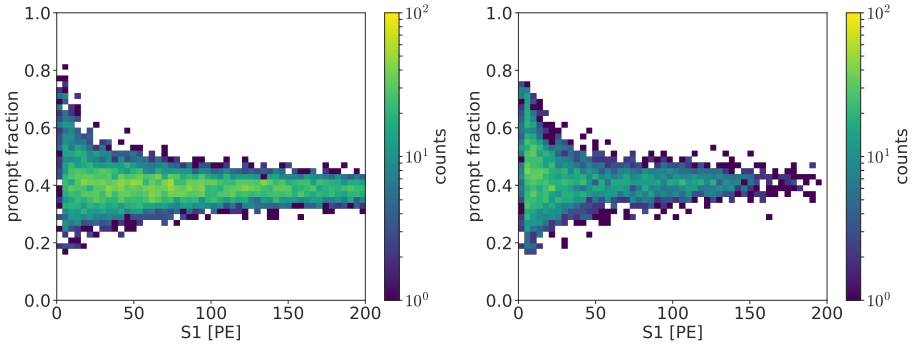

Figure 3.18: *PF* distribution for both the ER and NR calibration data samples. They become broader towards smaller S1 sizes because of low photon statistics. Left: ER distribution. Right: NR distribution.

profile likelihood method[1]

The results are shown in Fig. 3.19, where the difference in average *PF* between the ER and NR samples can be seen. Afterwards, the fit parameters extracted are used to calculate the receiver operating characteristic (ROC) curve for each slice (Fig. 3.20, left). It allows to state the ER rejection power for a given NR acceptance. Errors on the curve are determined by recalculating confidence intervals with MINOS such, that the 2D contour of the central 68 % region is determined instead of 1D error intervals with all other parameters profiled out. Following that, the extreme values of the Gaussian's μ and σ on the contour are used as the upper and lower ends of the corresponding parameter's 68 % confidence interval. While this method yields conservative intervals, as they contain a larger surface of the parameter space than the actual 68 % contour, it accounts for parameter correlations. This is necessary for stating a probability for both intervals to cover their true values *at the same time*. Errors on the ROC curves are estimated by a grid scan in (μ, σ), with 10 points per parameter distributed equidistantly across the rectangle defined by the parameter's confidence intervals. For each point on the grid, the ROC curve is calculated in order to determine the envelope of all curves for a given $cS1$ slice and sample. The envelope approximates the 68 % confidence region of the true ROC curve, which allows to determine confidence intervals for the ER rejection at a given NR acceptance.

Based on past publications, the benchmark is chosen to be the ER rejection at 50 % NR acceptance. Fig. 3.21 shows its variation over $cS1$. The rejection power

[1]For further information regarding this method, the reader is referred to [61].

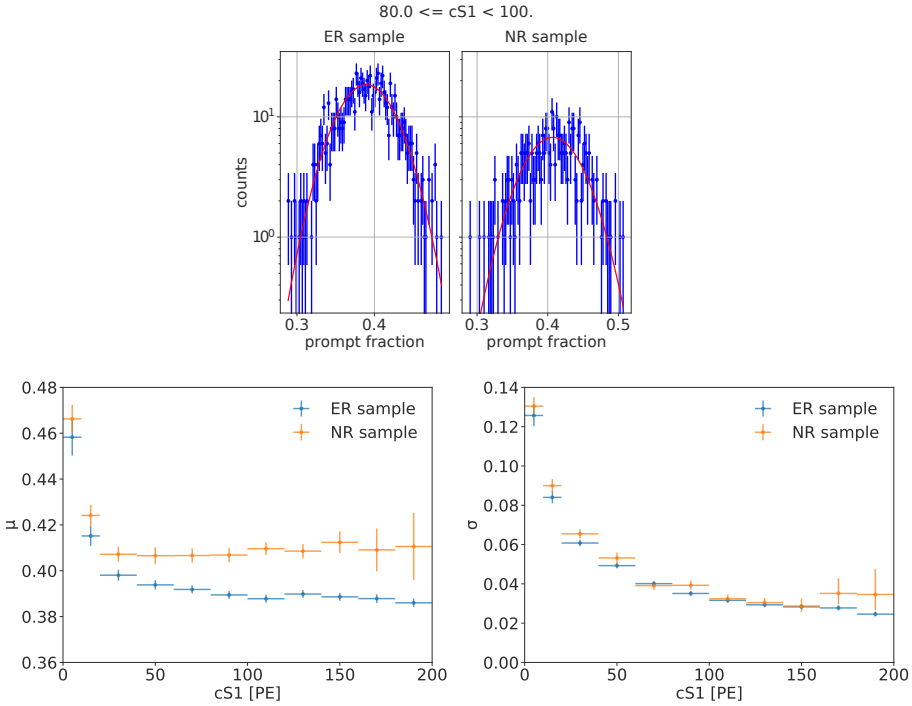

Figure 3.19: Fit results for both ER and NR samples in each $cS1$ slice. Top: Fits in $[80\,\text{PE}, 100\,\text{PE}]$ slice, shown as a typical example. Bottom-left: μ of fitted Gaussians. The larger PF of NRs compared to ERs is evident. Bottom-right: σ of fitted Gaussians. Both samples have comparable PF distribution widths.

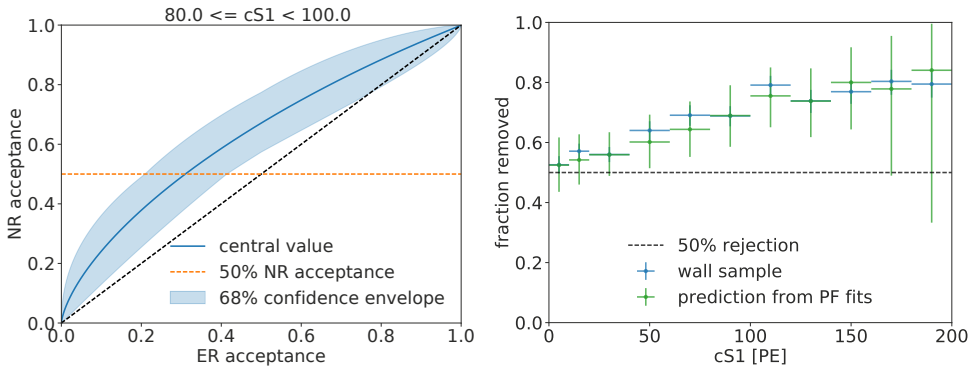

Figure 3.20: Left: Example ROC curve when using *PF* for discrimination between ER and NR by classifying events above a certain *PF* threshold as NRs. Right: Rejection power against ER events at 50 % NR acceptance. Included are both the estimate based on the *PF* distribution fits as well as the fraction of the wall event sample removed.

can reach up to $\sim$ 75 % above 100 PE, while it deteriorates towards smaller S1 signals as the *PF* distribution broadens because of limited photon statistics. Compared to the study presented in [60], where the *PF* parameter definition was optimized by varying the interval which constitutes the beginning of a signal, discrimination is slightly worse. The reason for this is, that the definition of *PF* here, while based on the outcome of that study, is *ad hoc* without any further optimization. Furthermore, the XENON1T PMT transit time spread (TTS) is larger on average compared to the PMTs used in the study, which results in a worse temporal resolution and, consequentially, increases the variance of *PF*.

To test the applicability of PSD for discriminating against surface interactions, the *PF* distribution of the surface event sample is compared to the one of the ER sample in every *cS*1 slice by applying a two-sample Kolmogorov-Smirnov test. The p-values, as they can be seen in Fig. 3.21, indicate, that 10 out of the 11 slices are compatible with the hypothesis, that both samples have been drawn from the same distribution, at 95 % C.L. However, when assuming that each slice is statistically independent of each other, the probability for those 3 slices to fail the test is smaller than 10^{-7}. This indicates an actual difference between the distributions which could be caused by field inhomogeneities close to the PTFE panels leading to modified singlet fractions for interactions occurring there. Another potential reason are photon transit time differences, as events in the ER sample do not include the regions at or close to the panels,

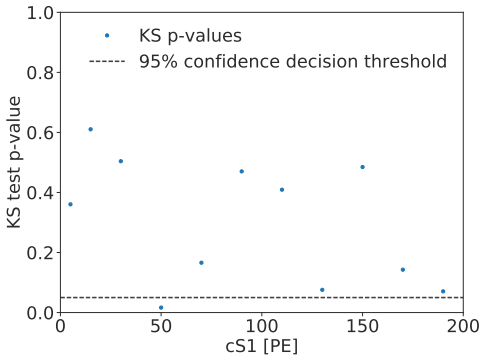

Figure 3.21: Comparison between the PF distributions of the ER and wall event samples. For each $cS1$ slice, the two-sample Kolmogorov-Smirnov test is applied to yield a p-value.

while the inverse is the case for the surface event sample. Nonetheless, both distributions are very similar, which is proven by applying the PF thresholds corresponding to 50 % NR acceptance in each slice to the surface event sample. As seen in Fig. 3.20, they are compatible with the values as expected from the ROC curves.

In addition to purely using the PF parameter for discrimination, another investigation is made concerning the concurrent use of PF and the S2/S1 ratio. Quadratic discriminant analysis (QDA)[2] is utilized to train a classifier in each of the previously defined $cS1$ slices, using all of the ER and NR samples to train them. The QDA classifier assumes PF and $\log_{10}(cS2/cS1)$ of each class to be distributed according to a multivariate normal distribution. It uses mean and covariance matrix as estimated from the samples themselves as the corresponding parameters of each class' distribution. Afterwards, a new data point can be classified by calculating the log-likelihood for each multivariate normal distribution. Usually, the new point is matched to the class which gives the largest log-likelihood value, but in the case of two classes, one can calculate the log-likelihood ratio between the two distributions and use it as a classification parameter, which is analyzed in the same way as PF above.

Results for the QDA distribution fits are shown in Fig. 3.23. As for PF, the classification parameter distributions are reasonably well described by a normal distribution. For comparison purposes, the same analysis is repeated using the S2/S1 ratio only for discrimination. The extracted ER rejection power of both (Fig. 3.24) is comparable, with the QDA classifier performing better at S1

[2] See, for example, [62], page 106 and following.

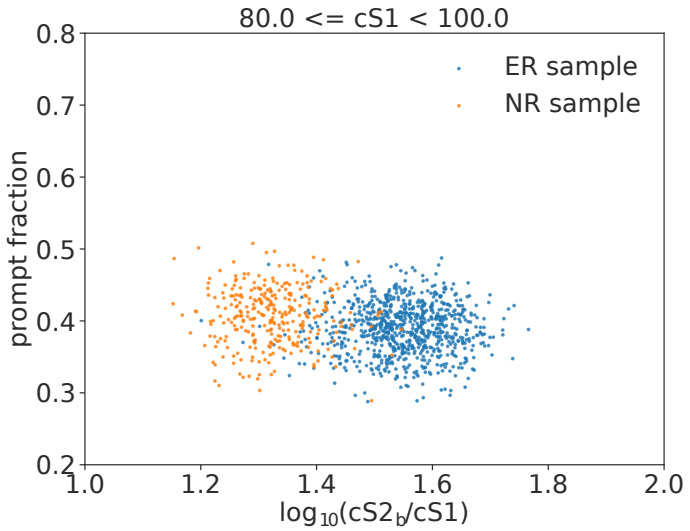

Figure 3.22: Example plot of the parameter space used for QDA classification. A negative correlation between S2/S1 ratio and *PF* is visible, which can be employed to enhance ER/NR discrimination.

sizes below 50 PE. For more precise values which could clearly indicate the superior method for bigger S1 signals, a larger amount of sample events would be needed, especially NR events. Otherwise, it cannot be guaranteed, that QDA yields the optimum classifier it can return due to a lack of statistics.

3.4 Summary and outlook

In this chapter, three different analyses are presented. They regard the identification and mitigation of background signal sources which have the potential to impact physics analyses with XENON1T data.

The first analysis uses waveforms without physical signals, called noise waveforms, to identify noise sources and to estimate the stability of electric noise during the XENON1T SRs. This is done by calculating the noise waveform discrete Fourier transform (DFT) coefficients. The coefficients yield both amplitude spectra and phases of noise components, allowing to use the former to quantify changes in noise conditions and the latter to search for parameters correlating with phase, which provides a way to identify electric noise sources. As in a preceding analysis [55], two sources are identified based on phases of

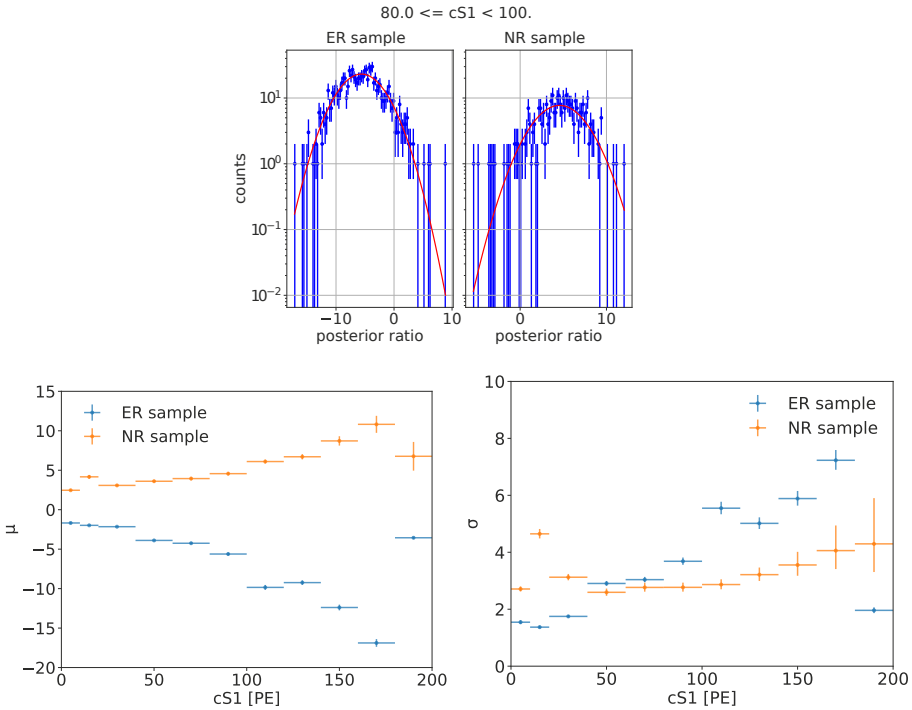

Figure 3.23: Fit results for both ER and NR samples in each $cS1$ slice, using the output of each slice's QDA classifier. Top: Fits in $[80\,\mathrm{PE}, 100\,\mathrm{PE}]$ slice, shown as a typical example. Bottom-left: μ of fitted Gaussians. Bottom-right: σ of fitted Gaussians. The rightmost data point of each parameter deviates markedly from the trends outlined by the preceding points. The very low number of NR sample events in the rightmost slice is the most likely cause, as it negatively impacts the quality of the trained classifier.

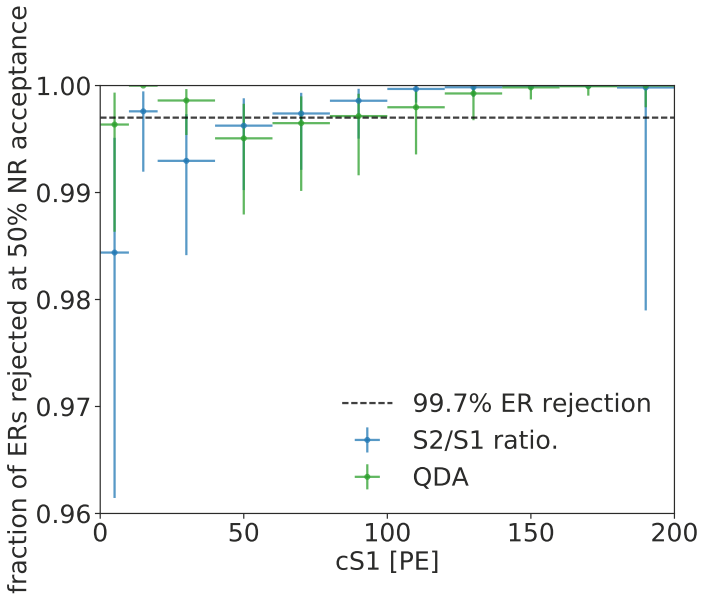

Figure 3.24: Comparison of ER rejection power at 50 % NR acceptance between QDA and S2/S1 ratio only. For both methods, the rejection power is extracted from the ROC curves of each slice. For S1s smaller than 50 PE, QDA seems to perform better, while it is ambiguous at larger sizes. For comparison, the average ER rejection power stated for the combined SR 0 and SR 1 SI-WIMP analysis is shown as a dashed line [23].

features in the amplitude spectra correlating with PMT cabling maps: the digitizers, and the HV boards supplying the PMTs with power. The digitizers are associated with a single peak in the amplitude spectrum at about 25 kHz, while the HV boards are matched to a series of peaks at multiples of ~ 104 kHz. Noise induced by the HV boards is mitigated by interposing low-pass filters between the PMTs and the boards. The impact of those filters is observed when evaluating the evolution of different noise components over XENON1T commissioning, SR 0 and SR 1, where a reduction of ~ 22 % on average per PMT channel is visible. Other than that, noise conditions are generally stable during the the periods mentioned above, with exceptions being sudden jumps which coincide with PMT signal cable operations and effects which could be explained by temperature variations of the DAQ electronics. The techniques used here for noise analysis are planned to be applied and expanded upon in XENONnT. As most of the XENON1T hardware is also going to be utilized in XENONnT, the identified noise components are expected to appear again in some capacity.

In the second analysis, interactions occurring in the GXe phase of the XENON1T TPC, which can produce S2-like signals, are identified by the AFT parameter. Parts of the GXe phase are closer to the top array compared to the amplification region, where actual S2 signals are generated. Thus, signals of gas interactions have an, on average, larger AFT value compared to normal S2s. Based on this fact, an event selection is defined using ^{220}Rn and neutron calibration data to remove gas phase interactions for various analyses in XENON1T. The AFT parameter is corrected for spatial variations and PMT afterpulse (AP) effects, after which the 0.5 % and 99.5 % percentiles of the AFT distribution are determined for slices in $S2_{\mathrm{raw}}$. The evolution of the percentiles with respect to $S2_{\mathrm{raw}}$ is then fitted with an empirical model function to retrieve an analytic description of the selection boundaries.

Based on the chosen percentiles, acceptance for non-gas interactions ought to be 99 %. This value is confirmed with calibration data which has not been used for defining the cut. It is constant over almost the entire $S2_{\mathrm{raw}}$ for which the selection is valid, dropping locally by 1 percentage point at most. The rejection power against gas interactions is estimated using a sample of gas events. Above around 600 PE in $S2_{\mathrm{raw}}$, all gas interaction events in the sample are removed. Also, the dependence of the selection acceptance on event coordinates and time is investigated. Both are homogeneous within most of the detector volume and time frame used for the XENON1T analyses.

A selection based on AFT is also going to be relevant for XENONnT and other

future xenon dual-phase TPCs because of their similar geometries implying similar gas interaction signatures. Depending on the precise electrode layout, one might be able to tune the TPC field configuration to prevent gas phase interactions from resulting in a proportional scintillation signal. In retrospect, it might have been possible to do so in XENON1T by setting the top PMT array screening mesh voltage to a value closer to the one used for the anode. As a consequence, it could be worthwhile to investigate the reduction of gas interaction signals via this method during XENONnT commissioning. While an AFT-based cut is not an issue for S2 sizes at $\mathcal{O}(1000\,\mathrm{PE})$ and above, the AFT distributions of smaller S2s and gas interaction signals overlap increasingly towards smaller sizes. Because this results in a correspondingly lower rejection power, preventing gas phase interaction signals in the first place would be more efficient.

The third analysis is primarily motivated by background event populations which leak into the NR region in $(cS1, cS2_b)$ space, such as random coincidences and PTFE surface ERs. In order to remove such events, a prompt fraction parameter, PF, has been defined to investigate the effectiveness of PSD techniques in discriminating against these populations. An *ad hoc* definition based on results presented in [60] already succeeds in rejecting surface events caused by ^{222}Rn daughter decays, especially ^{210}Pb, occurring on the PTFE panels delimiting the TPC. At 50 % NR acceptance, the rejection power against ERs can reach up to $\sim$ 75 % for $cS1 > 100\,\mathrm{PE}$ while still being more effective than random classification for smaller S1 signals. Combining PF with the S2/S1 ratio is investigated by utilizing QDA to yield a classifier which incorporates both. Results indicate, that the resulting classifier indeed performs better than the currently used S2/S1 ratio at S1 sizes below 50 PE, while both are comparable at high energies.

The investigation of PSD with XENON1T data has important implications for future XENONnT analyses. Depending on how many ^{222}Rn daughters are going to remain on the XENONnT PTFE panels, PSD could help in extending the fiducial volume towards the latter. In addition, PSD also has the potential to reject random coincidences of lone S1 and S2 signals as the former are, based on the relative amount of ER vs. NR background, usually caused by ERs. Finally, as shown in [59], PSD would significantly improve ER rejection in general if the electric field within the drift volume of the TPC were to be about 100 V/cm or lower. While the designed field strength of XENONnT is above that value, HV issues [63] arising during operation might necessitate to lower it. Applying the voltages needed to the TPC electrodes is by far no trivial task, as evidenced by the amount of R&D conducted regarding electrode field emissions,

for example.

A potential way for integrating PSD in a XENONnT analysis would be to define a dedicated prompt fraction parameter at data processor level which does not rely on interpolating other signal parameters. Its distribution could then be modelled using sufficient amounts of ER and NR calibration data, with the model being used as a term in a likelihood function. Initially, the effectiveness of PSD will need to be assessed again because of XENONnT's TPC being larger than the one of XENON1T, resulting in longer photon transit times increasing the variance of any prompt fraction parameter.

4 The HeidelbergXenon system

Built to conduct detector R&D for future-generation liquid noble gas detectors, the HeidelbergXenon (HeXe) system consists of a 100 g-scale xenon TPC. In addition, it contains a gas recirculation system for purifying xenon and injecting samples of various kinds. With previous iterations of the system having been used for alpha-decay measurements [42, 64] and testing radon removal from LXe via distillation techniques [65], HeXe is currently employed in studies regarding detector material treatment and xenon microphysics.

In the following, the different sub-components of HeXe are detailed together with the data acquisition chain and the surrounding computing framework in order to provide crucial information for the measurements and analyses presented in Chapter 6.

4.1 Time projection chamber

At the core of HeXe is a TPC with a cylindrical drift volume measuring 56 mm in diameter and 50 mm in height at room temperature (illustrated in Fig. 4.1 and Fig. 4.2). It is defined by a cylinder made out of PTFE and two stainless steel grids with hexagonal tiling (gate and cathode at the top respectively bottom of the volume), held by rings made out of the same material. Both grids are 0.1 mm thick, with the pitch of the hexagonal cells, which have a minimal diameter of 1.0 mm, being 1.12 mm. Taking thermal contraction into account, the drift volume, when filled completely, contains about 344 g of LXe at −107.5 °C.

The TPC has been designed for the cylinder to be easily exchanged to facilitate trials where different surface cleaning procedures are tested for their impact on LXe purity. These measurements are described in [66]. PTFE has been chosen for the material because it is both non-conductive and highly reflective at

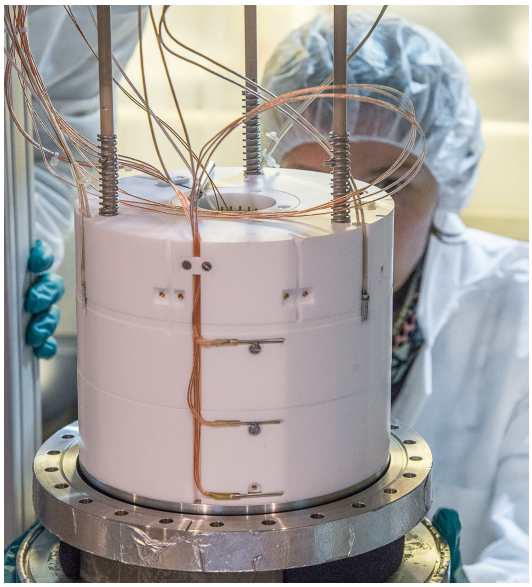

Figure 4.1: Photo of the HeXe TPC during an opening of the cryostat housing it. It shows how the PEEK rods, the metal plate they are connected to, and the springs mounted on the rods are used to suspend the assembly and to hold it together.

178 nm, which is close to the peak scintillation wavelength of LXe [19], maximizing light collection. It is also commonly used in large-scale xenon TPCs for these reasons.

The cathode and gate grids are needed in order to create the drift field during dual-phase operation. To increase the field's homogeneity, three stainless steel field shaping rings enclosing the PTFE cylinder are placed equidistantly between the two grids. Both grids and rings are connected in series via 1 GΩ resistors to define a gradual drop in electric potential over the length of the drift volume when applying a voltage between gate and cathode, resulting in a homogeneous drift field. Another grid, the anode, which is identical to the gate and cathode grids, is placed at a distance of 5 mm above the gate. Gate and anode together define the extraction field region, with the the LXe-GXe interface between them. During single-phase operation, the grids are utilized to set up varying field configurations for measuring field-dependent parameters.

Light signals from particle interactions with the xenon target are detected by two Hamamatsu R6041-406 PMTs facing the drift volume and extraction field region, with their windows being placed 4 mm above the anode respectively

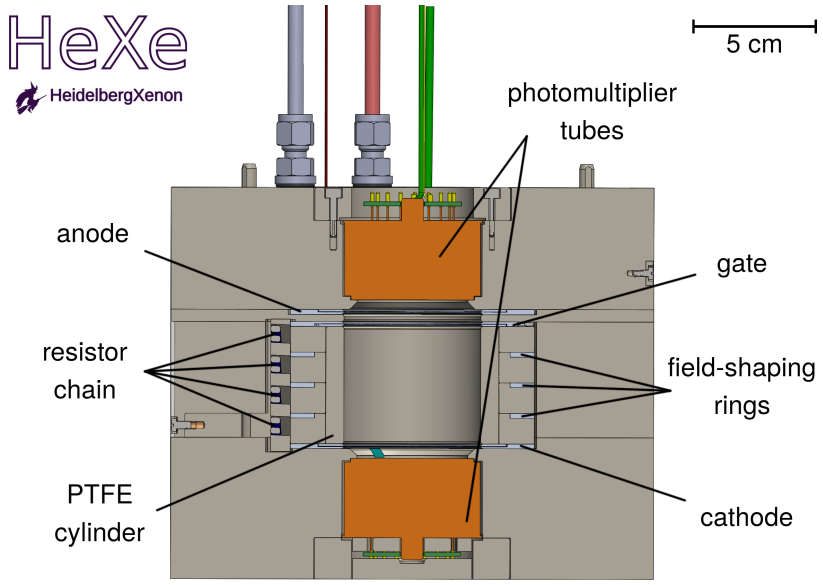

Figure 4.2: Cross-section of the HeXe TPC. Sub-components are described in the text.

below the cathode. Both have, according to manufacturer specifications, high quantum efficiencies (QEs) of about 39 % at 178 nm and TTSs of 0.75 ns, making them well-suited for precision timing measurements. For calibration purposes, two optical fibers are led to about 20 mm below the gate, pointing directly at the outer side of the cylinder. The latter acts as a diffusor for light passing through the fibers, resulting in near-equal illumination of both PMTs when the volume between them is filled entirely with a single-phase medium.

Both the grids and PMTs are supplied with HV via iseg NHQ series modules, which are controlled via software (see Section 4.4). A hardware current threshold is set which causes a module to immediately shut down a channel if the current flowing through it exceeds a certain value, protecting the connected device. Such a triggered shutdown is called a *trip*. Trips occur when HV components develop a short or experience electrical discharges. They also happen when a PMT receives large amounts of light and creates a correspondingly large signal.

The entire TPC is encased in a PTFE filler, divided into slices, with a diameter of 19.8 cm to minimize the amount of LXe needed for operation. It contains grooves and holes for guiding cables respectively fibers and providing a way for the xenon to enter and leave the TPC. On the outer surface of the filler,

four Pt100 sensors are mounted at varying heights in order to monitor temperature. Also located at the outer surface are four custom-made capacitive levelmeters of varying lengths which are used to measure the height of the LXe phase during operation. As the filler is not liquid-tight, the level at the outer surface equilibrates to the level inside the TPC. One of the levelmeters, called *long levelmeter*, goes along the entire length from the bottom of the filler until slightly above the anode. It is used to measure the LXe level during filling and recuperation. Two levelmeters are called *short levelmeters* and span over the amplification gas gap. They are utilized to monitor the LXe height in the gap, and, together with a *medium levelmeter*, they can be used to adjust the level of the system. The medium levelmeter spans the same range as the short ones, but continues upwards above the top PMT window. Thus, it is able to indicate single-phase operation.

To hold the assembly together, the PTFE filler is pierced by three rods made out of PEEK. They are screwed into a metal plate against which the filler is pressed via springs attached to the rods themselves to avoid movement due to buoyancy in LXe. The entire setup is suspended, via the rods, from a support structure which links it to the other HeXe facilities. The effective length of the rods can be adjusted in order to level the setup.

4.2 Support structure and cryogenics

The support structure the TPC is suspended from consists of a double-walled CF flange (DN200) onto which four pipes are welded. It serves as a central point connecting the TPC to the gas recirculation system, a cooling tower for gas liquefaction and to feedthroughs for cables and optical fibers. It also provides mounting points for equipment which needs to be connected to the inner cryostat volume.

The CF flange is used to fasten a cylindrical, double-walled cryostat, measuring 60 cm (54 cm) in outer (inner) height and 27.6 cm (20 cm) in outer (inner) diameter, to the support structure while raising it over the TPC. The insulation vacua of both the cryostat and the CF flange are continuously pumped during operation using a turbomolecular pump connected in series with a roughing pump. Their internal pressure is monitored using a vacuum sensor. Together with 25 layers of multi-layer insulation on the vacuum-facing side of the inner cryostat wall, the insulation vacua reduce heat intake such, that a stable LXe phase can be maintained. A hot plate, integrated into the bottom plate of

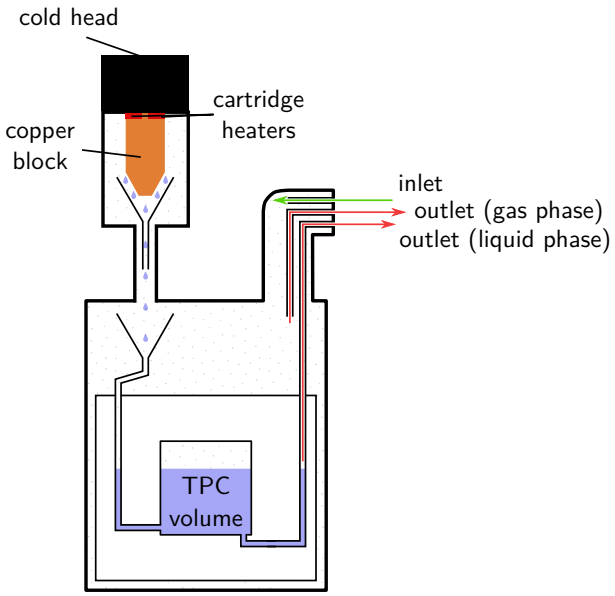

Figure 4.3: Diagram which shows the xenon flow within cryostat and support structure. The outlets, which can be opened and closed separately, lead to the gas purification system, while it is vice-versa for the inlet.

the cryostat, can be used to assist in xenon recuperation by speeding up LXe evaporation.

Flanges are attached to the four pipes which contain the facilities mentioned in the following. TPC grid and PMT HV cables are connected to the outside using welded SHV10 respectively SHV feedthroughs. A multipin feedthrough is used for levelmeter, Pt100 and PMT signal cables. During the course of the measurements presented in this thesis, the feedthrough type for the PMT signals was changed to a welded BNC feedthrough to mitigate electric noise. For the two optical fibers used for PMT calibration, an FC/PC feedthrough is employed. In addition to the facilities for connecting cables to the outside, a turbomolecular pump is connected directly to one of the pipes. This is done to have as little piping as possible between the pump and the cryostat when evacuating the latter. Also, a digital manometer for monitoring the pressure inside the cryostat and several mechanical safeguards (described in Section 4.4) are connected to the pipes. Finally, one of the flanges contains ports for xenon to enter respectively leave the cryostat.

The general flow of xenon inside both cryostat and support structure is illus-

trated in Fig. 4.3. It has been designed to facilitate the purification of the xenon within the TPC. Liquefaction takes place on the surface of a ribbed copper block inside a cooling tower which is mounted on top of one of the pipes connected to the CF flange. The block is cooled down using a PTR driven by a Leybold COOLPAK 6000-1 helium compressor which delivers a cooling power of 200 W. Three cartridge heaters, which are regulated by a PID controller and, in total, provide up to 300 W of heating power, are sandwiched between the block and the cold head. They allow to set and stabilize the block's temperature, which in turn affects the rate of xenon liquefaction. Four Pt100 sensors, installed at various points within the block, monitor the temperature, with the one closest to the block's surface being used as a reference for the PID controller. Sensors and cartridge heaters are connected to the outside via a multipin feedthrough installed at the cooling tower.

After liquefaction, the xenon drips off the copper block and is directed by a series of funnels into a groove drilled through the PTFE filler surrounding the TPC as seen in Fig. 4.3. The groove ends inside the TPC at a point slightly above the bottom PMT. Extraction into the gas recirculation system can take place at two different points, which are connected via PTFE pipes to corresponding ports on the support structure pipe flanges. One of them is at the top of the GXe phase in the cryostat. The other one is directly below the bottom PMT in the LXe phase. During regular operation, only the liquid phase output is used to promote mixing of purified xenon with the xenon already inside the TPC.

4.3 Gas recirculation system

The gas recirculation system, depicted in Fig. 4.4, is a collection of facilities for storing the xenon used in HeXe and continuously purifying it in a recirculation loop. It also houses a ^{83m}Kr [47] calibration source and has several access ports which, for example, allow to draw samples and to connect additional appliances.

Recirculation is driven by a KNF N 143.12 double diaphragm pump. Two buffer volumina, one connected to the pump inlet and the other one connected to the outlet, absorb pressure shocks resulting from switching the pump on respectively off and dampen flow rate variations. A gas line which bypasses the pump is used to control the mass flow through the system by allowing part of the compressed gas to flow back through an adjustable valve.

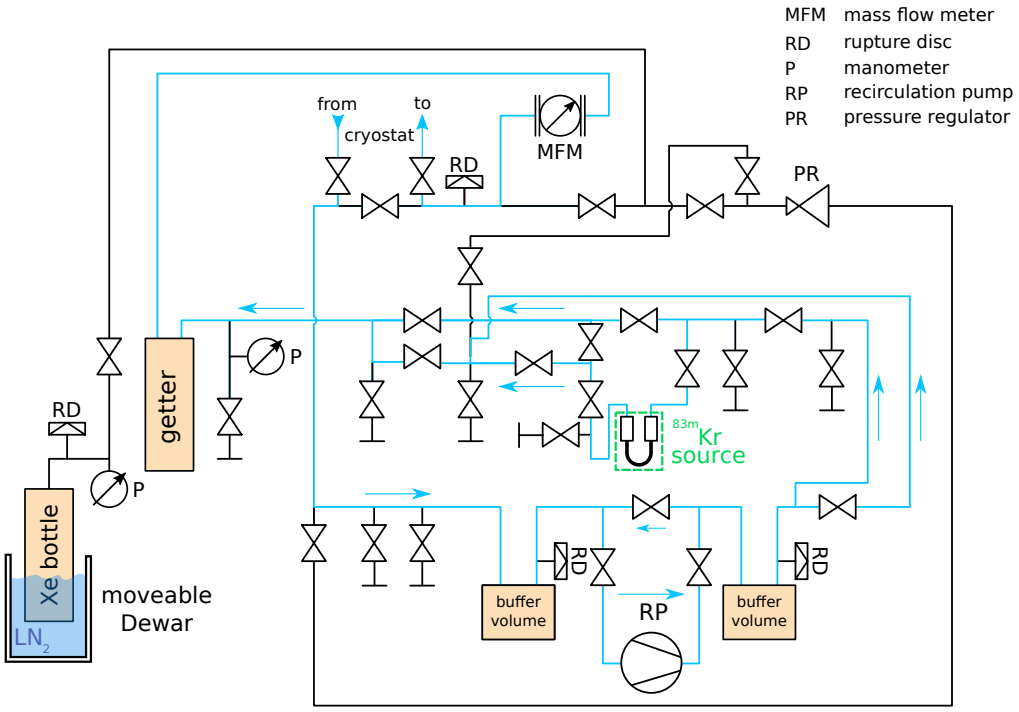

Figure 4.4: Diagram of the gas recirculation system. The colored lines and arrows indicate the xenon flow during a typical ^{83m}Kr calibration measurement.

The pump is connected via two parallel gas lines to an SAES PS3-MT3 rare gas purifier used for removing impurities, such as water and oxygen, from the xenon flushed through. One line, named *main line*, leads directly to the purifier, while the other one, named *sampling line*, is used to introduce radionuclides into the xenon stream to measure their decays inside the TPC. One of these nuclides is ^{83m}Kr. It is inserted by directing the flow of xenon through a bent pipe installed at the sampling line which houses a handful of zeolite beads containing ^{83}Rb [67], which decays into ^{83m}Kr emanating out of the beads. Particle filters at both the pipe inlet and outlet are used to avoid potential bead fragments to contaminate the recirculation system and other parts of HeXe.

At the point where the two lines merge, a digital manometer is used to monitor the gas pressure at the gas purifier inlet. The outlet is connected to a mass flow meter (MFM) through which the xenon flows before it returns, during regular operation, to the cryostat. When recuperating, the xenon is directed towards a 9.5 l stainless steel sampling cylinder cooled with liquid nitrogen into which it is cryopumped. The cylinder is suspended from an S-type load cell used to monitor its weight. It is able to contain all the xenon used in HeXe, which corresponds to about 6.5 kg. Usually, between 2 kg and 4 kg are put to use during operation depending on the desired liquid phase height inside the TPC.

Filling xenon into the system is accomplished by opening the cylinder, when it is at room temperature, to a high-pressure line of the recirculation system connected to the inlet of a pressure reducer. The reducer's outlet is connected to a line leading to the recirculation pump inlet, such that xenon coming from the cylinder has to pass through both purifier and MFM before entering the cryostat.

4.4 Slow control system and safety precautions

The presence of LXe, which is a liquefied rare gas, necessitates measures for avoiding loss of xenon and to ensure the safety of people operating HeXe. These consist of mechanical safeguards and sensors which continuously monitor critical system parameters. The latter are read out by a slow control system which is capable of sending alerts in case these parameters approach dangerous values.

To minimize the risk of xenon loss, the cryostat volume is connected via a pipe with a diameter of 2.54 cm containing an in-line rupture disk to an evacuated 480 l buffer vessel, from which it can be recuperated. The vessel is able to hold about 5 kg of xenon at room temperature, which is more than is used for both dual-phase and single-phase measurements. If the pressure inside is rising towards dangerous values, which could damage equipment, the rupture disk bursts open, causing the xenon to flow into the vessel. Should the pressure still rise too quickly, an overflow valve, which is connected to the support structure, releases xenon in a controlled fashion to the outside and closes itself the pressure goes down again. For additional safety, rupture disks leading to atmosphere are mounted at several points of the gas recirculation system and also at the support structure if either the overflow valve is not sufficient in releasing pressure quickly enough, or if local pressure spikes occur which might damage the system otherwise.

Detector parameters are continuously read out and monitored by a program developed in LabVIEW [68], which constitutes the main part of the slow control system. The parameters in question are:

- Pressure inside the cryostat and at the gas purifier inlet
- Cryostat / support structure insulation vacuum pressure
- Heater PID reference Pt100 temperature, set point and power output
- MFM readings
- Levelmeter capacitances
- TPC and copper block temperatures
- Sampling cylinder weight

The program's interface allows to select which sensors to read out and displays parameter evolution plots. Every read out value is stored in a periodically backed-up PostgreSQL [69] database for later access. The database runs on the same computer as the LabVIEW program in order to be able to save parameter readings during network outages and keep the detector running.

Furthermore, two sets of thresholds can be set for each parameter which correspond to different severity levels in case readings go past them, called *warning* and *alarm thresholds* in the following. When warning thresholds are passed, notification emails are sent to a customizable list of addresses. If alarm thresholds are passed, SMS messages are sent to select cell phone numbers in addition by utilizing an interface to a pre-existing monitoring infrastructure set up by

the Max-Planck-Institut für Kernphysik (MPIK) IT department, which is based on Nagios [70]. The same infrastructure, in turn, monitors the computer on which the program and database are running on and sends out emails and SMS messages in case either of them is not responsive.

The slow control system is completed with a tool written in Python by [71], which is used to control the HV modules supplying the TPC grids and PMTs. It operates on the same machine as the LabVIEW program. A graphical user interface allows to set voltages and trip currents and to load ramp schedules used to automate voltage changes. In case one of the HV channels trips, the tool can be set to send email and SMS notifications and to attempt to ramp the affected channel back up. It also interacts with the above-mentioned database by regularly storing voltage and current readings and retrieving cryostat pressure values. If the most recent pressure value is lower than 1.2 bar or older than 5 minutes, all HV channels are ramped down. This is done in order to avoid damage due to electric sparks, which are caused by the breakdown voltage of GXe approaching a minimum when going to lower pressures according to the Paschen law [72].

The way in which all these subsystems are connected which each other is visualized in Fig. 4.5. It also includes the DAQ systems which are described in the following section.

4.5 Data acquisition and storage

PMT signals are fed into the signal processing chain as depicted in the top half of Fig. 4.5. They first enter a custom-made voltage amplifier module consisting of four channels with at least two identical outputs each. Two of the channels have a variable amplification factor, or *gain* which can be set by the user, while the other channels have a fixed gain of 10. During pulse shape measurements, the top PMT is connected to one of the fixed gain channels, while the bottom PMT uses one of the variable gain channels at its lowest setting (factor ~ 2.2 amplification). Regardless of the channels used for a specific measurement, one output is connected to a digitizer used for waveform recording, while another one is connected to a series of modules which allow to monitor PMT signals on-line and to send trigger signals to the digitizers.

Two different digitizers can be used for recording waveforms, both made by CAEN. For dual-phase measurements, such as those in [66] and most of the

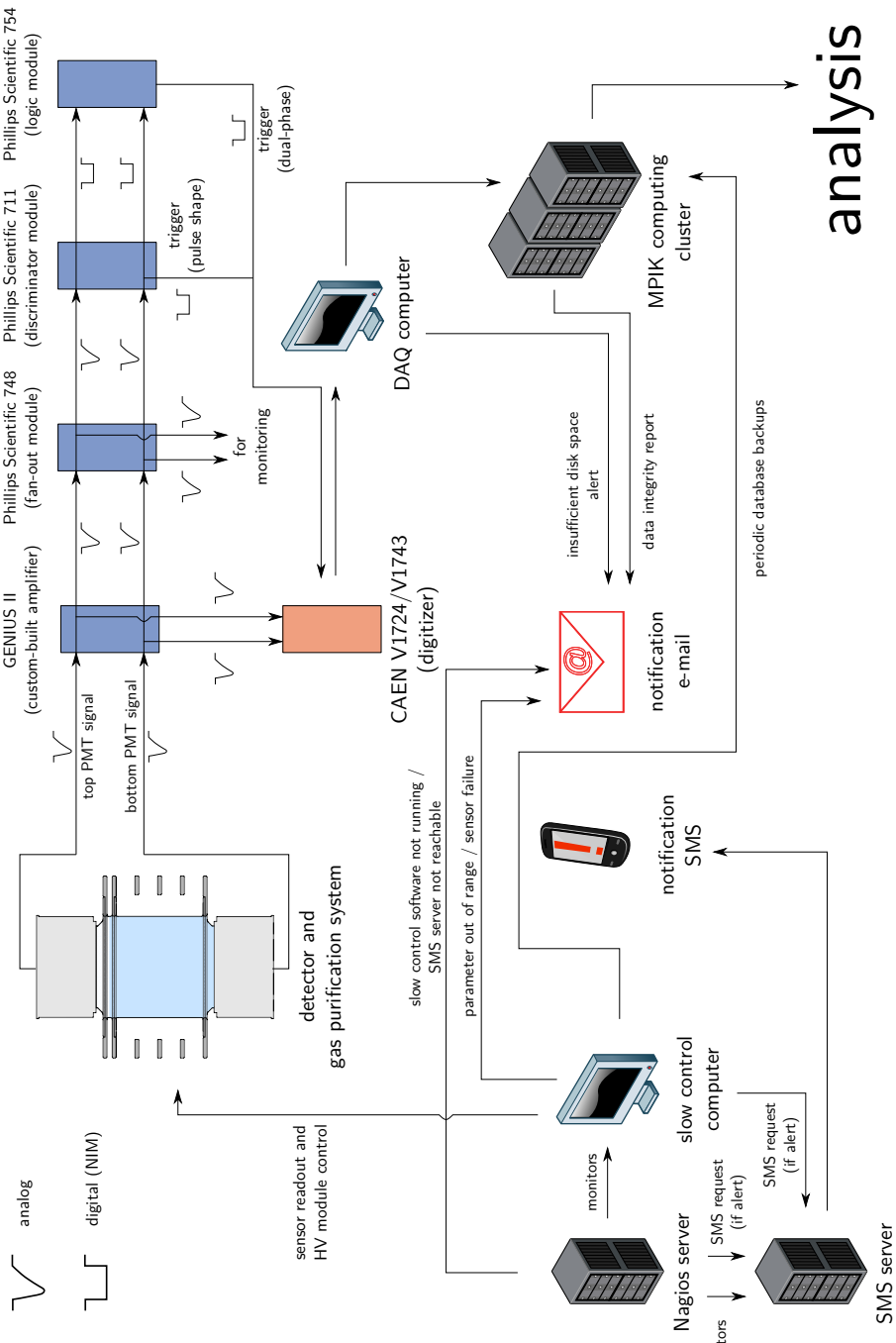

Figure 4.5: Signal and data flow between HeXe subsystems, which includes the slow control, the DAQ, as well as the systems used for data processing.

PMT calibration measurements, a V1724 module [44] has been used, the same type as employed in XENON1T (see Section 2.3). The pulse shape measurements in this thesis have been made with a V1743 module [73] instead. This module contains 8 switched capacitor ADC boards, with two channels each for a total of 16 simultaneously recordable channels. The boards use time interleaving to sample with an effective rate of 3.2 GHz, the bandwidth being 500 MHz. They record signals with 12 bit resolution over a dynamic range of 2.5 V with window sizes up to 320 ns. While the boards have a minimum amount of dead time up to 125 µs per trigger, due to digitization being slow compared to the V1724 module, it is not of relevance for the pulse shape measurements.

The amplifier outputs which are not connected to the used digitizer are fed to a 4-way fan-out module to replicate them. One of the fan-out outputs per channel goes into a discriminator which outputs a standard NIM signal if the corresponding PMT signal passes a certain threshold. The discriminator outputs of both PMT signal lines are, in turn, lead to a logic unit which creates a standard NIM signal if the NIM signals it receives overlap with each other. The signal coming from the logic unit is used to trigger the digitizer in dual-phase measurements. For pulse shape measurements, the discriminator output of one of the PMTs is used instead for reasons outlined in Chapter 6. Remaining, unused outputs of the modules are utilized for on-line signal monitoring via oscilloscope.

Digitizers are read out via optical link, using a dedicated computer on which recorded waveforms are buffered before being uploaded to a computing cluster located at MPIK for further processing. Data acquisition is controlled by the HeXeRecorder (HeXeR) software, written in C++, which has been programmed from scratch for this purpose. It supports, at the time of writing, readout of CAEN digitizers from the x724 and x743 families running with the standard waveform recording firmware by utilizing libraries provided by the manufacturer. Acquisition settings for each board can be set with JSON configuration files, covering most of the parameters which can be customized. In addition, alternative acquisition modes, such as the digitizer generating its own trigger, can be utilized if required.

After having uploaded the data onto the cluster, a script can be run to register it into a database which stores names and checksums for every single file. That script is also capable of checking whether the currently computed checksum of a previously registered file matches its initial value. In case of mismatches

or missing files, a notification email, which includes the names of the affected files, is sent to a customizable list of addresses.

4.6 Data processing

Recorded waveform data is analyzed on the MPIK computing cluster via batch jobs which run the *walpurgisnacht* data processor originally developed for the measurements in [64]. It is capable of processing binary files corresponding to the standard output formats of the V1724 and V1743 digitizers and, in addition, the modified V1743 format of HeXeR. Files placed within a common folder are treated as belonging to a single dataset and can be processed in parallel via multithreading. Results are stored as ROOT TTrees, with TTrees of files from the same dataset being merged. Different analysis modes, depending on the user, can be selected, including a plotting mode for displaying raw waveforms together with the corresponding output from the data processor. If not specified otherwise, the default analysis mode and parameter settings as used for dual-phase measurements are referred to. Parameter changes and features exclusive to the pulse shape measurements are outlined in Chapter 6.

Files are worked through on an event by event basis. After extracting waveform samples for each channel and additional information provided by the data format, baseline voltages are estimated by taking the average of the first 25 valid samples of a waveform. These baseline voltages are then subtracted from the waveforms of the channels to which they belong, yielding one *baseline-subtracted waveform* per channel. The latter are summed up to calculate the *sum waveform*. Afterwards, PMT signals are being searched for in both types of waveform with a peak finding algorithm. For convenience, the following algorithms are illustrated for signals with positive polarity, but they can be used analogously for negative polarity signals as well by flipping the signs of the recorded waveform samples.

The peak finding algorithm detects signal candidates in several steps (Fig. 4.6). First, the standard deviation of the first 25 valid samples of the waveform where signals are to be searched for, σ_b, is calculated. Subsequently, a threshold of $5\sigma_b$ is used to search for voltage excursions which indicate potential PMT signals. To identify such an excursion, the voltage must both rise above the threshold and go below it again afterwards, with the threshold crossings delimiting the *excursion interval*. Then, for every excursion interval, the maximum voltage U_{max} is determined and 19 different voltage thresholds are calculated, spaced

equidistantly between $5\sigma_b$ and U_{max}. The number of thresholds has been decided upon based on peak finder studies where this number was varied. Each of these thresholds is then used in separate iterations to find local maxima by determining intervals within which the voltage is above the corresponding threshold. The locations of the maximum voltage values in each interval found are then retrieved. Maxima and their positions are retained as signal candidates, which are referred to as *peaks* from now on, if they are found in at least 25 % of the 19 iterations. The exception is the location of U_{max}, which is always regarded as a peak candidate. Lastly, *peak intervals*, which delimit the region belonging to a peak, are defined by the voltage zero-crossings closest to a peak. If peak intervals would overlap, the location of the minimum value between the affected peaks is chosen as a border instead.

To account for signal topologies with more than one maximum and artificial maxima induced by noise, peaks neighboring each other are merged if either of two different sets of criteria are satisfied. This occurs as follows, with peaks being processed in the order in which they occur in the waveform:

1. Start with a peak and the peak neighboring it with the largest maximum.
2. Check for the first set of criteria:
    - Is the minimum distance between the peaks' interval boundaries 15 samples or smaller?
    - Does the neighboring peak have the largest maximum of the two?
    - Is either the peak maximum smaller than 25 % of the neighboring peak's maximum, or are both maxima smaller than 2 % of the recording digitizer's dynamic range?
3. If not all criteria of the first set are met, check for those in the second set:
    - Are the peak interval boundaries overlapping (minimum distance of 0 samples)?
    - Is the absolute difference between the peak's maximum and the voltage value at the point where the boundaries touch smaller than 20 % of the peak's maximum?
4. If all criteria of either set are fulfilled, merge the two peaks. If no merger occurs, repeat the above procedure with the other neighboring peak, should one exist.

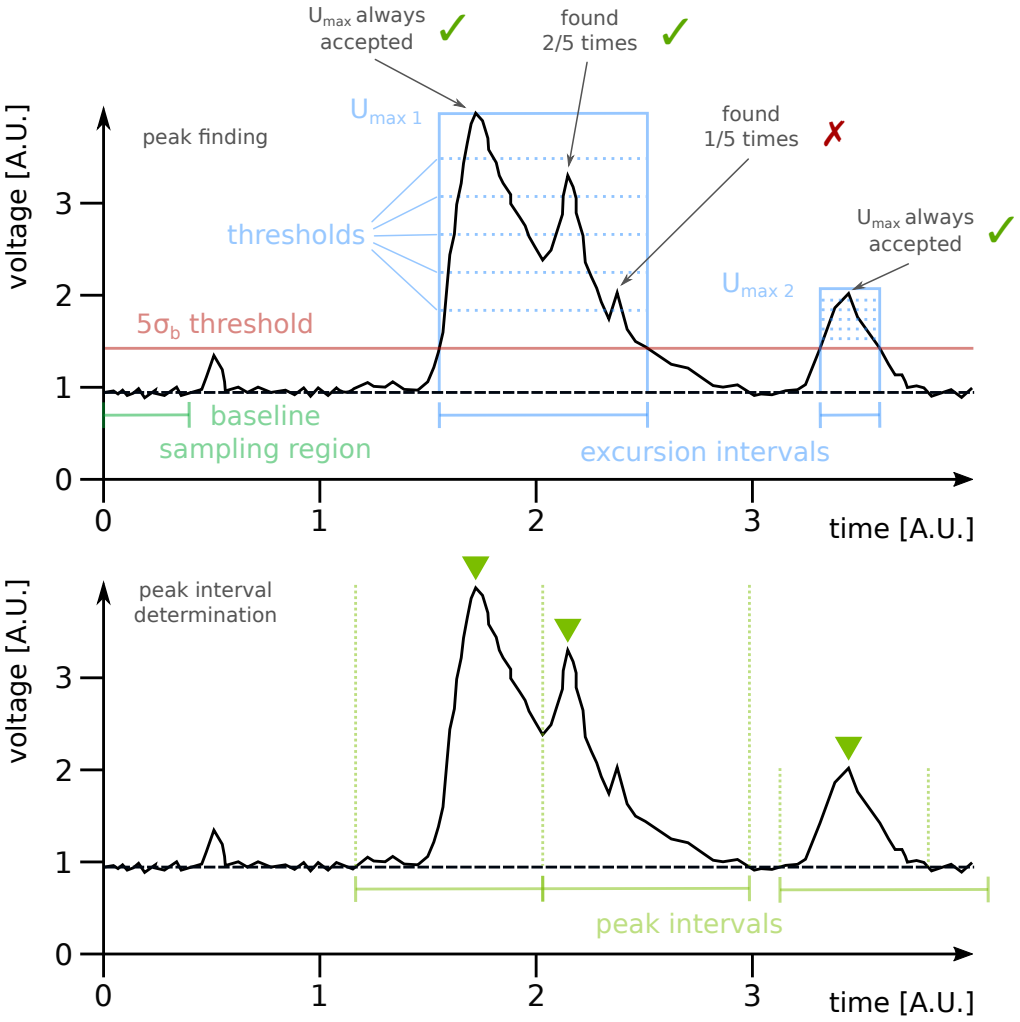

Figure 4.6: Diagrams illustrating the peak finding process on a synthetic waveform. The horizontal, dashed line indicates the baseline voltage. Top: Peak finding algorithm step. For the sake of readability, 5 instead of 19 thresholds are utilized here. Bottom: Result after peak finding and interval determination.

Merging occurs recursively until the number of peaks does not change. If two peaks are merged, the resulting merged peak can only be combined with peaks occurring after it. This restriction is lifted as soon as the next iteration happens. Two use cases for the clustering algorithm explained above can be found in Fig. 4.7. One of them (top) is the correct reconstruction of *single electron S2 signals*, which are created by the proportional scintillation signal of a single electron extracted into the amplification region of the TPC. The amount of photons is small enough that many of them can be resolved in time. The other case (bottom) is a peak which would be split if no clustering were to occur.

As soon as peaks and their intervals are determined, a set of peak parameters is calculated. Among the most important is the peak area, which is calculated by integrating over the peak interval using the composite Simpson's rule. This rule requires an odd number of discrete samples. In case the number of samples is even, Simpson's rule[1] is applied between the first and the next-to-last sample, with the integral between the next-to-last and the last sample being calculated using the trapezoidal rule instead. After the area is estimated, it is converted to PE using conversion factors which take the single PE amplification of the PMT to which the recorded waveform belongs into account. For the sum waveform, integrals are calculated and converted separately for each constituent waveform and summed up at the end. Also, a *coincidence level* is calculated in addition, defined as the number of channels which contribute at least 0.33 PE to the integral.

Besides the peak area, estimating a peak's rising and falling edge is essential for defining its position in time and deriving shape-related parameters. The rising/falling edge is defined as the point where the voltage in the rising/falling flank of the peak corresponds to a fraction κ of the peak maximum. The peak maximum is also referred to as the *peak height* in the following. The edges are determined by starting at the position of the peak maximum and scanning waveform samples in the direction of the corresponding flank. When the first sample is encountered which is below κ times the peak height, the waveform between that sample and the previously scanned sample is linearly interpolated to estimate the point in time where the fraction is reached. The default value used for κ for dual-phase measurements is 0.1. Section 6.3.2 contains a study concerned with choosing an optimum value with regard to variance and robustness against potential waveform sample biases.

[1] See, for example, [74], page 163, for the definition of this rule and the book in general for other numerical integration formulas.

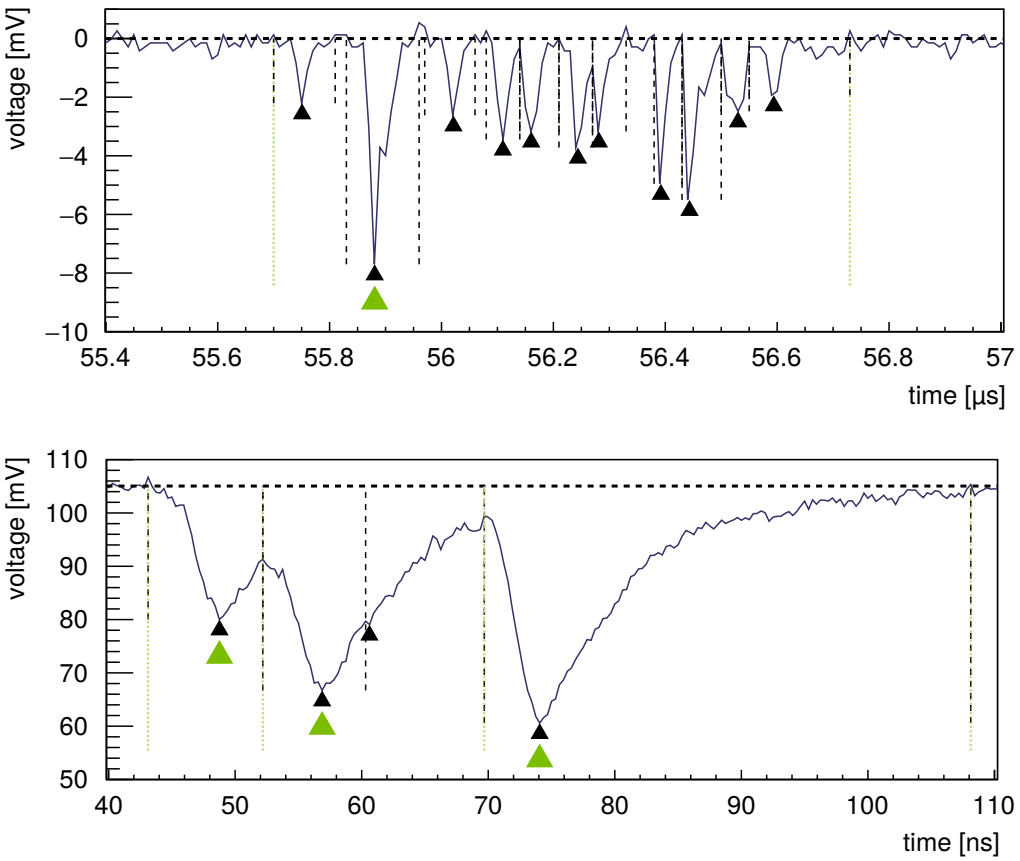

Figure 4.7: Illustration of peak clustering on real data. The dotted vertical lines and the larger triangles, both green, indicate peak interval and extreme value, respectively, as found by the processor with clustering fully enabled. Dashed vertical lines and the smaller triangles in black represent peaks found by the processor with certain clustering criteria removed. Horizontal dashed lines indicate the baseline value estimate for the event. Top: Single electron S2 candidate, recorded in dual-phase operation with V1724 digitizer. The single photon signals it is made out of can be clearly identified. Removing the first set of clustering requirements results in the S2 being split into its constituents. Bottom: Group of single photon signals, recorded in single-phase operation with V1743 digitizer. Removing the second set of requirements causes the central signal to be split because of a voltage fluctuation.

Other peak quantities of interest are area quantiles. An area quantile is defined as the point, between which and the starting point of the peak a certain fraction of the area is contained. They are estimated analogously to rising and falling edges, with one of two main differences being that the scan starts at the beginning of a peak's interval. The other difference is that the area integrated over is the parameter used in the linear interpolation instead of the raw data.

Finally, in dual-phase data, the signal type of a peak needs to be determined. Quantities derived from area quantiles are employed for this task. They are the *rise time*, defined as the distance between the 0.5 and the 0.1 area quantiles, and the *80p width*, defined as the distance between the 0.9 and the 0.1 area quantiles. If both are below given thresholds, the corresponding peak is classified as an S1, otherwise as an S2 signal. Values chosen are 200 ns and 500 ns for the rise time and 80p width, respectively.

Both the clustering and the classification parameters have been validated to result in peaks as they would have been identified by four different analysts, including the author of this thesis, via a waveform examination campaign which involved $\mathcal{O}(100)$ dual-phase events. The same has been done by the author of this thesis with single-phase data recorded with the V1743 digitizer, as used in Chapter 6. During waveform examination, it has been found, that the peak finder and clustering parameters need to be adjusted in order to perform reasonably well, which is due to the higher sampling rate compared to the V1724. A σ_b threshold of 15 is used, which is necessitated by

An example for the performance of walpurgisnacht can be observed in Fig. 4.8, which shows an event recorded during a $^{83\mathrm{m}}$Kr measurement run which includes a multitude of different signals. Almost all signals are correctly identified as either S1 or S2 and have their intervals correctly identified.

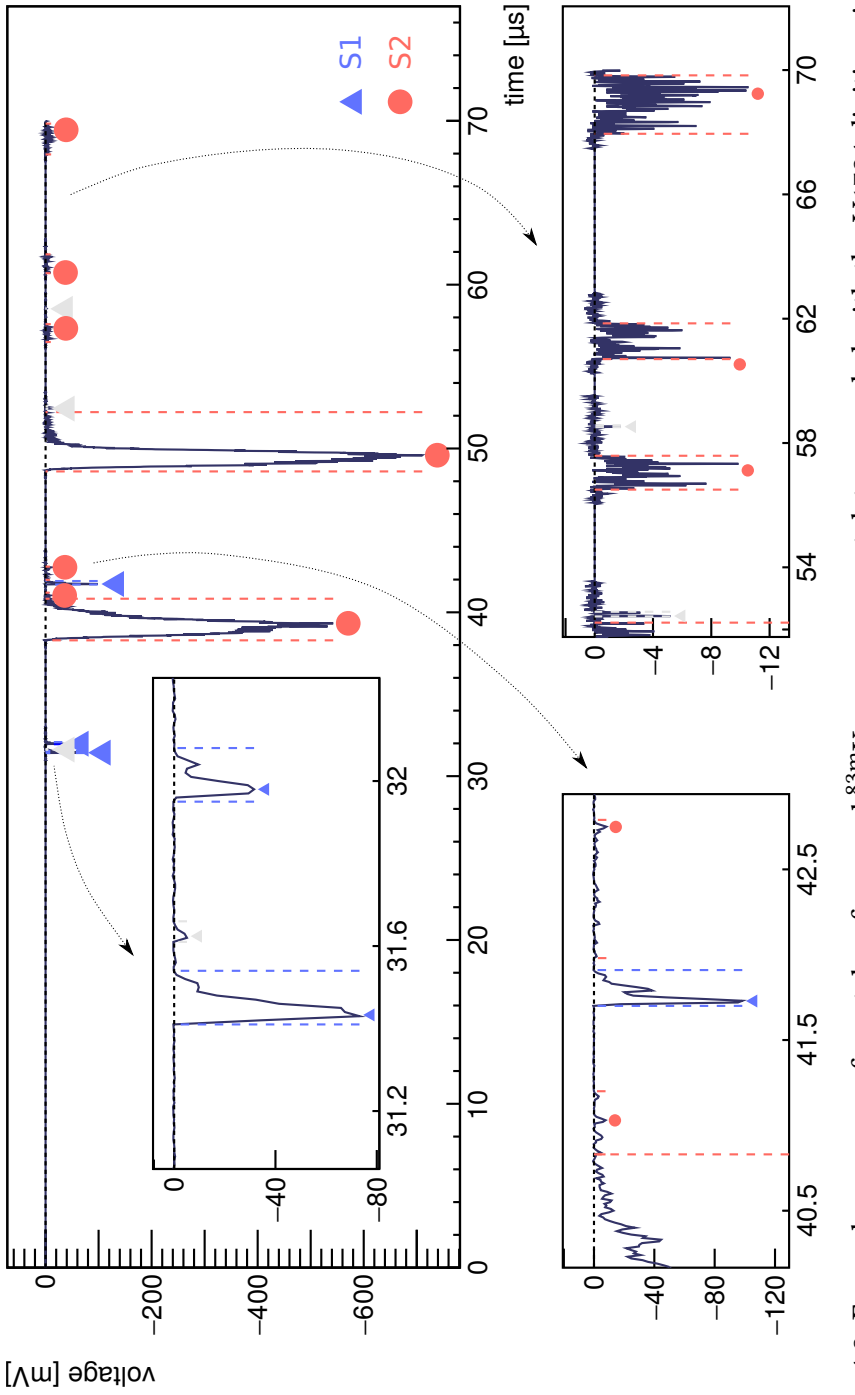

Figure 4.8: Example sum waveform taken from real ^{83m}Kr measurement data, recorded with the V1724 digitizer, including zoomed-in insets. It shows three S1 and two large S2 signals resulting from physical interactions. Single electron S2 signals can be seen occurring after the large S2s. Peaks with a coincidence level < 2 have their indicators shaded in bright grey. Waveform gaps in between the signals result from ZLE.

5 Photosensor calibration and raw data corrections

This chapter describes data calibration and correction methods needed to conduct the pulse shape measurements and analyses presented in Chapter 6. First, it is necessary to calibrate the HeXe TPC PMTs to be able to estimate the amount of light seen and to select on that amount. The procedure used for calibration is outlined in Section 5.1. Furthermore, it has been found, that raw data corrections are necessary due to artefacts and noise influencing the recorded signals. One issue is, that the manufacturer-provided calibration of the utilized V1743 digitizer is insufficient to correct for artefacts related to the way the signal is being sampled. Another issue is caused by both top and bottom PMT signals influencing each other via crosstalk. Corrections developed for handling both the digitizer artefacts and the crosstalk are detailed in Section 5.2.

5.1 Photosensor calibration

To determine the response of each HeXe PMT to a single photoelectron, *in situ* calibrations following the method described in [75] are conducted periodically during operation using the V1724 digitizer. Additional measurements have been made while employing the same channels of the custom-made amplifier as those used for a pulse shape measurement. This is done in order to convert results from a calibration made with the dual-phase measurement amplifier channels to values which a calibration that uses the pulse shape measurement amplifier channels would yield.

During calibration, the PMTs are illuminated via an LED with a peak emission wavelength of 350 nm. The LED is mounted on a custom-made board which allows to trigger the emission of light with a TTL signal. After such a signal is received, an on-board capacitor is discharged over the LED for a fixed duration

($\mathcal{O}(10\,\mathrm{ns})$ or larger) which can be set via a potentiometer. As a consequence, the potentiometer allows to either increase the amount of light emitted per trigger, increasing the variance of the LED photon arrival time in the process, or vice-versa. Emitted LED light is guided towards the TPC via an optical fiber connecting the custom-made board to one of the fiber feedthroughs on the support structure. Inside the cryostat, the light passes through another fiber which ends at the exchangable PTFE cylinder. Going through the cylinder, the light is diffused before potentially hitting a PMT. For every measurement with LED illumination, another one is made using the same PMT operating voltage settings, but without LED illumination. This is done to measure the background charge spectrum. The measurement types are called *LED+BG* respectively *BG* in the following.

Before recording any data, both anode and gate grid inside the TPC are set to ground potential if operating in dual-phase mode. Otherwise, S2 signals could overlap with LED signals at a non-negligible frequency. For LED+BG, a Tektronix AFG3252 arbitrary waveform generator is used to send synchronized trigger signals simultaneously to both the custom-made board and the recording digitizer at the same rate. In a standard measurement, 10^6 events are taken at a rate of $\sim 7\,\mathrm{kHz}$. The position of the LED signals inside the recorded waveforms is determined by calculating the average of all baseline-subtracted waveforms (Fig. 5.1). Afterwards, a fixed interval is chosen for each waveform such, that the LED-induced signals as seen in the average waveforms are fully contained within. The interval is kept as small as possible because every additional sample which does not contain any signal contributes to statistical uncertainty. Finally, the HeXe data processor is run in a special mode which determines baseline values as in its regular mode and integrates over the area inside the aforementioned intervals, but does not include any additional processing. Taking and processing BG data is done equivalently, using the same integration interval as for the corresponding LED+BG measurement. The only difference is, that no trigger signal is sent to the custom-made board in order to avoid LED illumination.

The method in [75] requires no *a priori* information about the shape of the single PE and background charge spectra, which is in contrast to methods which fit an empirical model [76, 77]. Instead, it requires knowledge of the quantiles and moments of the LED+BG and BG charge distributions. For results to be valid, the following criteria need to be fulfilled:

1. The number of detected PE per LED pulse must follow a Poisson distribution.

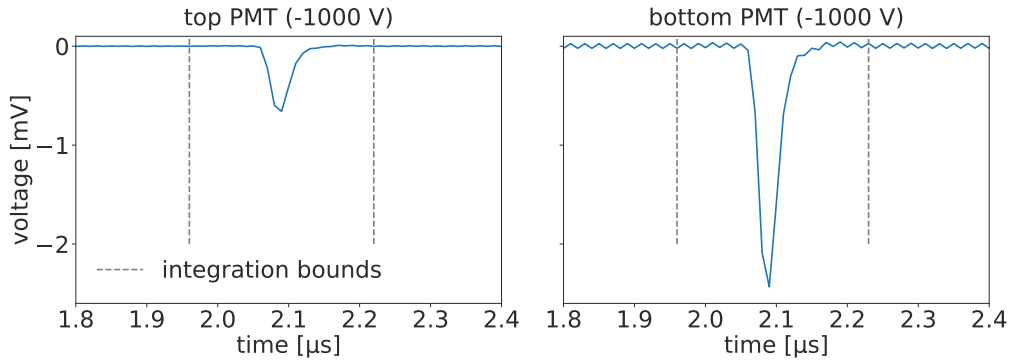

Figure 5.1: PMT signal waveforms averaged over an entire LED+BG measurement which includes waveforms both with and without photon signals. They were recorded using the V1724 digitizer during dual-phase operation. This resulted in the bottom PMT having received more light on average compared to the top PMT because of total internal reflection at the liquid-gas interface. The bounds within which the PMT signals are integrated in each event are also shown. A periodic pattern is visible in the bottom PMT average waveform, which is also present, but smaller, in the top PMT waveform. Because the pattern remains visible when averaging over 10^6 waveforms, the phase of its source must correlate with the trigger signal. The pattern's frequency is about 50 MHz. A potential candidate is the digitizer's internal 50 MHz clock [44], which drives waveform sampling.

2. The PMT response must be proportional to the amount of light received.

3. Electric noise and other factors influencing the background must be kept the same between LED+BG and BG measurements.

The basic principle is to choose a quantile of the BG charge distribution below which the number of events in the LED+BG distribution with at least 1 PE is negligible. The event fraction to which this quantile corresponds to is called f, and the charge equivalent to it is determined using the measured BG spectrum. Afterwards, the number of events in the LED+BG distribution below the charge corresponding to the quantile is counted to estimate the total number of background-only events. Under assumption of Poissonian statistics, the average amount λ of PE detected per LED pulse, also called *occupancy*, can be estimated using [75]:

$$\lambda = -\ln\left(\frac{A_T}{fN}\right), \tag{5.1}$$

with A_T being the number of events in the measured LED+BG charge distribution below the charge which corresponds to f, and N being the total number of events. Finally, the *PMT gain* g, which is the average charge generated per PE in units of e^-, can be calculated using the expected values of each distribution via [75]:

$$g = \frac{E[LED + BG] - E[BG]}{\lambda} \tag{5.2}$$

An example analysis which uses real data can be seen in Fig. 5.2. During the corresponding calibration measurement, the top PMT operated at −1000 V. The figure includes diagnostic plots which are created after every calibration analysis to assess data quality, such as whether the value of λ yielded by the analysis is off or if the background-only peaks of the LED+BG and BG distributions do not match. The former might be the case if a bad value for f has been chosen. This is illustrated using a simple MC simulation which be seen in Fig. 5.3. Background charges are drawn from a Gaussian distribution, while single PE signal charges are sampled from a log-normal distribution instead. The number of PE per simulated event is drawn from a Poisson distribution with an average of $\lambda = 0.5$. At the end, the background and single PE charges are summed up in each event to yield the total simulated charge. Parameters are chosen such, that the resulting spectra qualitatively resemble the real data from Fig. 5.2. The MC data analysis stresses the importance of how well the background-only and signal components of the LED+BG charge spectra are separated and which value of f is chosen.

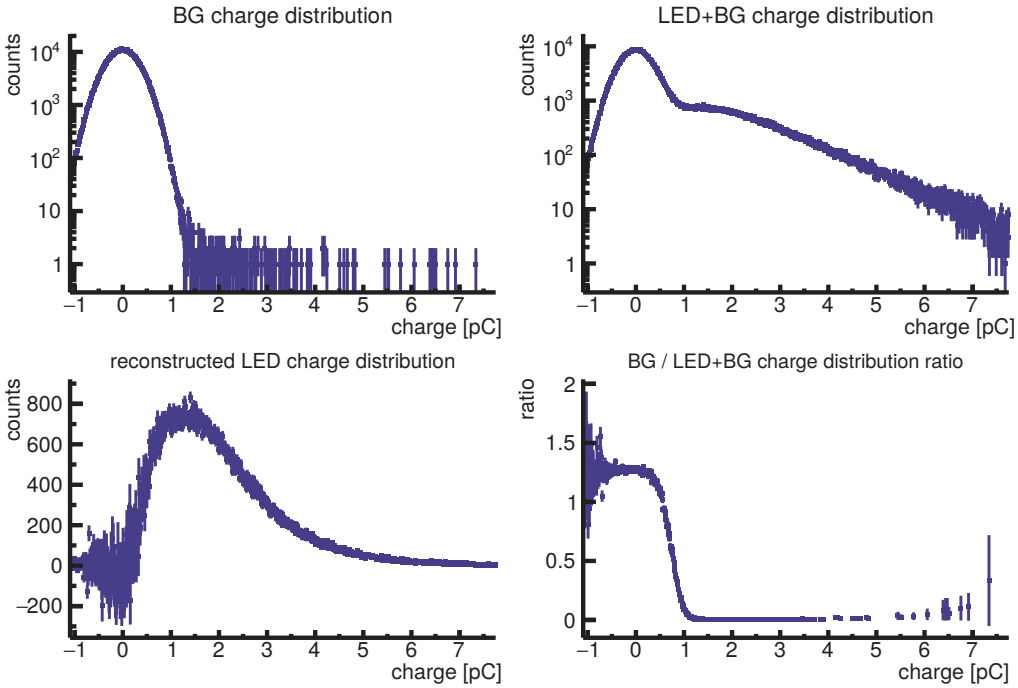

Figure 5.2: Top PMT charge distributions of BG and LED+BG measurements taken during dual-phase operation, centered on the central 99.9 % of the LED+BG distribution. Diagnostic plots show the reconstructed LED-only distribution retrieved by scaling and subtracting the BG distribution from the LED+BG distribution. The scaling factor is equal to the estimated probability of not observing a signal in the LED+BG data ($e^{-\lambda}$). For the corresponding analysis, a value of $f = 0.1$ has been used. In addition, the ratio between the two measured charge histograms indicates, that the shape of the peak containing the background-only events is comparable in both the BG and LED+BG measurements below $\sim 0.25\,\mathrm{pC}$. This is indicated by a flat, non-zero ratio. The effective gain extracted from the data shown here, which includes amplifier amplification, amounts to $g_{\mathrm{eff}} = (11.4 \pm 0.2) \times 10^6$.

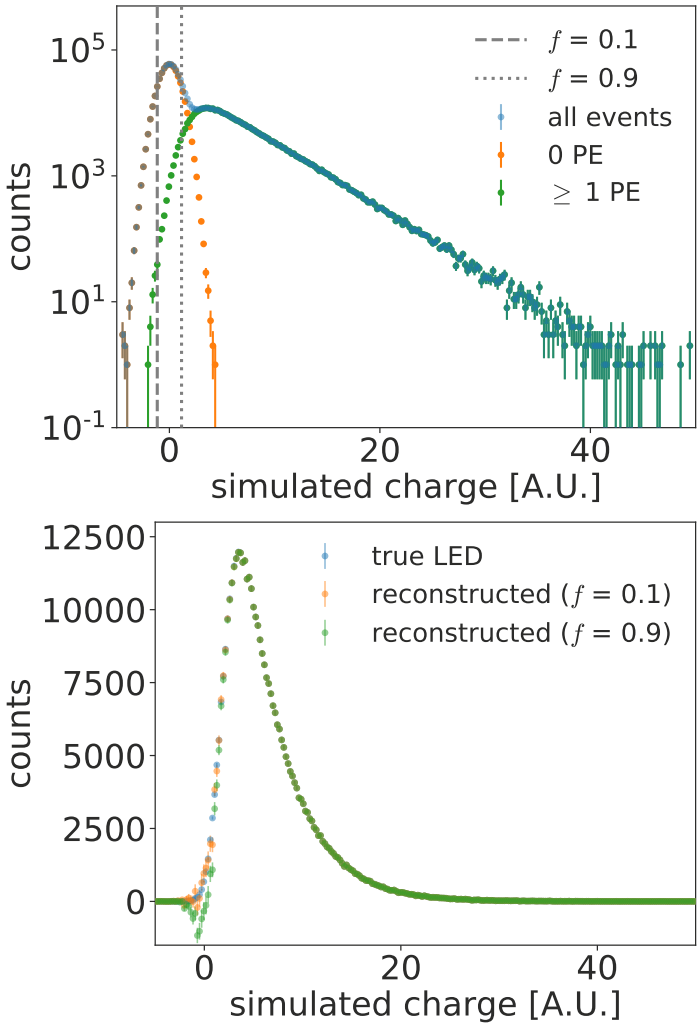

Figure 5.3: Illustration of the importance of background separation and choosing a value for f, using MC data. Top: Simulated LED+BG distribution, divided into its subcomponents. Two lines indicate charges corresponding to different values of f. The line at $f = 0.9$ cuts deep into the population containing at least one photon. This is not the case for the one at $f = 0.1$, below which only few events of that population fall. Bottom: LED charge distributions reconstructed by scaling the simulated BG distribution and subtracting it from the LED+BG distribution as in Fig. 5.2. The distribution reconstructed using $f = 0.1$ exhibits no statistically significant deviation from the true LED distribution. In contrast, the reconstruction with $f = 0.9$ results in an obvious underfluctuation in the left-hand tail due to λ being overestimated.

The best separation is achieved when operating at the largest possible gain of a PMT, reached at the highest absolute operating voltage allowed. As a result, the bias of the occupancy estimate is then also as small as possible. For this reason, two successive calibration measurements are made, if possible. One, called *reference measurement* in the following, is conducted with PMT operating voltages close to their most extreme values allowed. The other one is made with the PMTs operating at different, lower absolute voltages, which generally are the same voltages they operated at during a physics measurement. The occupancy estimate of the reference measurement is then utilized in the analysis of the other measurement to yield a better result.

The importance of choosing an appropriate value for f has already been mentioned. If f is too large, the amount of events assumed to contain no signal is overestimated. According to Eqs. (5.1) and (5.2), this results in λ being underestimated and thus the gain being overestimated. To choose a value for f, a series of multiple, independent calibration measurements was conducted after the chronologically last pulse shape measurement presented in Chapter 6. Both PMTs were operated at a reference voltage of $-980\,\mathrm{V}$ during the end of a dual-phase measurement, at which detector parameters had been stable for several days. In total, 20 LED+BG and BG dataset pairs including 10^5 events each were recorded under identical conditions. To each of them, a value for f is assigned randomly from a predefined set of 20 equidistant values between 0.05 and 0.62 to avoid potential biases caused by the dataset pairs having been recorded successively. The boundaries of 0.05 and 0.62 were chosen based on the fact, that smaller values would yield large statistical errors on the occupancy (> 10 % relative uncertainty), while values above 0.62 are very likely to cut significantly into the spectrum population with at least one PE detected. The resulting occupancy estimates are shown in Fig. 5.4. Based on the scan results and cross-checks with diagnostic plots of preceding LED calibration measurements, the values chosen are 0.1 for the top and 0.05 for the bottom PMT, respectively. While Fig. 5.4 implies that a larger value for f could have been selected for the top PMT, cross-checks using other calibration measurements show, that λ is overestimated in some cases otherwise. This is due to presumably different noise conditions compared to the f scan measurements.

After having finalized the analysis procedure by choosing values for f, calibration data taken during the lifetime of HeXe is analyzed accordingly. The evolution of the resulting PMT gain estimates between April 2019 and February 2020 is be given in Fig. 5.5 to assess its stability over time. The particular time period is chosen because it encompasses two of the three pulse shape measurement runs as outlined in Chapter 6. A measurement of the $^{83\mathrm{m}}$Kr pulse shape,

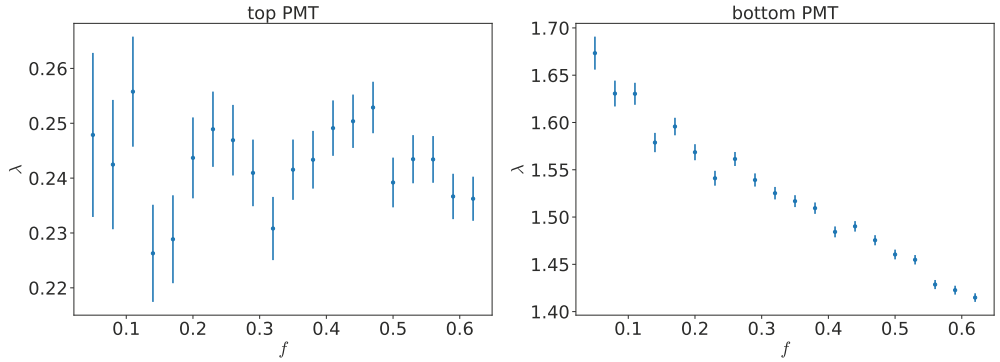

Figure 5.4: Occupancy estimates of a series of measurements to determine a value for f. The plot for the top PMT suggest that a value as high as $f = 0.47$ could be used, as only larger values hint towards a systematic downward trend for the central value of the λ estimate. However, cross-checks with other calibration measurements indicate, that a lower value is required. The bottom PMT, which has a lower gain than the top PMT when both are operating at the same voltage, shows a worsening bias of the estimated occupancy with larger f.

which was made in February 2019, is not covered. Because the aforementioned issues caused by S2 signals were only identified in April 2019, no good quality calibration data taken while running with LXe is available for earlier times. This necessitates using gain estimates measured in April 2019 in this case. As no events occurred in between February 2019 and April 2019 from which one might expect an impact on PMT performance, such as exposure to excessive quantities of light, these estimates are assumed to still be reasonably accurate when applied to past data.

5.2 Raw data corrections

5.2.1 Artefacts related to digitizer sampling

As described in Section 4.5, the CAEN V1743 digitizer uses time interleaving to achieve its effective sampling rate of 3.2 GHz. The principle is illustrated in Fig. 5.6. In the case of the V1743, the input is distributed across 16 separate signal lines which sample at frequency of 200 MHz each. The lines are delayed

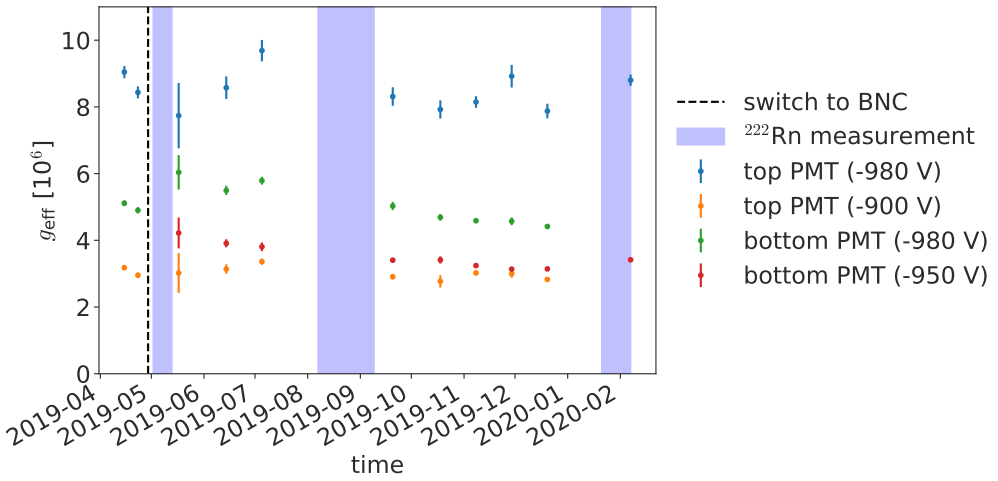

Figure 5.5: Evolution of the effective gain, including amplifier amplification, measured during multiple dual-phase operations over a period in time spanning a part of the LXe purity studies as presented in [66] and the two ^{222}Rn pulse shape measurement runs detailed in Chapter 6 (August 2019 and January 2020). If available, measurements with the PMTs operating at −980 V, are used as reference measurements. At least two systematic shifts are noticeable. One upward shift occurs after switching from a multipin feedthrough for leading PMT signals outside the cryostat to separate BNC feedthroughs for each PMT. The other shift, followed by a downward trend of the bottom PMT gain, occurs after a long series of measurements involving ^{222}Rn. This is assumed to be the result of both PMTs being exposed to large amounts of scintillation light caused by α-decays of ^{222}Rn as well as its daughters ^{218}Po and ^{214}Po. This issue, including a solution to it, is discussed in Section 6.2.

by 312.5 ps relative to each other, resulting in the higher effective sampling rate. According to manufacturer specifications, the delays are calibrated such, that the time integrated nonlinearity (INL)[1] amounts to less than 5 ps. Because this is equivalent to only a small fraction of the 312.5 ps sampling period, the time INL is a negligible source of uncertainty. To sample a waveform, the digitizer continuously records waveform samples in chronological order into a circular analog memory buffer which contains 1024 cells, with the cells denoted by $\{W[n] \mid n \in \{0, 1, \dots, 1023\}\}$ in the following. When a trigger signal arrives, the buffer is frozen and read out. As a consequence, the cell into which the starting sample of the waveform is written varies. The digitizer is set up such, that the index n of the starting sample has to be a multiple of 16. This results in waveforms always starting with a sample from the same signal line, which is important for what follows in the next paragraph.

Each signal line has its own input amplifier and its own baseline offset voltage. If amplifier gain or baseline offset voltages are not matched across all 16 lines, the recorded waveforms exhibit an artificial pattern repeating every 16 samples (equivalent to 5 ns), which, if gains are mismatched, also depends on the input voltage (Fig. 5.7, left). While gain and offset differences are compensated for by factory-side tuning and baseline calibration using the manufacturer-supplied software for the V1743, called WaveCatcher [78], a residual pattern still remains. It can reach, depending on the input voltage and at which DC offset the WaveCatcher baseline calibration is made, an amplitude of $\mathcal{O}(1\,\mathrm{mV_{pp}})$. Because digitization always starts at the same line, the pattern is stable across waveforms, leading to distortions of signals which depend on their location within the waveform. Evidently, this results in *position- and input-dependent biases* for parameters which rely on a signal's shape.

To correct for this residual pattern, dedicated measurements are made to quantify it. One such measurement consists of $\mathcal{O}(10^4)$ or more full-length waveforms recorded for each digitizer channel while their inputs are not connected to any device. They are taken at least 30 minutes after powering on the DAQ electronics to ensure, that the digitizer has reached its long-term operating temperature. Trigger signals are provided by the HeXeR software. The waveforms are then aligned by circular shifting their samples such, that the sample coming from $W[0]$ is placed at the beginning. The information needed to map the samples to the cells which contained them is part of the event's raw data fetched from the digitizer. Afterwards, all aligned waveforms are averaged

[1] The time INL corresponds to the deviation from the difference in time between the beginning of a waveform and one of its samples expected from the sampling rate.

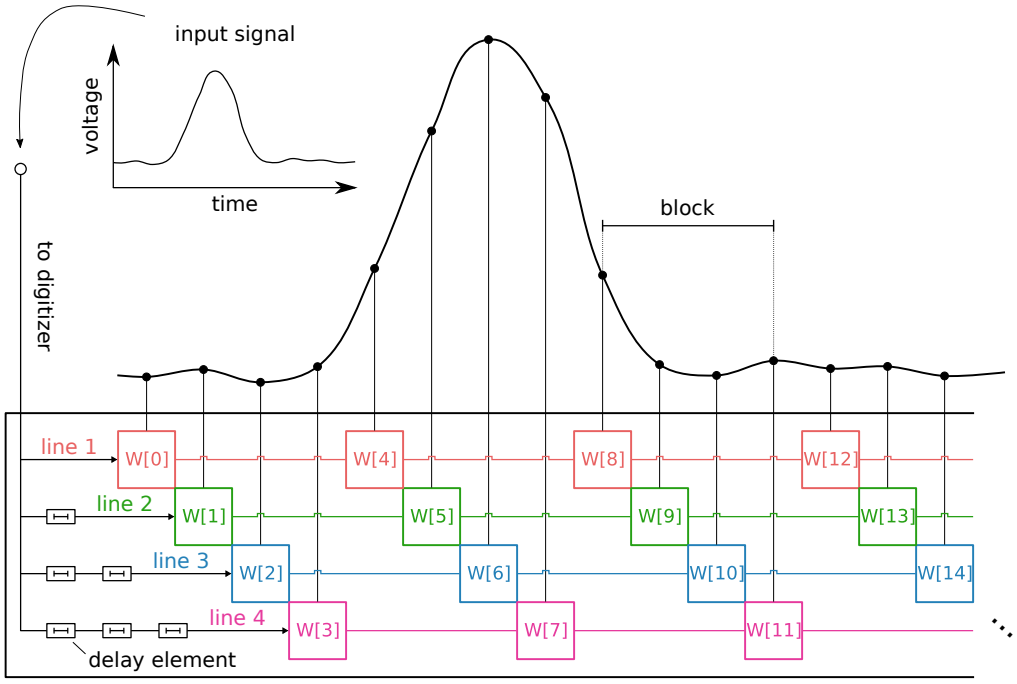

Figure 5.6: Diagram explaining the principle of time interleaving which depicts 4 different lines for the sake of simplicity. The input signal is distributed to n separate lines which sample it with a frequency of ν' each. Line inputs are delayed by multiples of $1/\nu'$ relative to each other. Interleaving the samples as depicted in the diagram yields a waveform with an effective sampling rate of $\nu_{\text{eff}} = n\nu'$.

over, which yields the residual baseline pattern. This is repeated for multiple settings of the digitizer's on-board DACs, which shift the baseline voltage, to cover as much of the 2.5 V dynamic range as possible. Afterwards, the average value of the nth aligned waveform sample for a given DAC setting, $\hat{W}[n]$, is grouped together with the average value of $W[0]$, $\hat{W}[0]$. The $(\hat{W}[n], \hat{W}[0])$ pairs are used to construct cubic splines which yield functions that approximate the value $W[0]$ would have if it sampled the same voltage corresponding to the value of $W[n]$. These functions are called $\hat{f}_n$ in the following. Having calculated all splines, a sample coming from cell $W[n]$ can then be converted to the response of $W[0]$ according to the following formula:

$$W'[n]_{\text{corr}} = \begin{cases} \hat{f}_n(\hat{W}[n]_{\max}) + W[n] - \hat{W}[n]_{\max}, & W[n] > \hat{W}[n]_{\max} \\ \hat{f}_n(\hat{W}[n]_{\min}) + W[n] - \hat{W}[n]_{\min}, & W[n] < \hat{W}[n]_{\min} \\ \hat{f}_n(W[n]), & \text{otherwise} \end{cases} \tag{5.3}$$

Here, $\hat{W}[n]_{\text{min / max}}$ is the minimum respectively maximum value of $\hat{W}[n]$ encountered in the baseline pattern measurements used for building the splines. The definition by cases is necessary to cover edge cases where sample values are outside the domain of the interpolating function. Pattern calibration measurements and spline calculation are repeated each time after a V1743 calibration using the WaveCatcher software, as the latter influences the corrections which are already applied during DAQ.

The effects of applying the correction to real data can be seen in Fig. 5.8, left. Albeit with smaller amplitude, a residual pattern is still visible. This is attributed to differences in ambient temperature between pattern calibration measurements and pulse shape measurement runs, as none of the other possible parameters, such as digitizer settings, changed in between. Observing the pattern closely, one notices, that the pattern's period seems to be rather about 10 ns instead of 5 ns. In the FFT of the averaged waveform (Fig. 5.8, right), however, no distinct peak is visible at 100 MHz. Instead, the peaks at multiples of 200 MHz, the frequency which corresponds to a period of 5 ns, dominate. A possible explanation is related to the fact, that the correction, which is equivalent to a subtraction of the baseline pattern, does not match the actual pattern in data exactly. As a consequence, the resulting waveform can be seen as a sum of two signals with frequency components at multiples of 200 MHz each. The sum of, for example, the 200 MHz component of one signal with the 400 MHz component of the other results in a beat with an envelope frequency of 100 MHz. Thus, 32 samples, equivalent to 10 ns, are needed to fully

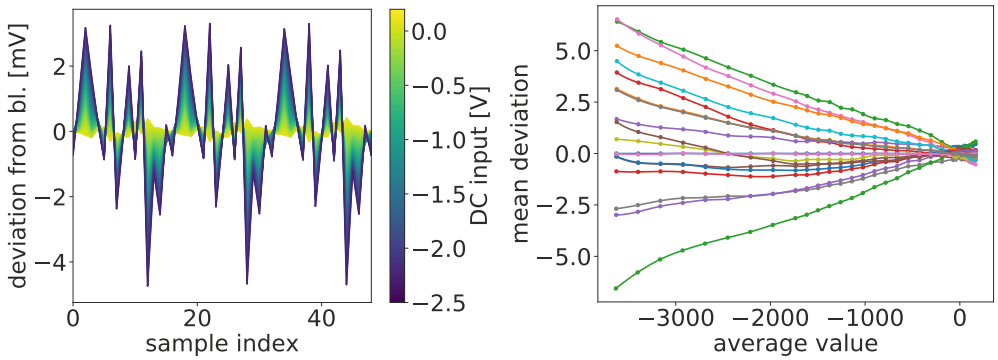

Figure 5.7: Measurements of the baseline pattern. Left: The first 48 samples of 31 averaged waveforms measured for a pattern calibration, aligned to have $W[0]$ at the beginning and with their means subtracted. Sample values between measurements are interpolated. Right: Mean deviation of $\{W[n] \mid n \in 0, 1, \ldots, 16\}$ from $W[0]$ versus their value in the corresponding averaged waveform. The data used is the same as for the plot on the left-hand side. Also shown are the deviations as predicted from the associated cubic splines.

reconstruct the pattern.

In order to approximately correct for the remaining pattern, the average baseline-subtracted waveforms of the first 10^4 events from the first and last datasets of a measurement run are filtered using a 5th order low-pass Bessel filter with a critical frequency of 140 MHz. The filter removes most of a PMT signal, should one be present, while retaining the baseline pattern. Afterwards, the waveform is restricted to sample indices between 576 and 927. The lower bound ensures, that the region of the average waveform which is affected the most by PMT signals is excluded, as the filter does not remove them entirely. The upper bound removes a region which contains bipolar electric noise with an amplitude of about 2.5 mV that correlates with the trigger signal and appears in every waveform at the same position and similar intensity (Fig. 5.9). This is a problem known to the designers of the digitizer [79], which implies that it is present in at least a significant fraction of the entire digitizer series. It does not affect raw data in any other fashion, but it also has to be taken into account for analyses. Afterwards, the interval within the bounds is evenly divided into 11 intervals with 32 samples each (11 times two blocks as defined in Fig. 5.6). The average of all intervals is then taken and denoted as $\{B[n]_{\text{start/end}} \mid n \in 0, 1, \ldots, 31\}$ in the following for the first and last dataset of

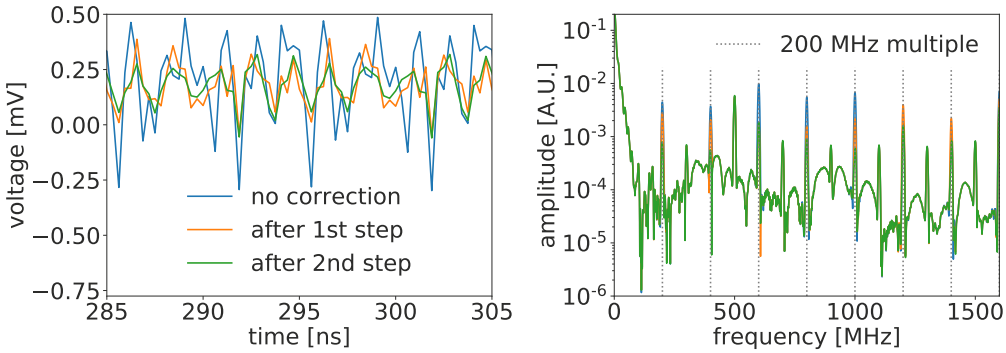

Figure 5.8: Application of the residual pattern correction. Left: Excerpt of the average waveform of a real data set, processed at different levels of correction. Right: Fourier spectrum of the waveforms shown on the left-hand side, made according to the same procedure as presented in Section 3.1. It shows how each correction step reduces the amplitude of the peaks at multiples of 200 MHz.

the measurement run, respectively. The final correction step is then:

$$W[n]_{\text{corr}} = W'[n]_{\text{corr}} - \frac{(B[n \bmod 32]_{\text{start}} + B[n \bmod 32]_{\text{end}})}{2} \tag{5.4}$$

As it can be seen in Fig. 5.8, this second, final correction step improves upon the initial spline-based correction step. Because the subtracted pattern is fixed, it is not able to fully changes in line amplifier gains, however, so some effects of the pattern are expected to remain.

5.2.2 Photosensor signal crosstalk

It has been found during the pulse shape measurements presented herein, that the PMT signal lines influence each other either within the cryostat or at the signal cable feedthrough, producing *crosstalk*. Neither an upgrade of the signal feedthrough from multipin to BNC, nor a switch to coaxial PMT HV cables for the portion within the cryostat eliminated it. An example waveform containing crosstalk is shown in Fig. 5.10. Signals in the bottom PMT consist of $\mathcal{O}(100\,\text{PE})$, which is large enough to induce a non-negligible bump in the top PMT waveform. The position of that bump coincides with the rising flank of the bottom PMT signal, while its height amounts to $\mathcal{O}(1\,\%)$ of a top PMT single PE signal. Depending on which rising flank definition is used as a signal time

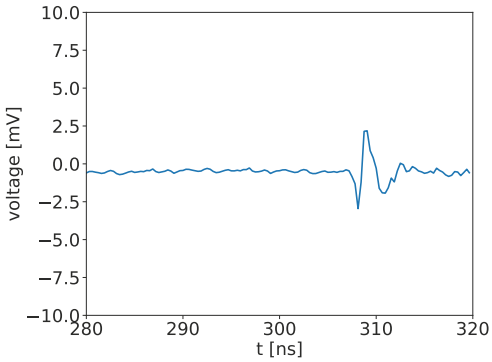

Figure 5.9: Average bottom PMT waveform using 10^4 events from a pulse shape measurement dataset after baseline correction as an example. It shows bipolar noise which occurs at the end of every waveform in both digitizer channels used for recording.

parameter, this is sufficient to induce a large, position-dependent bias when determining a signal's position, as it can be seen in. It is strongest around the beginning of the bottom PMT signal, which is equivalent to the starting point of the photon arrival time distribution. This makes it difficult to correctly estimate pulse shape parameters which are constrained mostly by that region, such as the effective singlet lifetime τ_s and the singlet fraction f_s.

To correct for crosstalk, measurements were made at the end of each ^{222}Rn run where the top PMT had been switched off. DAQ and detector conditions were identical to the preceding run. This yielded a sample of waveforms purely containing crosstalk signals, which is used to fit a function of the form:

$$S[n]_{\text{synth}} = \sum_{k=-m}^{m} a_k S[n+k]_{\text{bot}}, \tag{5.5}$$

with $S[n]_{\text{bot}}$ being the nth sample of the recorded bottom PMT waveform and m being the width. For the latter, a value of $m = 24$ is used.

The purpose of Eq. (5.5) is to predict the crosstalk seen in the top PMT using the waveform of the bottom PMT, allowing to remove it. The filter coefficients are found by minimizing:

$$\chi^2(a_{-m}, a_{-m+1}, \dots, a_m) = \sum_{k=1}^{N_{\text{wfm}}} \sum_{n=1}^{N} \left(S[n]_{\text{synth, k}} - S[n]_{\text{top, k}} \right)^2 \tag{5.6}$$

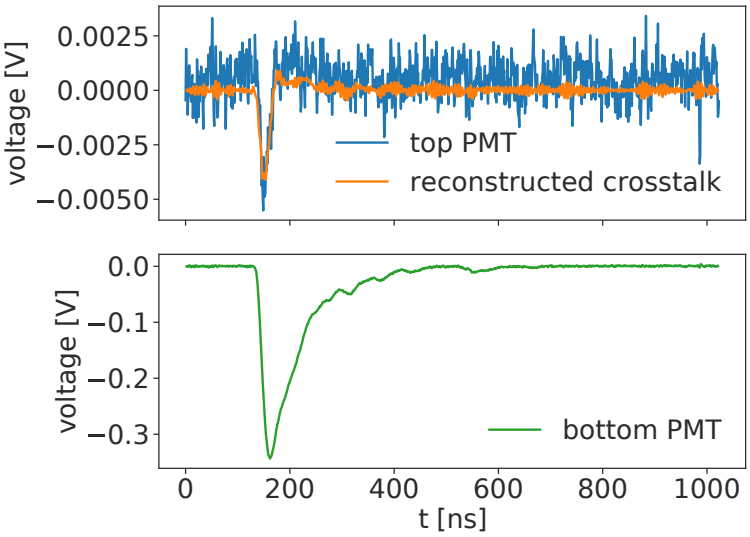

Figure 5.10: Recorded event of a pulse shape measurement with visible crosstalk, induced by the bottom PMT signal. Also shown is the crosstalk as predicted by the fitted correction function introduced in this section.

Here, N is the number of samples per waveform, and N_{wfm} is the number of employed crosstalk sample waveforms, which amounts to 10^4. It has been found, that a further subtraction of the residual baseline pattern is necessary for the fit to converge to values which correctly predict crosstalk. Otherwise, it also tries to "predict" the periodic baseline pattern. To approximately achieve this subtraction, the pattern consisting of the first 16 samples of a waveform is subtracted accordingly for each event separately.

The influence of applying all corrections can be observed in Fig. 5.11. For each plot therein, a different value of the height fraction κ is used for the rising edge to demonstrate the sensitivity of this parameter to the artefacts presented in this section (see Section 4.6 for the rising edge definition). In both plots, the baseline correction smoothens out the Δt distribution. While a small κ for the bottom PMT is beneficial to pulse shape spectrum resolution, as evidenced by the steeper left-hand flank of Fig. 5.11, top, a dip caused by the crosstalk is visible at $\sim 5\,\mathrm{ns}$. While the issue is alleviated by the crosstalk correction, the rising edge is still very sensitive to baseline artefacts, which is also a reason for why $\kappa = 0.05$ is not used for the bottom PMT in further analysis. The bottom plot, which uses the values of κ that are determined in Section 6.3.2, does not show such an extreme dependence while still benefitting from the crosstalk

correction.

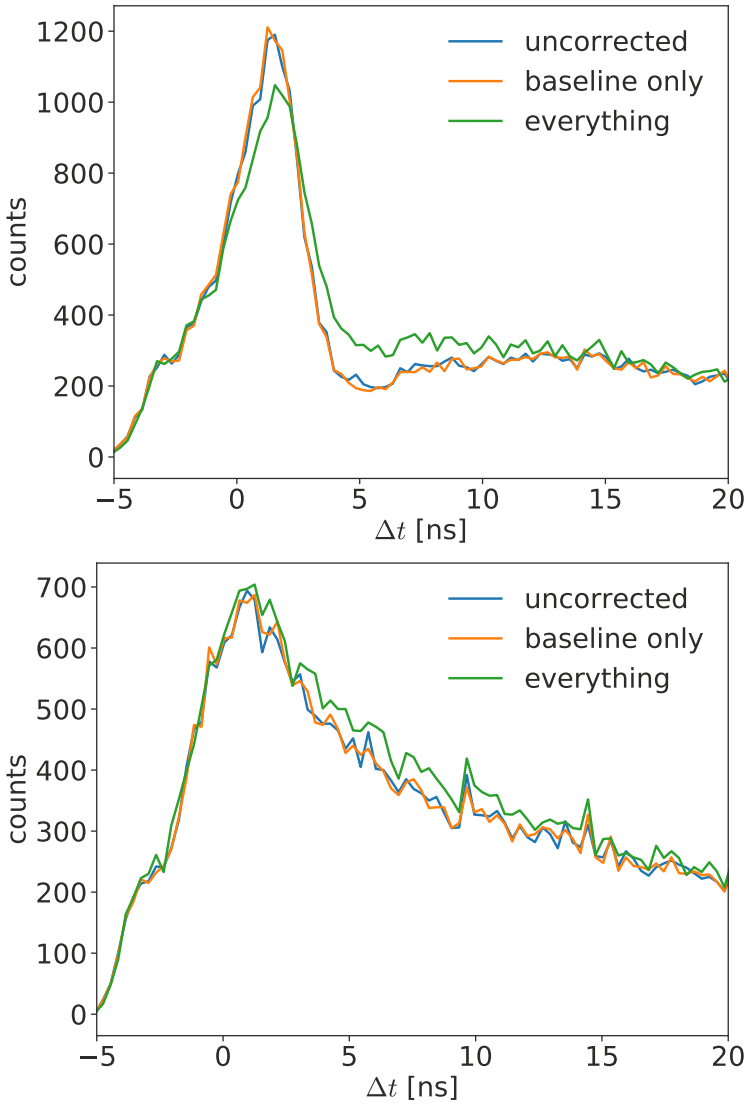

Figure 5.11: Influence of both baseline and crosstalk corrections on pulse shape spectra on ^{222}Rn data. Δt is the difference, between the rising edges of the largest top PMT peak and the largest bottom PMT peak, with event selection criteria applied as according to Section 6.3.1. Each plot uses different values for the rising edge height fraction κ. Top $\kappa = 0.05$ for both PMTs. Bottom: $\kappa = 0.55$ for top and $\kappa = 0.3$ for bottom PMT.

6 Liquid xenon pulse shape measurements

The penultimate chapter deals with measuring and analyzing the LXe scintillation pulse shape for interactions resulting from decays of ^{83m}Kr as well as ^{222}Rn and its daughters, both in single-phase operation. Because the pulse shape is known to depend on the strength of the local electric field, Section 6.1 deals with estimating the field within the HeXe TPC depending on voltages applied to the PMTs and grids. In addition, an optical MC simulation of the TPC is developed and utilized to determine the probability of a photon to have originated from a certain location, as no reliable position reconstruction is possible in HeXe single-phase operation. Combined with the field calculation, this yields a more accurate estimate of which field strength contributes how much to the measured pulse shape.

The field estimates are then utilized in Section 6.2, where the data taking procedure is outlined to be able to set a specific electric field configuration. Finally, Section 6.3 describes the actual pulse shape analysis including data selection, definition of signal time parameters, and the fitting procedure for parameter extraction. It is followed by a discussion of the results in Section 6.4.

6.1 Estimation of the electric field

6.1.1 Electrostatic field simulation and optimization

The electrostatic field simulation and calculation described in this subsection has been carried out by a colleague [71] whom the author is thankful for.

To calculate the electric field inside the HeXe TPC, finite element analysis (FEA) is performed on a model of the TPC which includes the entire PTFE filler, HV cables and the grounded cryostat, using COMSOL Multiphysics [80]. For each grid, field-shaping ring and PMT, the electric field generated when

applying 1 V to each of them is calculated first. These fields are called *support fields* in the following. Afterwards, the superposition principle is utilized to calculate the field for a certain HV configuration by adding and scaling the support fields accordingly. The deviation from a direct finite element calculation is confirmed to be at the order of the numerical FEA precision.

Each support field is voxelized into a $100 \times 100 \times 100$ 3D histogram which encompasses the TPC volume, with the field assigned to each voxel corresponding to the average field vector within it. The field is sampled equidistantly in R^2, ϕ, and Z, with R being the distance from the central axis of the TPC, ϕ being the angle around that axis, and Z being the height along the axis relative to a point of reference. A script is then used to minimize the deviation of the field strength from a targeted value:

$$\chi^2(\vec{U}) = \sum_{i=1}^{N_{\text{bin}}} \left(|\vec{E}(\vec{x}_i, \vec{U})| - |\vec{E_{\text{target}}}| \right)^2, \tag{6.1}$$

with the sum being over voxels which belong to the drift volume only. This is because other TPC regions cannot be optimized at the same time due to how grids and PMTs are arranged. $\vec{U}$ includes the three mesh voltages, while PMT voltages are kept fixed to the values used for the corresponding measurement.

6.1.2 Photosensor light collection Monte Carlo

The probability of a photon to hit either of the PMTs is estimated via a MC simulation utilizing the GEANT4 framework [81]. First, the inner TPC volume, including meshes and PMT windows, is constructed in the simulation based on design drawings of both TPC and meshes. For reasons explained in Section 6.2, the geometry also includes PTFE disks in front of each PMT which are used to reduce the amount of light seen by them. Different disk thicknesses are used depending on which pulse shape measurement the light collection is estimated for.

The hexagonal tiling of each HV grid is fully modelled, with the relative rotation of the meshes to each other being taken into account. Having defined the geometry, it is validated by simulating *geantinos*, which are fictional particles provided by GEANT4 for debugging purposes. They do not undergo any physics process. Instead, they propagate in a straight line until they hit the

boundary of the detector model. For checking the geometry, geantinos are produced homogeneously distributed within the drift volume with an isotropically distributed direction of movement. The point of origin of a geantino track and the points along it where the simulation detects a boundary between two different volumes are recorded. Afterwards, the design drawing of the TPC is overlaid with the boundary coordinates extracted from the simulation to finally validate the geometry. The final geometry for a certain PTFE disk configuration can be seen in Fig. 6.1. The plots were generated by homogeneously distributing 10^6 geantinos within each subvolume of the geometry and recording their starting position, which is then drawn into a scatter plot.

Because only photons are relevant for light collection, simulated physics processes are constrained to a subsection of those specified in the *G4OpticalPhysics* physics list. The subsection consists of Rayleigh scattering, photon absorption, and boundary interactions such as refraction and reflection. Material properties on which the simulated processes depend, such as absorption lengths and refractive indices for given wavelengths, are taken from [82] if not mentioned otherwise. They are assigned to the corresponding detector geometry components. Absorption within the PTFE disks is switched off, with the attenuation being modelled by diffuse reflection only. While this affects the fraction of a scintillation signal seen by the top PMT compared to the bottom PMT, the relative probability for a photon to have originated from a certain part of the volume given that it has been seen by the top PMT should not be affected.

In the final step, *optical photons* with an energy of 7 eV and random polarization are generated homogeneously distributed within the entire xenon volume. They are GEANT4's representation of scintillation photons and the only particles in the simulation affected by the selected subsection of physics processes. After sampling the starting point, 10^3 optical photons are propagated from it, with each photon's movement direction being sampled from an isotropic distribution. As soon as an optical photon is either absorbed or hits one of the PMT windows, it is not propagated any further. Afterwards, it is counted how often a photon reached the top respectively the bottom PMT. The counts as well as the coordinates of the point of origin are stored in a ROOT TTree. In total, about 3×10^9 events with 10^3 photons each are simulated for every disk configuration.

An example light collection result which uses the geometry from Fig. 6.1 is shown in Fig. 6.2. There, the influence of the HV grids in terms of light collection can clearly be made out. The discontinuous jumps at the grid positions are

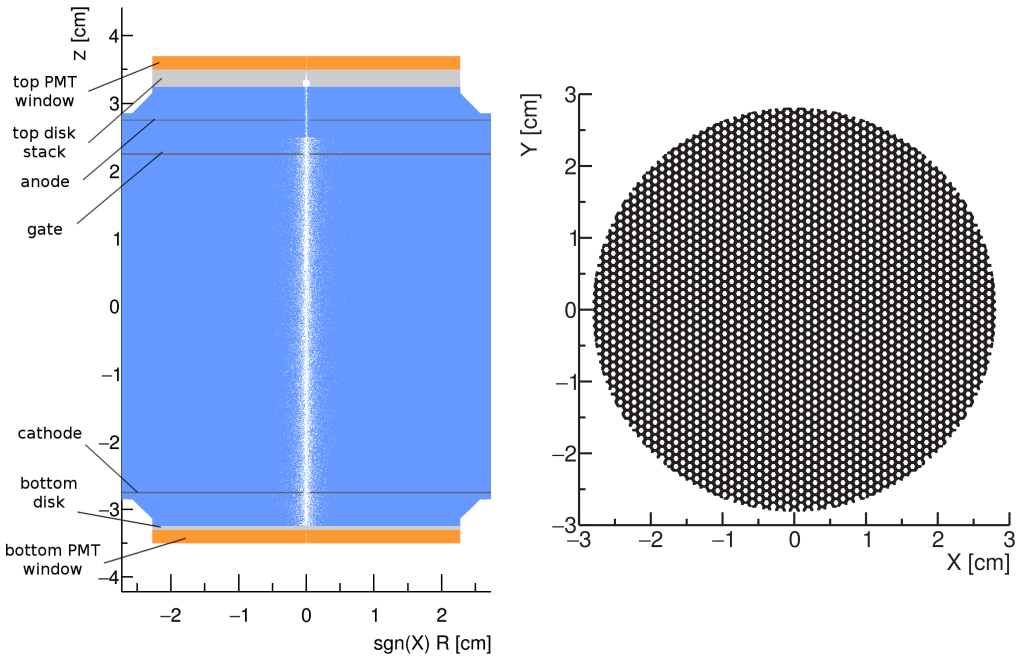

Figure 6.1: Geometry of the optical HeXe MC. Left: Height Z versus distance from the central axis R. The latter is multiplied with the sign of the X coordinate to mirror the picture in R, providing a better view of details in the center. The holes with different diameters visible in the top PTFE disk stack, which consists of two disks, are actual geometry features (see Section 6.2). Otherwise, the missing events in the central part are caused by the R^2-dependence of the size of a volume element. The sudden change in sample number between gate and anode is due to a change in subvolumes at this point. The xenon inside the TPC is represented by two separate subvolumes in order to also be able to simulate dual-phase operation. For the work presented here, LXe is assigned to both as a material. Right: Anode grid as implemented in the MC. Gate and cathode look identical, but are rotated in the XY-plane by $\pm 45°$ relative to the anode.

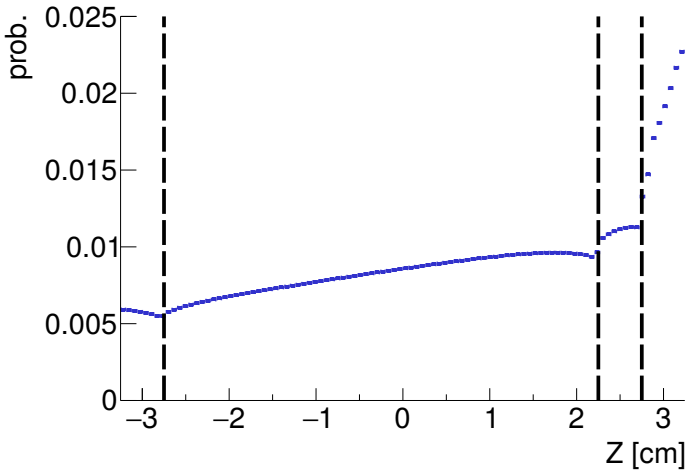

Figure 6.2: Simulated probability of a photon to be detected by the top PMT when originating from a height Z. Dashed lines indicate the grid positions.

the result of photons being blocked respectively reflected by the girds themselves.

6.1.3 Weighted field strength estimate

Results from the electric field calculation and the photon PMT hit probability simulation are combined by transforming the coordinates of the sampled points of the FEA model into the coordinate system of the optical MC. Afterwards, the origin point coordinates are histogrammed in R^2, ϕ and Z, with the binning being identical to the one used for the support fields. This ensures that volume elements are of equal size. Together with the number of optical photons per event, this gives the total number of photons which originated from a certain bin of the detector volume in the simulation. For bin i, this number is called $N_{\gamma,i}$. Also, the number of photons which reached the top PMT is added up for each bin for the points of origin that fall within it, yielding $N_{\text{top},i}$. Using both numbers and defining $p_i := N_{\text{top},i}/N_{\gamma,i}$, the fraction of photons detected in the top PMT which originated from bin i is given by:

$$w_i = \frac{p_i}{\sum_{j=1}^{N_{\text{bin}}} p_j}, \tag{6.2}$$

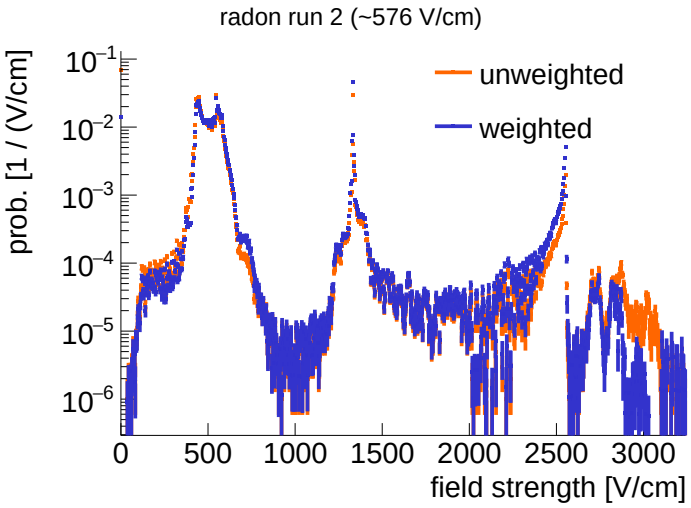

Figure 6.3: Weighted and unweighted field distributions, calculated for a field configuration of the second radon run as defined in Section 6.2. Three distinct peaks are visible, which, from left to right, correspond to the drift region, the region between bottom PMT and cathode, and the region between top PMT and anode. As expected from the light collection variation as seen in Fig. 6.2, the region between top PMT and anode is weighted stronger compared to the unweighted distribution, while the other regions changed less. The estimated values for this configuration are $\hat{E} = 576\,\mathrm{V/cm}$ and $\delta_{\hat{E}} = 113\,\mathrm{V/cm}$.

when assuming photon sources to be homogeneously distributed in the entire volume.

Because the binning of the w_i is identical to the one of the electric field map, they can be used to calculate a weighted median, $\hat{E}$, over the latter. $\hat{E}$ is used as the central estimate for the electric field strength for each HV configuration. To give a measure for the variation of the field strength, the weighted interquartile range (IQR), $\delta_{\hat{E}}$, is determined. It gives the central 50 % probability interval for the electric field of the point from which a photon, given that it is detected by the top PMT, originated. An example field distribution is displayed in Fig. 6.3. It is evident, that TPC regions outside the drift volume are responsible for sizable systematic uncertainties ($\delta_{\hat{E}}/\hat{E} > 0.1$ and larger), which cannot be avoided in single-phase operation.

6.2 Procedure for measuring the pulse shape

The pulse shape is estimated for ^{83m}Kr and ^{222}Rn (daughter) decays using single photon sampling (which has been used, for example, in [18, 22, 83–86]). This is done by attenuating the prompt LXe scintillation light reaching the top PMT such, that, if possible, only a single photon is detected on average, if one is detected at all. In contrast, the bottom PMT collects as many photons as possible to allow to estimate the start time of the prompt scintillation signal. As the arrival time of a photon relative to scintillation start is independent of its probability to be detected, single photon sampling allows, in principle, to measure the arrival time distribution with only few systematic effects to worry about. This is an advantage compared to other LXe pulse shape studies which either fit a signal model function directly to recorded pulses [87] or employ complex MC detector simulations and match them to data [21, 60, 88, 89]. The former method needs to take modification of the signal shape by the electronic components used for recording waveforms, such as those induced by a finite signal bandwidth, into account for an unbiased result. The latter method implies a multitude of potential sources for systematic deviations, with each of them needing to be identified and quantified.

For this work, one ^{83m}Kr and two ^{222}Rn measurement runs were conducted for measuring the prompt scintillation pulse shape at different electric field configurations. They are called *krypton run* respectively *radon run 1* and *radon run 2* in the following. Krypton run data was taken during February 2019 at ~ 26 different fields in order to measure the pulse shape of ERs resulting from its 32.1 keV internal conversion (IC) decay. The two radon runs were conducted during August 2019 at ~ 17 fields respectively January 2020 at ~ 30 fields to measure scintillation caused by α-decays from ^{222}Rn, ^{218}Po and ^{214}Po.

The needed attenuation of the light hitting the top PMT is achieved by placing PTFE disks in front of it, as shown in Fig. 6.1. Their amount and thicknesses depend on whether ^{83m}Kr or ^{222}Rn (daughter) decays are to be measured. For the krypton run, a ~ 2 mm thick disk, called *krypton disk* in the following, with a central pinhole of ~ 200 µm diameter is used. The pinhole has been drilled through a central pilot hole of ~ 1 mm diameter and 1.8 mm depth. For the radon runs, two different disks, called *radon disks* from now on, are employed. The first disk is ~ 2 mm thick and has a central pinhole of ~ 300 µm diameter. The second disk contains no pinhole and is ~ 500 µm thick.

The krypton disk dimensions are the result of an iteration of measurements. In these, the amount of light seen by the top PMT when using different pinhole

diameters has been determined such, that the light level in the top PMT is reasonably close to 0.3 PE on average. Assuming Poissonian statistics, such a level would correspond to less than 4 % of events with more than one peak. Because these peaks would, in addition, also need to occur close to each other, the actual amount of merged peaks that could bias results would then be even lower.

In the case of radon daughter decays, such an iteration of measurements would have been too inefficient time-wise, as introducing ^{222}Rn into the HeXe TPC requires considerably more effort compared to ^{83m}Kr. There, a single measurement with the radon pinhole disk has been conducted to get an estimate for the remaining amount of photons hitting the top PMT. Afterwards, a series of dedicated measurements for determining the transmissivity of PTFE for xenon scintillation light, published in [82], has been made. Based on preliminary results of the published studies, the thickness of the second radon disk has been chosen with the same target light level as for the krypton run in mind.

Due to scintillation light only distributing itself over two PMTs, it has been found, that α-decays generate so many photons in the TPC, that saturation effects, such as signal distortions, become relevant if no attenuators were to be used. Accordingly, also the bottom PMT had PTFE attenuator disks placed in front of it during ^{222}Rn measurements. In radon run 1, the disk was $\sim 500\,\mu$m thick, while it was $\sim 700\,\mu$m thick in radon run 2. In both cases, the disks had no pinhole.

Pulse shape measurements themselves are conducted by filling the HeXe TPC with xenon such, that the volume observed by both PMTs is filled completely. As an indication for that, the capacitance of the medium levelmeter (see Section 4.1), whose upper end is above the top PMT window, is monitored while filling xenon until it does not change any longer, which indicates that the levelmeter is filled. Afterwards, both the recirculation pump and the hot gas purifier are switched on to start gas purification through the main line, drawing only from the LXe outlet at the support structure. Meanwhile, the sampling line is opened, including either of the sources, to introduce the radionuclides to measure into the xenon stream.

The details regarding the introduction of a source vary depending on the nuclide. In the case of ^{83m}Kr, the xenon flow is routed entirely through its source by slowly closing off the main line after having opened both source and sampling line. This results in a constant rate of ^{83m}Kr decays within the TPC over the duration of a measurement run after an initial grow-in period. Depending on the age of the source, DAQ rates of $\mathcal{O}(100\,\text{Hz})$ were usually reached.

For ^{222}Rn, the radon trap needs to be prepared at least one day in advance before a measurement. First, it is disconnected from the gas purification system and baked and pumped for a day afterwards. Meanwhile, an evacuated $\sim$ 50 mL glass pipette is filled with ^{222}Rn by expanding helium through an aqueous 20 kBq ^{226}Ra standard into it. The standard is the same as the one used in [65], and the radon extraction procedure is almost identical. The only difference is, that ^{222}Rn is expanded into the galas pipette first which then serves as a source instead of directly extracting from the ^{226}Ra standard. Having loaded the trap with ^{222}Rn, it is connected to the gas purification system again. When introducing ^{222}Rn, both trap and sampling line are opened for $\mathcal{O}$(1 min) before being closed off again. Because the radionuclide is introduced in a single pulse, the decay rate inside the TPC drops over the duration of the measurement run after the grow-in period instead of remaining constant. Depending on the amount of ^{222}Rn filled, DAQ rates at the order of $\mathcal{O}$(1 kHz) were reached.

After having introduced the radionuclide to measure, the system is left to equilibrate for several hours until both pressure and temperature inside the cryostat are stable. Following that, the PMTs are set to their operating voltages. The top PMT, which is supposed to only see signals with a size of a couple PE, is set to a voltage of -980 V (krypton run and radon run 1) or -1000 V (radon run 2) in order to operate close or at the maximum possible gain. This is done to reduce the impact of crosstalk and to improve the signal-to-noise ratio for single PE signals. Also, the PMT is connected to one of the factor 10 amplifier channels (Section 4.5) to utilize more of the digitizer's dynamic range to reduce the relative quantization error. The bottom PMT is set to a voltage of -900 V (all runs), which is a compromise between mitigating crosstalk and retaining a passable signal-to-noise ratio. It is connected to one of the amplifier's variable gain channels at minimum amplification (factor $\sim$ 2.2) to utilize more of the digitizer's dynamic range, but not using a larger amplification to avoid potential clipping of the signal.

Afterwards, an automatic ramp schedule is set up in the HV control software. The schedule consists of different HV grid voltage settings, determined in Section 6.1, which correspond to different electric field configurations within the drift volume. As soon as the first electric field setting is set, DAQ starts. Each field configuration in a schedule is kept for $\mathcal{O}$(1 h) before switching to the next one. Some of them are measured a second time after having gone through all other configurations once in order to check for reproducibility of the measurements. When switching between certain field strengths, the polarity of one or more grid needs to be changed, which requires to temporarily switch off the

HV modules supplying them. Correspondingly, separate schedules are generated based on grid polarity. As soon as a schedule has finished running, DAQ is paused, polarities are changed, and the next schedule corresponding to the new polarities is loaded.

6.3 Analysis of the scintillation pulse shape

6.3.1 Defining the event selection

Having recorded the necessary data, it is processed using the HeXe data processor. Afterwards, recorded events of a run undergo a two-step selection process. First, they need to be matched to an electric field configuration, as DAQ was not synchronized with voltage changes. For this purpose, grid and PMT voltages over the duration of a measurement run are exported from the slow control database to a text file. This file is read by a Python script which identifies time intervals over which all measured voltages remained constant while also determining points in time, where one or more HV channels tripped. Interval identification happens according to the following procedure:

1. Sequentially loop through all measured voltage data points for each HV channel. If the absolute difference between a data point and the one following it is larger than 2 V, it is marked as bad. Then, determine all cohesive intervals in time consisting of non-bad data points. Store the start and end timestamps of each cohesive interval in a file.
2. Calculate the average voltage of each cohesive interval. Compare the averages of neighboring intervals from the same HV channel and group them together if their difference is smaller than 2 V. Store the start and end timestamps of each group.
3. Sequentially iterate in parallel over the groups of each HV channel in the following way to determine time intervals of constant electric field configuration:
    a) Determine the groups with the latest start time, $t_{s,\mathrm{max}}$, the earliest end time, $t_{e,\mathrm{min}}$, as well as the channels they belong to.
    b) Check, if one of the groups starts later than $t_{e,\mathrm{min}}$. Should this not be the case, all groups overlap in time between $t_{s,\mathrm{max}}$ and $t_{e,\mathrm{min}}$. Store both timestamps in a list. Otherwise, do nothing.

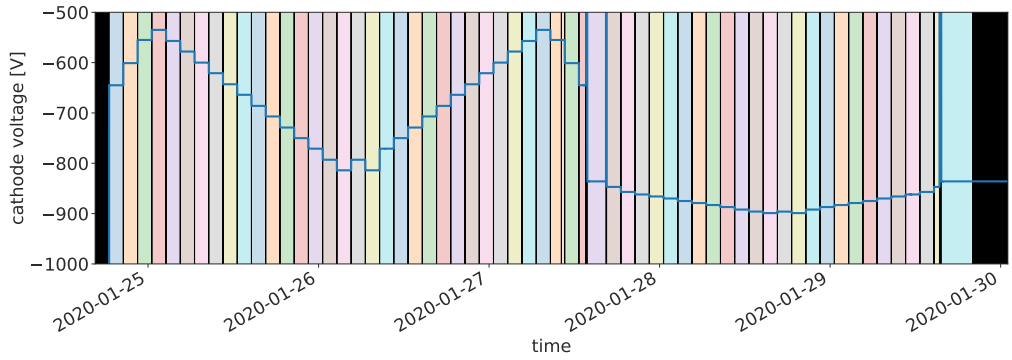

Figure 6.4: Cathode voltage during radon run 2. Colored intervals are detected field configurations, of which there are more than 50. Transition periods between configurations and times where an HV trip occurred or a non-targeted voltage has been measured are shaded in black.

c) Advance to the next group in the channel to which the group with $t_{e,\mathrm{min}}$ belongs.

d) Repeat the above procedure until there is no next group to advance to.

4. Loop through the list of electric field configuration intervals and calculate the average voltage of every channel within each interval. Compare each average to a list of allowed voltages for that channel. If there is no entry from which the average deviates by less than 2 V, the field configuration interval is removed from the interval list. This step is necessary to remove periods in time which technically constitute a constant field configuration, but where, for example, one of the PMTs was off because of a trip. Afterwards, store the start and end times of each interval in a file.

Fig. 6.4 shows the periods of constant field configuration found for radon run 2. All of them are correctly identified. The files generated during the identification process are used to determine whether an event occurred during a period of constant voltage in all channels and to which field configuration it belongs to based on its timestamp.

The second step of event selection involves a collection of parameter criteria which need to be passed. In the following, S1[n] refers to the nth largest peak, with S1[0] being the largest one.Initially, the subsequent list is applied for both $^{83\mathrm{m}}$Kr and ^{222}Rn data:

- All events must have occurred within the same constant field configuration interval. In addition, it must have occurred during a cohesive interval with good voltage data points, as defined above.
- Exactly one peak must be found in the top PMT waveform.

All remaining criteria depend on the used radionuclide. For the krypton run, the signature of the 32.1 keV decay being followed by a 9.4 keV decay with $T_{1/2} \sim 154$ ns [47] is exploited to by the following criteria:

- Exactly two peaks must be present in the bottom PMT waveform.
- The start, as identified by the data processor, of S1[1] must occur at least 160 ns after the start of S1[0]. This selects for the delayed coincidence signature. It also ensures, that photons originating from the second ^{83m}Kr decay do not affect the first ~150 ns of the first decay's photon arrival time distribution.

With all of the cuts mentioned so far applied, the S1[1] area is histogrammed together with the area of S1[0] one as seen in Fig. 6.5. A two-dimensional Gaussian is then fitted to the main population via χ^2 minimization by using the MIGRAD algorithm of MINUIT2[1]. An additional criterion for ^{83m}Kr data is then, that the areas of the largest and second-largest peak found in the bottom PMT must lie within the central 0.85 quantile of the fitted Gaussian. This method takes the field dependence of S1 signal sizes into account. Also, S1[1] must be larger than 10 PE to avoid cases, in which S1[0] and S1[0] are merged, with a third peak smaller than the two occurring in the bottom waveform at the same time.

For the radon runs, the following set is used instead:

- Exactly one peak must be present in the bottom PMT waveform.
- The area of that peak must be within the following limits:
  - Radon run 1: [400 PE, 900 PE]
  - Radon run 2: [187 PE, 420 PE]

  This is done in order to select the population containing the ^{222}Rn, ^{218}Po, and ^{214}Po α-decays. The corresponding area distributions on which the selections are based are shown in Fig. 6.6, top. Based on only the spectra, it is not possible to clearly identify the population which contains the

[1] MINUIT2 is a C++ re-write, provided by ROOT [90], of the MINUIT minimization package [91].

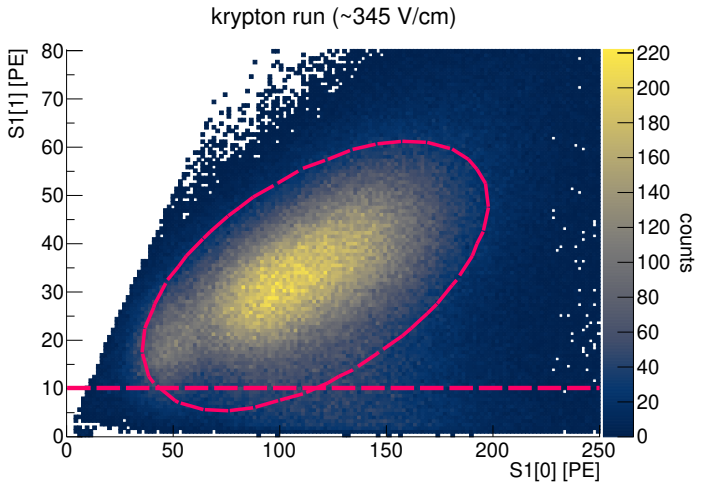

Figure 6.5: Example histogram via which the fit for defining the krypton run peak area selection is made. Events need to be both within the ellipse and above the horizontal dashed line.

α-decays. However, immediately following radon run 2, a dual-phase measurement was conducted using the same attenuator configuration. The availability of an additional S2 signal allows to specifically select events which occur in the drift volume. Plotting S2[0] (largest S2 signal) versus S1[0] size as in Fig. 6.6, top, allows to identify the peak at $\sim$ 300 PE in the radon run 2 spectrum as the correct one (compare to the radon analysis in [92]). Based on that, the peak can also be identified in radon run 1. The bounds are chosen to cut into the peak in order to avoid adjacent populations with, as of, now, unknown origin. It is possible, that these originate both from ^{214}Bi β-decays, which can coincide with γ-rays at energies of $\mathcal{O}(1\,\mathrm{MeV})$, or from α-decays which do not happen inside the drift volume. Because the scintillation signal size changes only by about 2.5 for electric fields up to 1.2 kV/cm [93], it is not necessary to update this selection for each field configuration.

- Both height h and area A of the peak must match the following criterion:
  - Radon run 1: $A < -1868\,h$
  - Radon run 2: $A < -2300\,h$

  Targeted by this cut are events containing signals with a different height-to-area ratio which are already present in data before introducing ^{222}Rn into the TPC. They are either produced by cosmogenic muons crossing

the sensitive volume, or by background radiation. The corresponding population and the selection bound, for radon run 2, are displayed in Fig. 6.7.

Finally, one can have a look at the average amount of PE seen by the top PMT by applying the criteria as defined above, except for the requirement on the number of peaks found in the top waveform. The result for the krypton and radon runs is shown in Fig. 6.8. The need for an upper bound on the top peak area, at least for the radon runs, is immediately clear. Consequently, a final requirement on the top peak area is added to all runs:

- Krypton run: $0.1\,\mathrm{PE} < \mathrm{area} < 1.0\,\mathrm{PE}$
- Radon runs: $0.1\,\mathrm{PE} < \mathrm{area} < 0.65\,\mathrm{PE}$

The lower boundary is utilized to protect against potential noise wrongly identified by the data processor as a signal candidate. The upper boundaries are selected in order to conservatively remove merged peaks and are varied when fitting the arrival time spectra in the next section.

6.3.2 Fitting the photon arrival time spectra

Defining the photon arrival time

Using the selections defined in the previous section, a suitable value for the height fraction κ for defining the rising and falling edge of a peak (see Section 4.6) needs to be determined for a robust definition of a photon arrival time parameter. The calculation of the rising/falling edge time, $t_{\mathrm{rise/fall}}$ via linear interpolation can be expressed via:

$$t_{\mathrm{rise/fall}} = t_l + \frac{t_r - t_l}{S_r - S_l}(\kappa h - S_l), \tag{6.3}$$

with $S_{l/r}$ describing the value of the sample to the left respectively right of the point in the waveform where the height fraction κ is reached, $t_{l/r}$ being the corresponding time, and h denoting the peak height. To analyze the influence of fluctuations and biases in $S_{l/r}$ and h, which occur because of noise and remaining digitizer artefacts, the partial derivatives of the rising/falling edge

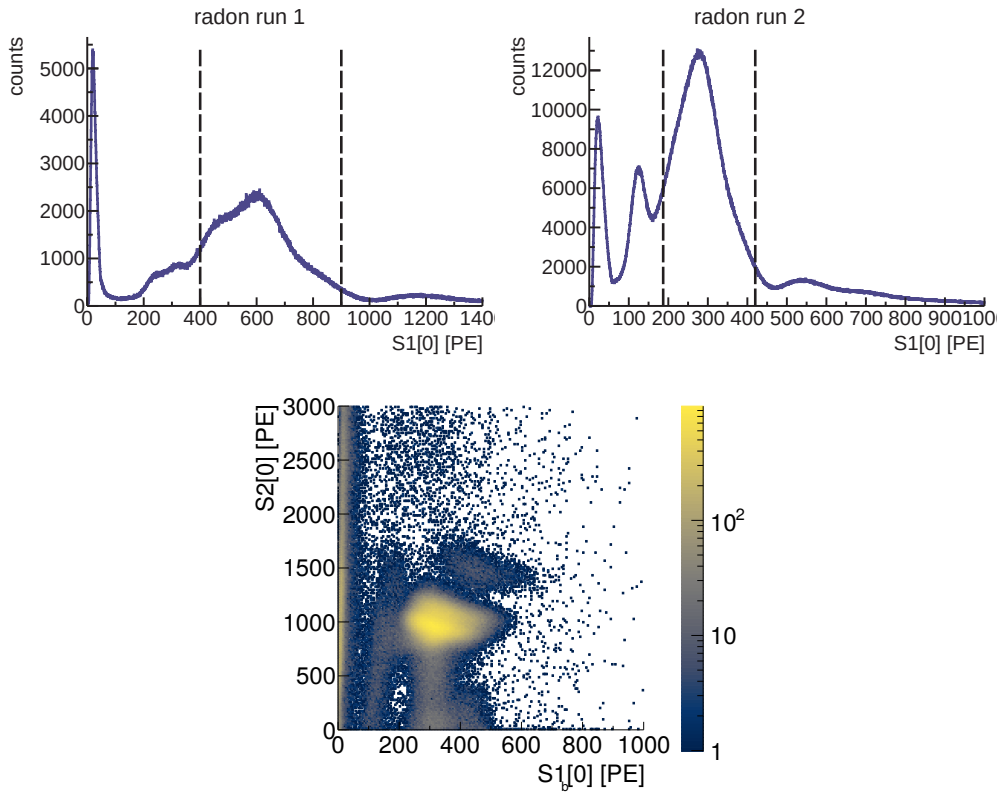

Figure 6.6: Plots illustrating how the bottom peak area is to be selected for radon runs. Top: Bottom peak area spectra for both radon runs, including selection bounds. Bottom: S2[0] versus $S1[0]_b$ histogram of a dual-phase measurement immediately succeeding radon run 2, which uses the same attenuators. $S1[0]_b$ is the area of an S1 signal seen by the bottom PMT only. The only cuts used are requiring a coincidence level larger than 1 for both signals, which corresponds to them being visible in both PMTs, and that the time between the two, the drift time, is within [5 µs, 25 µs]. This avoids events close to both cathode and gate, which, for the measurement depicted, are around 0 µs and 30 µs. The ^{214}Po population at about (500 PE, 1600 PE) is clearly separated from the one containing ^{222}Rn and ^{218}Po, which is at roughly (350 PE, 1000 PE). Also, the ratio between the S1 signal sizes is roughly equivalent to the energy ratio between ^{222}Rn α-particles (5.59 MeV) and ^{214}Po α-particles (7.83 MeV). Energy values are from [94].

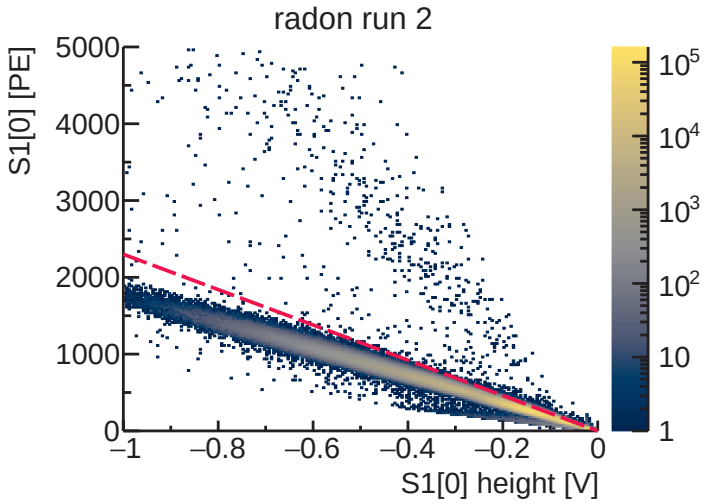

Figure 6.7: Location of the intrinsically broader bottom peak signals in the area versus height space. A dashed line shows the boundary below which events need to lie in order to be accepted.

estimator are taken with respect to these parameters:

$$\frac{\partial t_{\text{rise/fall}}}{\partial S_l} = \frac{t_r - t_l}{S_r - S_l}\left(\frac{\kappa h - S_l}{S_r - S_l} - 1\right) \tag{6.4}$$

$$\frac{\partial t_{\text{rise/fall}}}{\partial S_r} = -\frac{t_r - t_l}{S_r - S_l}\frac{\kappa h - S_l}{S_r - S_l} \tag{6.5}$$

$$\frac{\partial t_{\text{rise/fall}}}{\partial h} = \frac{t_r - t_l}{S_r - S_l}\kappa \tag{6.6}$$

It is evident, that the resulting fluctuations and biases induced into $t_{\text{rise/fall}}$ are smaller, the larger the difference $S_r - S_l$ is. Accordingly, κ should be chosen such, that the rising/falling edge corresponds to the steepest point of a PMT signal.

For the top PMT, the analysis can be based on single PE signals which are expected to have a stable shape. To determine their shape, a dataset from radon run 1 is used to fit an exponentially modified Gaussian to each peak found in the top PMT waveform via χ^2 minimization. This function has the form [95]:

$$f(x \mid A, \mu, \sigma, \tau) = \frac{A}{2\tau} e^{\frac{1}{2}\left(\frac{\sigma}{\tau}\right)^2} e^{\frac{-(x-\mu)}{\tau}} \operatorname{erfc}\left[\frac{1}{\sqrt{2}\sigma}\left(\frac{\sigma^2}{\tau} - (x-\mu)\right)\right], \tag{6.7}$$

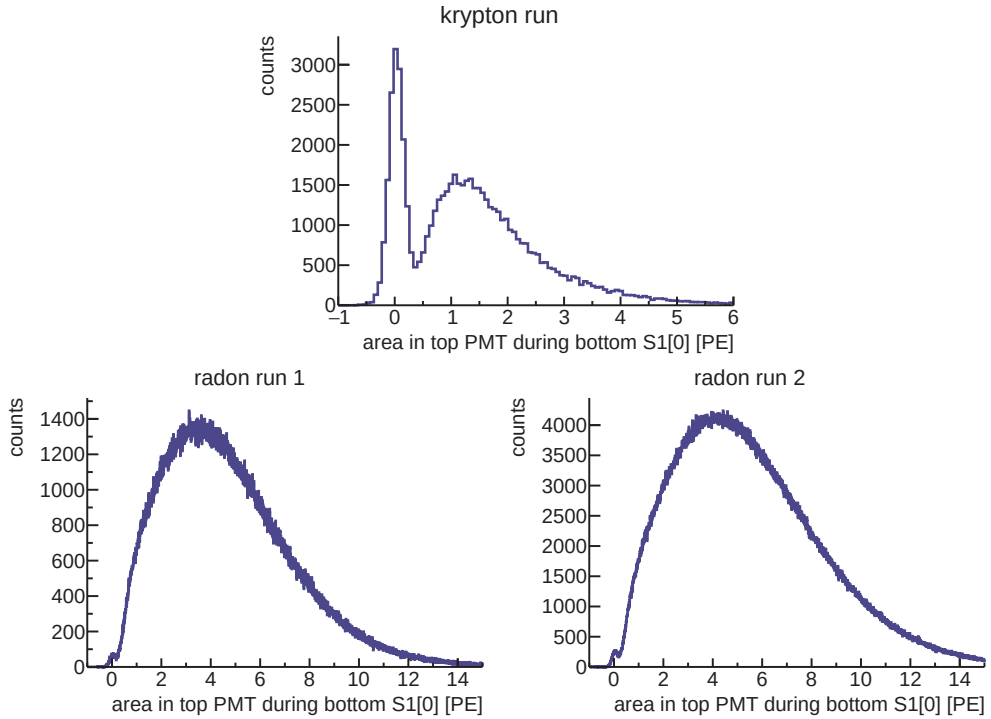

Figure 6.8: Area seen by the top PMT over the duration of the largest bottom PMT peak, without any requirement on the number of peaks found in the top waveform. The light level in the krypton run is reasonably close to the targeted value of 0.3 PE (roughly 0.5 PE on average measured), while this is evidently not the case for the radon runs. The mismatch between expected and observed value is because of the attenuator thicknesses having been based on a preliminary analysis for [82], which had to be updated after the review process.

with the complementary error function:

$$\mathrm{erfc}(x) = \frac{2}{\sqrt{\pi}} \int_x^\infty e^{-t^2} dt, \tag{6.8}$$

and is the result of a convolution of a Gaussian distribution with amplitude A, mean μ and standard deviation σ, with an exponential distribution with decay constant τ. For the fit, all samples within a peak's interval are used. As evident from Fig. 6.9, top, the function gives a good description of the single PE signals in the top PMT, especially for the rising flank.

The resulting fit parameter distributions are shown in Fig. 6.9, bottom. To now determine values for κ, the central parameter values are used to numerically determine the inflection points of the resulting exponentially modified Gaussian. They lie at $\sim$ 55 % of the peak height in the rising flank and $\sim$ 85 % in the falling flank, respectively. Because the inflection point in the rising flank corresponds to the steepest point of the single PE signal, the rising edge with $\kappa = 0.55$ is taken as the timing parameter. The bottom PMT parameter is selected to be $\kappa = 0.30$ based on varying the parameter such, that it is as small as possible while still being robust against digitizer artefacts (see Fig. 5.11).

Based on the results above, the photon arrival time Δt is defined as the difference between the $\kappa = 0.55$ rising edge of the top PMT signal and the $\kappa = 0.3$ rising edge of the bottom PMT signal. Using all of the above selection criteria, the resulting normalized photon arrival time spectra are displayed in Fig. 6.10 for subsets of the field configurations of each pulse shape measurement run. For the krypton run spectra, a trend towards earlier arrival time for larger fields is visible. In radon run 1, the distributions above $\sim$ 200 V/cm are similar, while the distributions below that value exhibit a sudden drop of their maximum. The reason for this drop could not be determined. For radon run 2, the spectra look identical at first glance. The next section shows, whether the radon 1 drop is also seen in the extracted pulse shape parameters.

Parameter estimation

To finally extract the effective pulse shape parameters, two sets of model functions are fit to the Δt spectra. For the krypton run, the function is:

$$F_1(\Delta t \mid t_0, \sigma_t, f_s, \tau_s, \tau_t) := f_s \; p_s(\Delta t) + (1 - f_s) \; p_t(\Delta t), \tag{6.9}$$

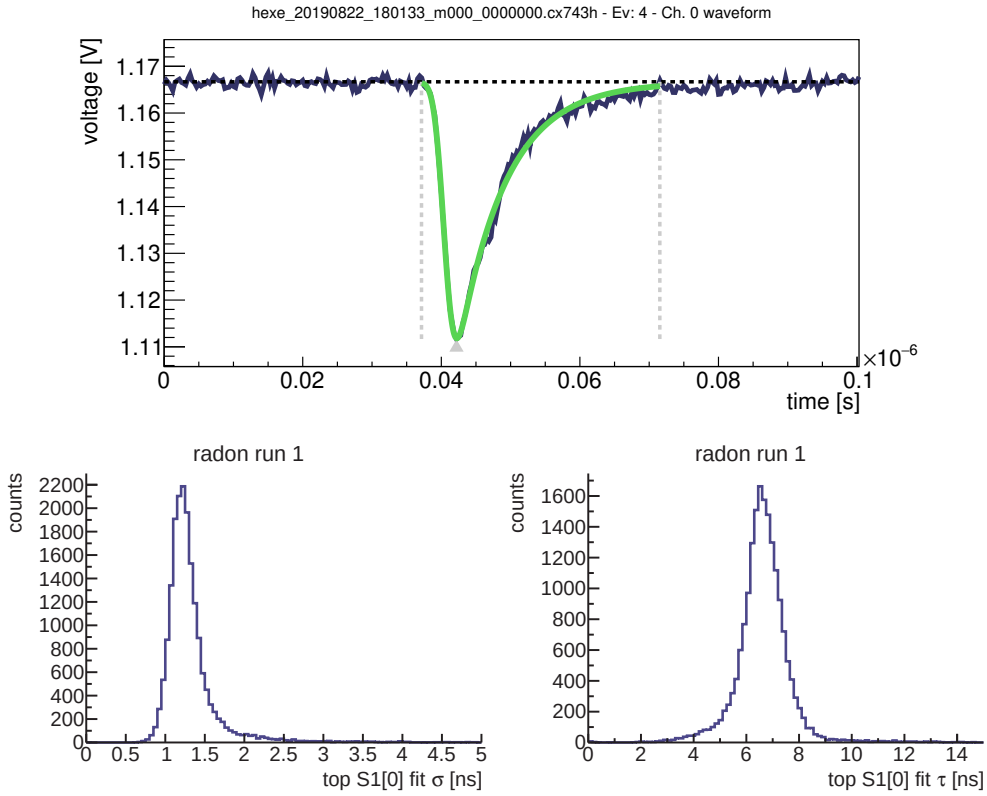

Figure 6.9: Fit of Eq. (6.7) to single PE signals in the top PMT waveform, using data from radon run 1. Top: Event view from the data processor which shows the fit. Bottom: Fit parameter distributions after using the corresponding radon run selection criteria and requiring, that the fit is successful and that the fit χ^2 is smaller than 500, which is found to remove fits to merged peaks which are reported as successful, but do not give a good fit at all. Values are $\sigma = (1.3 \pm 0.4)$ ns and $\tau = (6.62 \pm 0.10)$ ns.

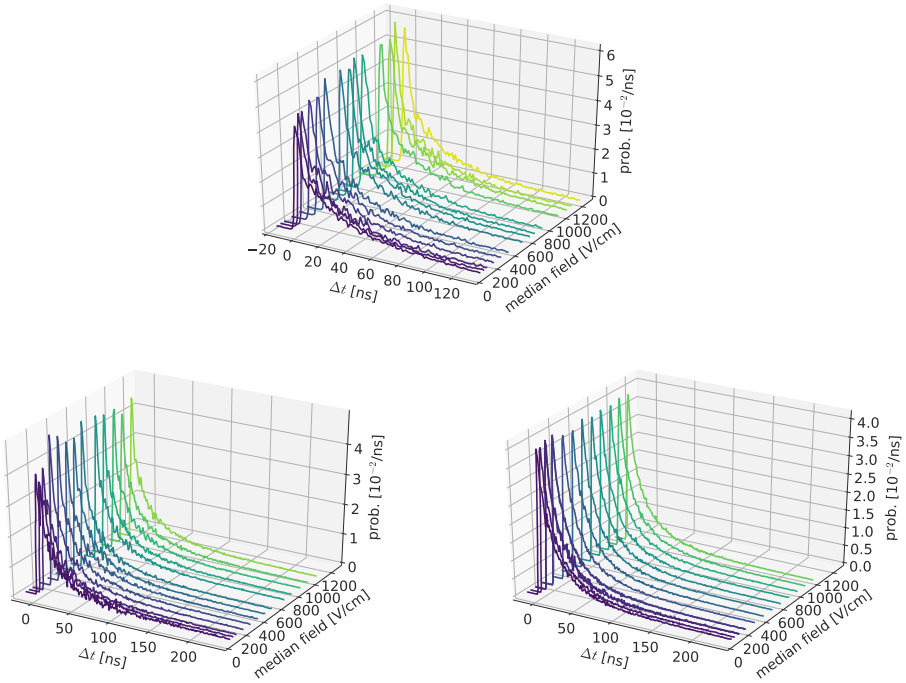

Figure 6.10: Δt spectra for each pulse shape measurement run field values are estimated according to Section 6.1.3. Top: Krypton run. Bottom left: Radon run 1. Bottom right: Radon run 2.

with t_0 being the scintillation start time plus any other offset between the two signal times, σ_t the time resolution, τ_s the effective singlet lifetime, τ_t the effective triplet lifetime, f_s the effective singlet fraction, and the $p_i(\Delta t)$ being a short-hand notation for Eq. (6.7) into which the corresponding parameters are inserted and which is multiplied with a normalization factor $1/N_i$:

$$p_i(\Delta t) := \frac{1}{N_i(t_0, \sigma_t, \tau_i, t_{\min}, t_{\max})} f(\Delta t \mid 1, t_0, \sigma_t, \tau_i). \tag{6.10}$$

The normalization, used to ensure that the p_i are probability density functions when restricting event selection to a minimum respectively maximum time difference $\Delta t_{\min/\max}$, is given by:

$$\begin{aligned} N_i(t_0, \sigma_t, \tau_i, \Delta t_{\min}, \Delta t_{\max}) = & \frac{1}{2}\left[\operatorname{erfc}\left(\frac{\Delta t_{\min} - t_0}{\sqrt{2}\sigma_t}\right) - \operatorname{erfc}\left(\frac{\Delta t_{\max} - t_0}{\sqrt{2}\sigma_t}\right)\right] - \\ & \frac{1}{2} e^{\frac{1}{2}\left(\frac{\sigma_t}{\tau_i}\right)^2} \\ & \left\{ e^{\frac{-(\Delta t_{\max} - t_0)}{\tau_i}} \left(2 - \operatorname{erfc}\left[\frac{1}{\sqrt{2}\sigma_t}\left((\Delta t_{\max} - t_0) - \frac{\sigma_t^2}{\tau_i}\right)\right]\right) - \right. \\ & \left. e^{\frac{-(\Delta t_{\min} - t_0)}{\tau_i}} \left(2 - \operatorname{erfc}\left[\frac{1}{\sqrt{2}\sigma_t}\left((\Delta t_{\min} - t_0) - \frac{\sigma_t^2}{\tau_i}\right)\right]\right)\right\}, \end{aligned} \tag{6.11}$$

which results from an analytic integration of $f(\Delta t \mid 1, t_0, \sigma_t, \tau_i)$ between $\Delta t_{\min}$ and $\Delta t_{\max}$. This is the typical two-component scintillation model as presented in Section 1.2, additionally convoluted with a Gaussian distribution to model timing uncertainties. Modelling the uncertainty with a Gaussian has been done in previous pulse shape analyses, such as [18, 86, 89].

For the radon runs, a third component is added as it is found, for reasons outlined later in this section, to be needed to properly describe the tailing towards larger Δt:

$$F_2(\Delta t \mid t_0, \sigma_t, f_s, f_3, \tau_s, \tau_t, \tau_3) := f_3 p_3(\Delta t) + (1 - f_3)\, F_1(\Delta t \mid t_0, \sigma_t, f_s, \tau_s, \tau_t), \tag{6.12}$$

where τ_3 describes the lifetime of that component, and f_3 its fraction. Note, that the meaning of f_s in the context of F_2 changes to describe the effective singlet fraction when considering singlet and triplet decays only.

Parameter estimates are extracted from the arrival time spectra by utilizing the

ROOT::Fit interface provided by ROOT to construct the unbinned negative log-likelihood, which is then minimized using the methods provided by MINUIT2. In a first step, an interval of starting values for the free parameters is specified based on reported literature values, if applicable, and results obtained form exploratory fits done manually. Minuit's SCAN algorithm then determines an improved starting point for minimization by scanning the likelihood within this interval. Afterwards MIGRAD is run twice for minimization: First with σ_t and the τ_i constrained to positive values, then unconstrained while using the parameters of the previous MIGRAD call as starting values. Finally, MINOS determines the 1σ confidence intervals of each parameter based on the profile likelihood method. If MINOS is not successful, approximate errors from HESSE, which calculates the Hessian matrix of the negative log-likelihood at the found minimum, are used.

The range of the fit is constrained for the krypton and radon runs as follows:

- Krypton run: $\Delta t \in [-5.5\,\text{ns}, 135\,\text{ns}]$
- First radon run: $\Delta t \in [-3.25\,\text{ns}, 240\,\text{ns}]$
- Second radon run: $\Delta t \in [2.5\,\text{ns}, 240\,\text{ns}]$

The upper bound for the krypton run is chosen based on the 160 ns minimum distance to the second $^{83\text{m}}$Kr decay peak and to allow for variation. For the radon runs, it is to avoid the bipolar signal present at the end of every waveform as reported in Section 5.2 while also leaving space for varying the bound. The lower bounds are selected such, that the fit range starts at a point within the left flank of the arrival time distribution where an oscillatory pattern, which is attributed to the digitizer's baseline pattern and described in the next paragraph, is roughly at a zero crossing.

Because the number of parameters in F_2 is rather high and some of them, like t_0, σ_t and τ_s are found to be highly correlated with each other ($|r| > 0.8$ from HESSE covariance matrix estimates), many of the radon run fits are highly unstable when leaving all parameters free and fail to converge when slightly changing starting values or event selection criteria. As signal sizes are constant during a radon run, the resolution parameter σ_t is assumed to be constant over the duration of such a run. In an initial series of fits, the values of σ_t are extracted from successful fits. This gives $\sigma_t = (1.67 \pm 0.06)\,\text{ns}$ for the first radon run, calculated using 15 fits, and $\sigma_t = (1.550 \pm 0.018)\,\text{ns}$ for the second radon run, calculated using 44 fits. Afterwards, σ_t is fixed to the central value of the corresponding estimate and varied within $\pm 1\sigma$ during the systematic uncertainty analysis later on.

Representative example fits are shown in Fig. 6.11 for the krypton run, Fig. 6.12 for radon run 1, and Fig. 6.13 for radon run 2, where the model function using the extracted parameter values is shown laid over a histogram of Δt. In all distributions, the aforementioned oscillatory pattern is visible in the fit residuals. It is strongest in the fits for radon run 1, where the signals seen by the bottom PMT are also the largest. The oscillation has a period of about 5 ns in the radon runs, which is equivalent to the period of the digitizer baseline pattern. In the krypton run, it is much weaker in comparison, with the period seeming to rather correspond to 10 ns, which is twice the baseline pattern period. It is concluded, based on these findings, that the oscillation is caused by the baseline pattern correction not being able to account for signal line gain differences which occur before respectively after a baseline calibration measurement, which is also concluded in Section 5.2. It is worst for the second radon run because there, the signals seen by the bottom PMT deviate the most from the baseline, while the correction is most reliable the closer a signal's amplitude is to the baseline. In both radon runs, the pattern causes a "shoulder" in the left-hand flank of the Δt distribution, which makes it difficult to properly constrain σ_t.

The influence of the pattern is also visible when attempting to determine the goodness of fit via χ^2. First, Δt is histogrammed such, that more than 90 % of bins contain at least 10 events. This ensures, that the assumption of Gaussian statistics for the event number in each bin, which is needed or a valid χ^2 test, is true in good approximation. For each measurement run, the following histogram parameters are chosen:

- Krypton run: $[-2.5\,\text{ns}, 60\,\text{ns}]$, 100 bins
- First radon run: $[0\,\text{ns}, 150\,\text{ns}]$, 150 bins
- Second radon run: $[0\,\text{ns}, 150\,\text{ns}]$, 150 bins

While one has to look out for caveats when interpreting p-values from a χ^2 test while using parameters which are not extracted from a χ^2 fit [96], being this careful is not necessary here. This is because typical $\chi^2/N_{\text{d.o.f.}}$ values are larger than 2 for the krypton run and 4 for the radon runs, which implies p-values that are essentially zero. Based on the residual plots, this is attributed to the oscillatory pattern.

To estimate the magnitude of systematic errors, the following set of analysis parameters is varied compared to the values given in Section 6.3.1:

- σ_t, if fixed: $\pm 1\sigma$ of initial estimate (radon)

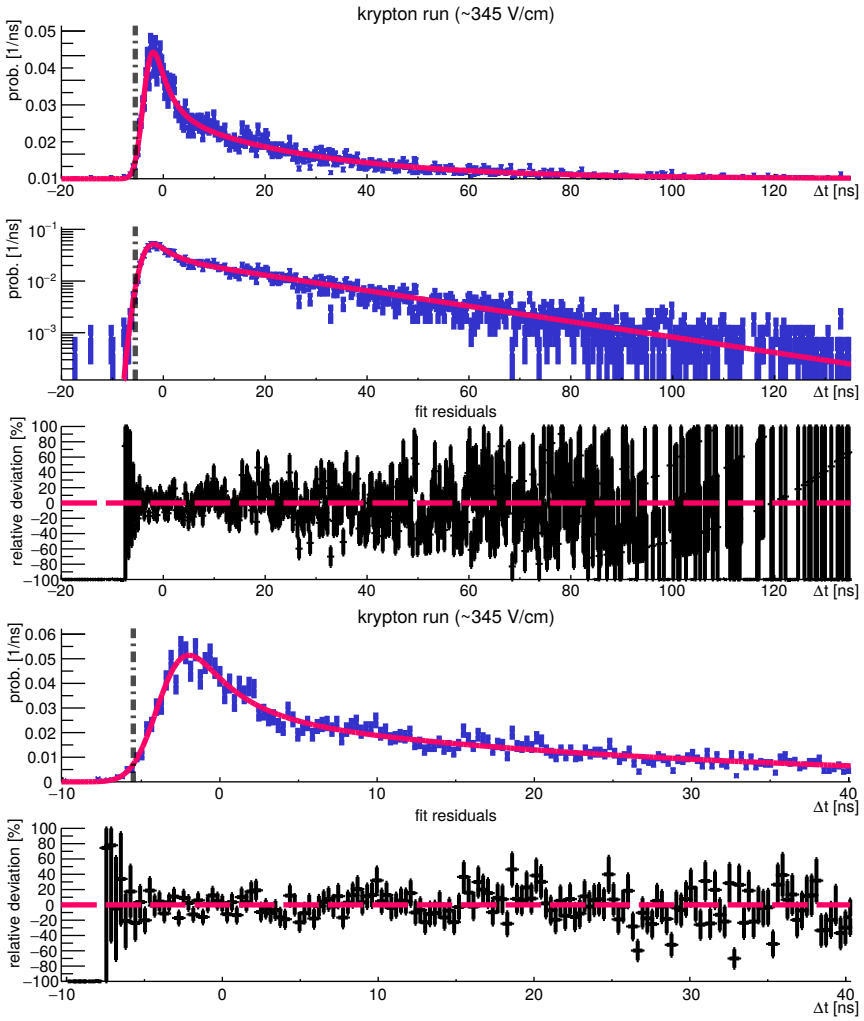

Figure 6.11: Representative fit to krypton run data and its residual. The vertical dashed line indicates the start of the fit range. Top: Including full fit range and with both linear and logarithmic y-axis. Bottom: View zoomed closer to the start of the fit range.

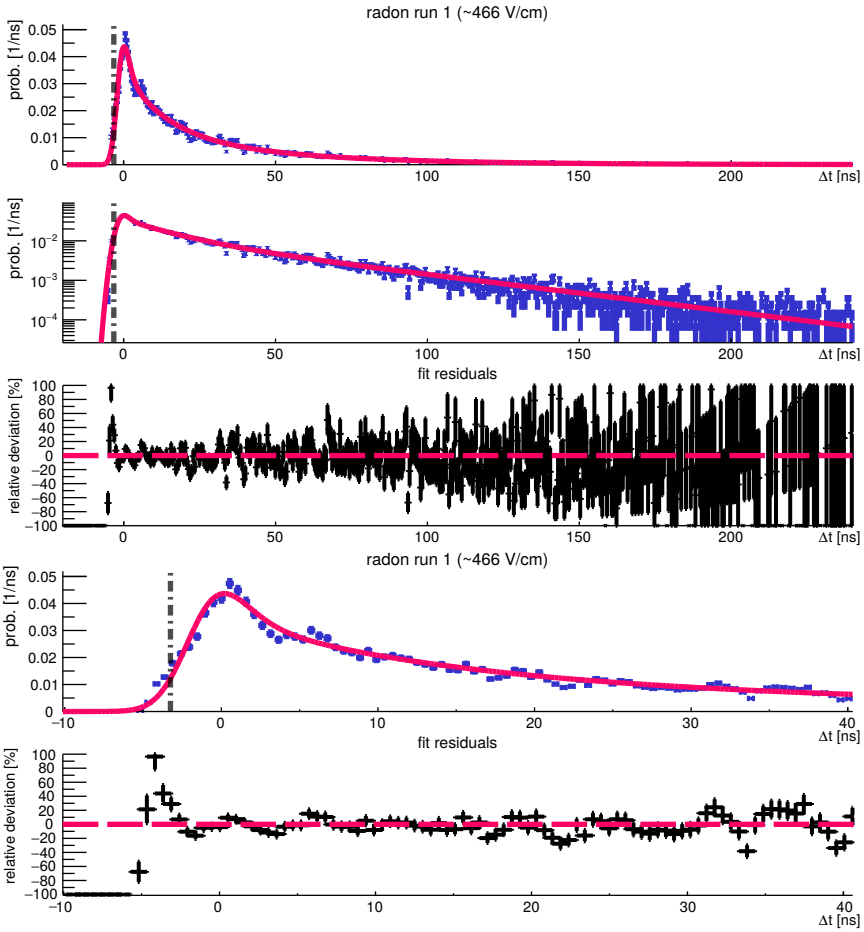

Figure 6.12: Representative fit to radon run 1 data and its residuals. The vertical dashed line indicates the start of the fit range. Top: Including full fit range and with both linear and logarithmic y-axis. Bottom: View zoomed closer to the start of the fit range.

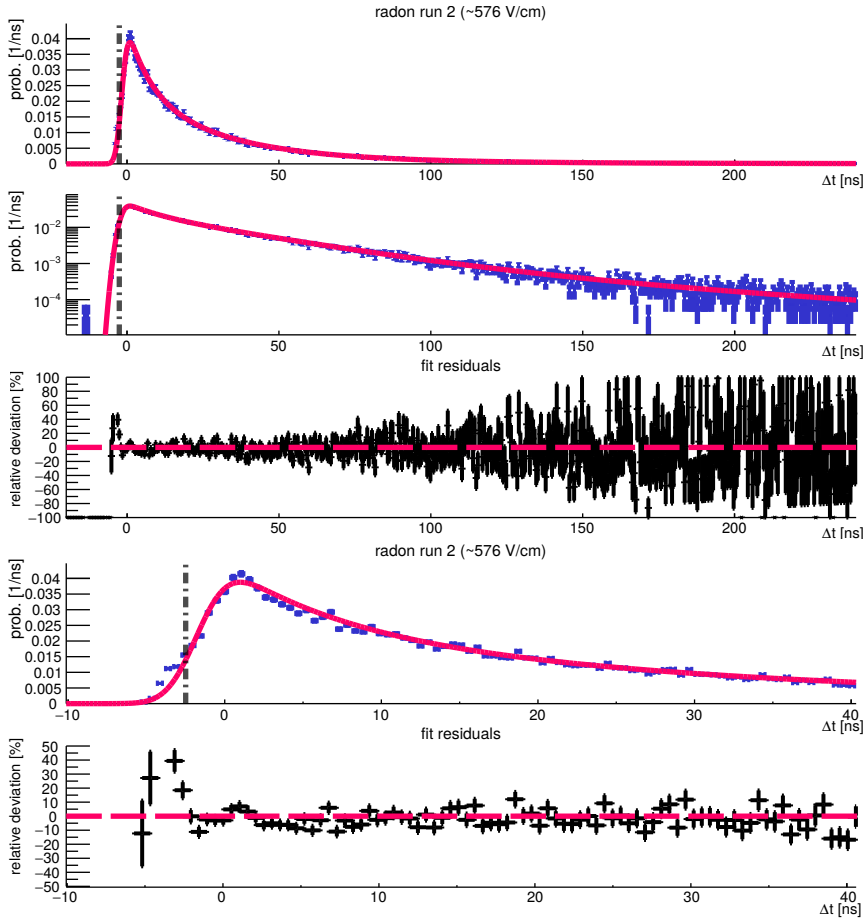

Figure 6.13: Representative fit to radon run 2 data and its residuals. The vertical dashed line indicates the start of the fit range. Top: Including full fit range and with both linear and logarithmic y-axis. Bottom: View zoomed closer to the start of the fit range.

- Ellipse selection quantile ±0.05 (krypton)
- Upper top peak area limit: ±0.1 PE (all)
- Upper fit bound: ±15 ns (krypton), ±260 ns (radon)
- Lower fit bound: ±1.25 ns (krypton)

All fits are repeated while varying all parameters simultaneously. The maximum and minimum values of a fit parameter then define the upper and lower bound of the corresponding systematic error. Initially, it was also planned to quantify the impact of the lower fit bound for radon data. However, it was found that the fit is still too unstable when varying that bound, resulting in the majority of fits failing for at least one parameter configuration. Only field configurations for which all fits are successful are taken into account. This results in the number of available field configurations for analysis to drop by about a factor ~ 2 for the krypton run and radon run 2, while it is more than a factor ~ 3 for radon run 1, where systematics are worst. The number of remaining data points is still sufficient to span the measured field range.

For the results, the central parameter estimates resulting from fitting are used together with the corresponding median field estimates $\hat{E}$. The statistical and systematic parameter errors are added up directly to yield the total parameter error. The field error is denoted by the endpoints of the IQR.

6.4 Fit results and discussion

Fit results are shown in Fig. 6.14 for the krypton run and in Fig. 6.15 for the radon runs, together with values from other publications. Averaged results are displayed in Table 6.1 for krypton above 500 V/cm, where the measured f_s is constant within the sensitivity of this analysis, and Table 6.1 for radon. In the following, the short-hands for the publications as indicated in the cited figures will be used when discussing them.

The krypton run results are in agreement with each other when taken at the same field and indicate, that the effective singlet fraction f_s is rising when the electric field becomes stronger. This is consistent with what is reported in [18] and by *Hogenbirk2018A* as well as *Hogenbirk2018B*. Values as measured in this work are consistent with *Hogenbirk2018A* data for ERs at (25 ± 3) keV, which is close to the energy of the 32.1 keV ^{83m}Kr decay. While no direct comparison with *XMASS2016* data at similar energies is possible because fields close

Table 6.1: Krypton run results averaged over all values at $\hat{E} > 500\,\mathrm{V/cm}$.

Parameter	value				
τ_s	$(2.5$	$\pm$	0.3_{stat}	$^{+0.8}_{-1.1\mathrm{sys}})$	ns
τ_t	$(28.2$	$\pm$	0.3_{stat}	$^{+1.2}_{-0.8\mathrm{sys}})$	ns
f_s	0.184	$\pm$	0.006_{stat}	$^{+0.02}_{-0.03\mathrm{sys}}$	
σ_t	$(1.28$	$\pm$	0.05_{stat}	$^{+0.5}_{-0.3\mathrm{sys}})$	ns

to 0 V/cm could not be reached, it is not implausible for a continuation of the trend seen in this work towards lower fields to be compatible. When comparing to *Hogenbirk2018B* data, f_s is systematically larger. This would match the hypothesis stated in [22] and *Hogenbirk2018A*, that f_s generally increases with larger linear energy transfer (LET) respectively stopping power. The *Hogenbirk2018B* data was taken using 511 keV γ-rays. Applying the Compton scattering formula[2] to determine the maximum electron recoil energy gives $\sim$ 340 keV, which is an order of magnitude larger compared to the IC electrons from $^{83\mathrm{m}}$Kr. According to the ESTAR model [98] for calculating the electron stopping power for different elements, xenon has a stopping power of more than 4.77 MeV cm^2/g for electrons with energies of 32.1 keV and lower, while it is about 1.24 MeV cm^2/g for 340 keV electrons. The LUX2018 value is significantly smaller and thus incompatible with values measured by this work and *Hogenbirk2018A*, even though the energy range is similar.

As for the effective lifetimes, the measured τ_s values are in agreement with *LUX2018* and *Hogenbirk2018A*. The central values seem to drop towards lower fields. However, this coincides with upward fluctuations of σ_t, which strongly correlates with τ_s. As a consequence, no variation of τ_s is seen within the sensitivity of the analysis down to a field of $\sim$ 70 V/cm. τ_t qualitatively follows the same general trend as indicated in *Hogenbirk2018B* by increasing towards lower fields, which would also match observations in [18, 20] and conform to the hypothesis, that recombination becomes slow enough for its dynamics to affect the pulse shape. However, the τ_t values of this work converge to a significantly larger value at large field strengths compared to *Hogenbirk2018B*. It furthermore does not match *Hogenbirk2018A* and *LUX2018*, both which have been taken in a similar energy range. Because, as discussed above, the stop-

[2] See, for example, [97], page 87.

Table 6.2: Radon run results averaged over all values.

Parameter	value run 1	value run 2
τ_s	$(6.7 \pm 0.5_{\text{stat}}\ ^{+0.6}_{-4.0\text{sys}})$ ns	$(4.13 \pm 0.16_{\text{stat}}\ ^{+0.8}_{-2.5\text{sys}})$ ns
τ_t	$(31.1 \pm 1.7_{\text{stat}}\ ^{+4.1}_{-11.6\text{sys}})$ ns	$(23.9 \pm 0.4_{\text{stat}}\ ^{+3}_{-4\text{sys}})$ ns
f_s	$0.24 \pm 0.04_{\text{stat}}\ ^{+0.03}_{-0.06\text{sys}}$	$0.132 \pm 0.004_{\text{stat}}{}^{+0.04}_{-0.02\text{sys}}$
τ_3	$(50\ ^{+3340}_{-50}{}_{\text{stat}}{}^{+540}_{-50}{}_{\text{sys}})$ µs	$(67\ ^{+16}_{-6}{}_{\text{stat}}\ ^{+26}_{-16\text{sys}})$ ns
f_3	$0.17 \pm 0.04_{\text{stat}}\ ^{+0.30}_{-0.10\text{sys}}$	$0.260 \pm 0.010_{\text{stat}}{}^{+0.30}_{-0.10\text{sys}}$

ping power for $^{83\text{m}}$Kr decay electrons is larger on average than that for Compton electrons produced by ^{22}Na 511 keV γ-rays, the discrepancy cannot be explained by slower recombination. Otherwise, this would contradict with the notion of recombination being faster at higher densities. Instead, a systematic deviation might possibly be caused by the region between anode and gate inside the HeXe TPC. For field values towards the maximum one achieved, anode and gate voltages are set to nearly identical voltages by the field optimization script because only the drift volume is optimized. This results in a 5 mm thick low-field region which, when doing a back-on-the-envelope comparison with the 5 cm drift volume, might be the point of origin for about 10 % of the events in the Δt spectrum. The long decay times in the low-field region then would bias the measured τ_t towards larger values. This possible effect would also bias f_s towards smaller values.

In summary, the krypton result is generally in agreement with other published values. The tension in τ_t remains to be investigated, which is only possible by reducing electric field systematic uncertainties.

The radon run results of this work are comparable to each other, although this is also due to the large systematic uncertainties which are caused by fit instabilities and parameter correlations. Compared to the zero-field data of *Hitachi1983* and *Teymourian2011*, the central values of the estimates for τ_s and τ_t scatter around them, indicating reasonable agreement. Comparing with the results averaged over all fields (Table 6.2) under the assumption, that the pulse shape only changes negligibly, confirms this. The τ_t value of run 2, which is less affected by systematics compared to run 1, is also closer to the values reported for ERs towards higher fields, which are discussed in the above paragraphs. Because the absolute change in recombination is known to only change little

with field for α-particle tracks [93] compared to ERs, the lifetime of the triplet component is not affected by low-field regions within the HeXe TPC as with krypton.

However, there is tension regarding the value of f_s, also when comparing to krypton data which shows a higher f_s value even though the ^{222}Rn α-decays are subject to higher stopping powers. The most likely reason is, that parameters cannot be easily compared with each other because *Hitachi1983*, *Teymourian2011* and the krypton run analysis use two-component models, while this work added a third component. The anticorrelation visible between f_s and f_3 at low fields points towards the parameters of the third component absorbing a part of the singlet contribution, which could explain the lower f_s value also compared to krypton data (Table 6.1). Another unknown bias could, in addition, affect the *Hitachi1983* value, as the model it is extracted from uses a constant offset which is left as a free parameter. Such a constant offset might be capable of absorbing part of the triplet contribution, which would increase the observed f_s value. While *Teymourian2011* reports a value similar to *Hitachi1983*[3], the pulse shape measurement is only of secondary nature to their publication, which is primarily about photosensor characterization. As a consequence, no analysis has been performed by them regarding the error on their reported f_s value.

Parameter estimates for the third component are generally unstable, especially for radon run 1. Based on radon run 2 values, it makes up a fraction of about $f_3 \sim 0.26$ of the entire photon arrival time spectrum, with a lifetime of roughly $\tau_3 = 70\,\mathrm{ns}$. The origin of that component is unknown as of now, but it is needed to describe the far end of the Δt distribution's right-hand tail (see the example fit in Fig. 6.13). It is not possible based on the currently available data to determine, whether it amounts to another excited xenon state, or if it is an impurity mixed with the LXe which is excited and also emits photons in the sensitive range of the PMTs. An analysis- or detector-based effect being the cause should also be considered.

Generally, the radon data is in agreement with other published values. The measurements are strongly affected by systematic uncertainties, which makes it difficult to provide precise values using the data presented here. Even the drop of the maximum probability density observed for fields $< 200\,\mathrm{V/cm}$, reported in Section 6.3.2, does not affect the fit parameters at a comparable magnitude. The only hint might be the larger central values of τ_s and f_s, which

[3] When assuming that they erroneously stated the inverse of the singlet-to-triplet ration, which is implied by the inverse value they cited for *Hitachi1983*.

could be explained by the singlet component absorbing a part of the triplet contribution because the minimization algorithm tends to larger τ_s values due to the smaller maximum.

In light of the difficulties encountered during data analysis, the following paragraphs contain approaches for reducing the amount of systematic uncertainty. The two largest identified contributors to it are the TPC regions outside the drift volume and the oscillatory baseline pattern. Regions outside the drift volume contribute the most to the size of $\delta_{\hat{E}}$ and could bias certain fit parameters, such as f_s and τ_t. The oscillatory baseline pattern is detrimental to the performance of the fit, especially close to the left-hand flank of the Δt spectrum which is essential for constraining σ_t and τ_s.

To address the baseline pattern issue, future pulse shape measurements should include a pattern calibration measurement at both the start and the end of a run to yield a more accurate model of the pattern and its dependence on input voltage. Further communication with CAEN and the digitizer designers is needed to evaluate, if any hardware-side improvements are possible.

Communication with the manufacturer is also needed for a potential solution for reducing systematic electric field uncertainties. This solution includes synchronizing both the V1724 and V1743 digitizers and operating in dual-phase mode. Operating in dual-phase mode is not useful when utilizing the V1743 only, as its maximum acquisition window size only amounts to 320 ns, while drift times between S1 and S2 are, at the very least, at $\mathcal{O}(1\,\mu s)$. Using both digitizers when triggering on an S1 signal, the V1724 would be able to record both the S1 and S2 signal, while the V1743 would record the S1 signal at high time resolution. This makes it possible to obtain a clean selection of events which occur within the drift volume by requiring both an S1 and S2 signal to be present. In addition, the presence of both signals allows for a significantly improved energy selection, as evidenced by Fig. 6.6, bottom. Dual-phase operation would have allowed to cleanly separate ^{214}Po α-decays from those of ^{222}Rn and ^{218}Po. It should also prove to be beneficial when measuring the pulse shape of particle interactions resulting from other decays, such as 511 keV γ-rays from positron annihilation coming from the β^+-decay of ^{22}Na. The improved energy resolution is expected to allow for a clean selection of the full absorption peak as in [21].

Another avenue for getting better results is to improve the fit procedure. Using the measured Δt values, which in this work essentially are only limited by an upper bound Δt_{max}, one can calculate their empirical mean $\hat{\mu_{\Delta t}}$. This should, on average, correspond to the expected value $E[\Delta t]$ of the true probability density

function up to a bias which results from the upper range limit. Assuming a probability density function $p(t)$ for Δt, one can express the expected value as:

$$\begin{aligned} E[\Delta t] &= \int_{-\infty}^{\infty} t\,p(t)\,dt = \int_{-\infty}^{\Delta t_{\max}} t\,p(t)\,dt + \int_{\Delta t_{\max}}^{\infty} t\,p(t)\,dt \\ &= E[\hat{\mu_{\Delta t}}] \int_{-\infty}^{\Delta t_{\max}} p(t)\,dt + \int_{\Delta t_{\max}}^{\infty} t\,p(t)\,dt, \end{aligned} \tag{6.13}$$

which contains the expected value of $\hat{\mu_{\Delta t}}$:

$$E[\hat{\mu_{\Delta t}}] = \frac{\int_{-\infty}^{\Delta t_{\max}} t\,p(t)\,dt}{\int_{-\infty}^{\Delta t_{\max}} p(t)\,dt}. \tag{6.14}$$

The expected value when using Eq. (6.7) as a probability density for Δt is ([99], page 24):

$$E[\Delta t] = \mu + \tau. \tag{6.15}$$

Utilizing the linearity of the expected value, this would result in the following expression when using the full model probability density function Eq. (6.9):

$$E[\Delta t] = t_0 + f_s\tau_s + (1 - f_s)\,\tau_t. \tag{6.16}$$

Combining everything yields, after rearranging:

$$\begin{aligned} t_0 =& E[\hat{\mu_{\Delta t}}] \int_{-\infty}^{\Delta t_{\max}} F_1(t \mid t_0, \sigma_t, f_s, \tau_s, \tau_t)\,dt + \\ & \int_{\Delta t_{\max}}^{\infty} t F_1(t \mid t_0, \sigma_t, f_s, \tau_s, \tau_t)\,dt - f_s\tau_s - (1 - f_s)\,\tau_t. \end{aligned} \tag{6.17}$$

This can be interpreted as an implicit equation for t_0. One could then calculate $\hat{\mu_{\Delta t}}$ by splitting the samples of a field configuration into two statistically independent subsamples. This would allow to either constrain $\hat{\mu_{\Delta t}}$ and thus t_0, or, if the error on $\hat{\mu_{\Delta t}}$ is negligible compared to other sources of uncertainty, to eliminate t_0 altogether. The idea for this method for parameter elimination came too late to be investigated in this thesis, but it serves as a starting point for future pulse shape measurements which fit the photon arrival time distribution.

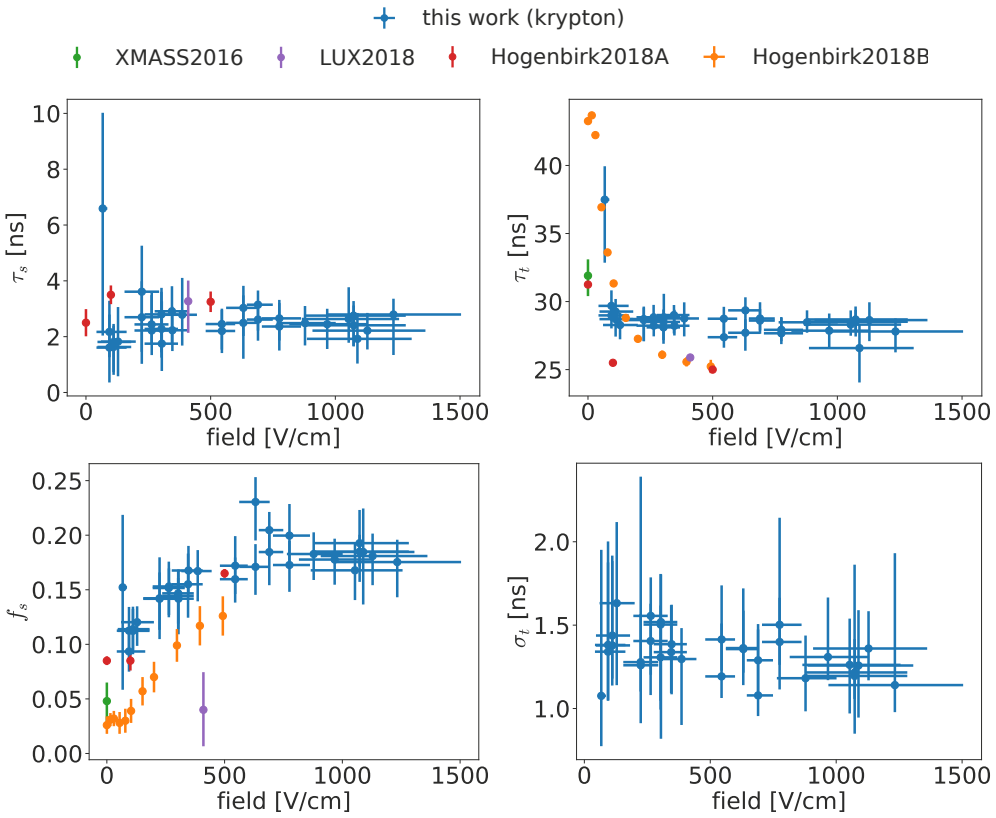

Figure 6.14: Parameter results from the krypton run. The data points used for comparison are taken from [88] (*XMASS2016*), [60] (*LUX2018*), [89] (*Hogenbirk2018A*) and [21] (*Hogenbirk2018B*). The sources used in each comparison measurement are:
XMASS2016 — ERs with an energy of (27 ± 12) keV induced by ^{57}Co γ-rays.
LUX2018 — ERs with an energy between 5 keV and 46 keV induced by ^{14}C and tritium β-decays.
Hogenbirk2018A — ERs with an energy of (25 ± 3) keV induced by ^{137}Cs and ^{22}Na γ-rays as well as background radiation.
Hogenbirk2018B — ERs from the full absorption peak of ^{22}Na 511 keV positron-annihilation γ-rays.

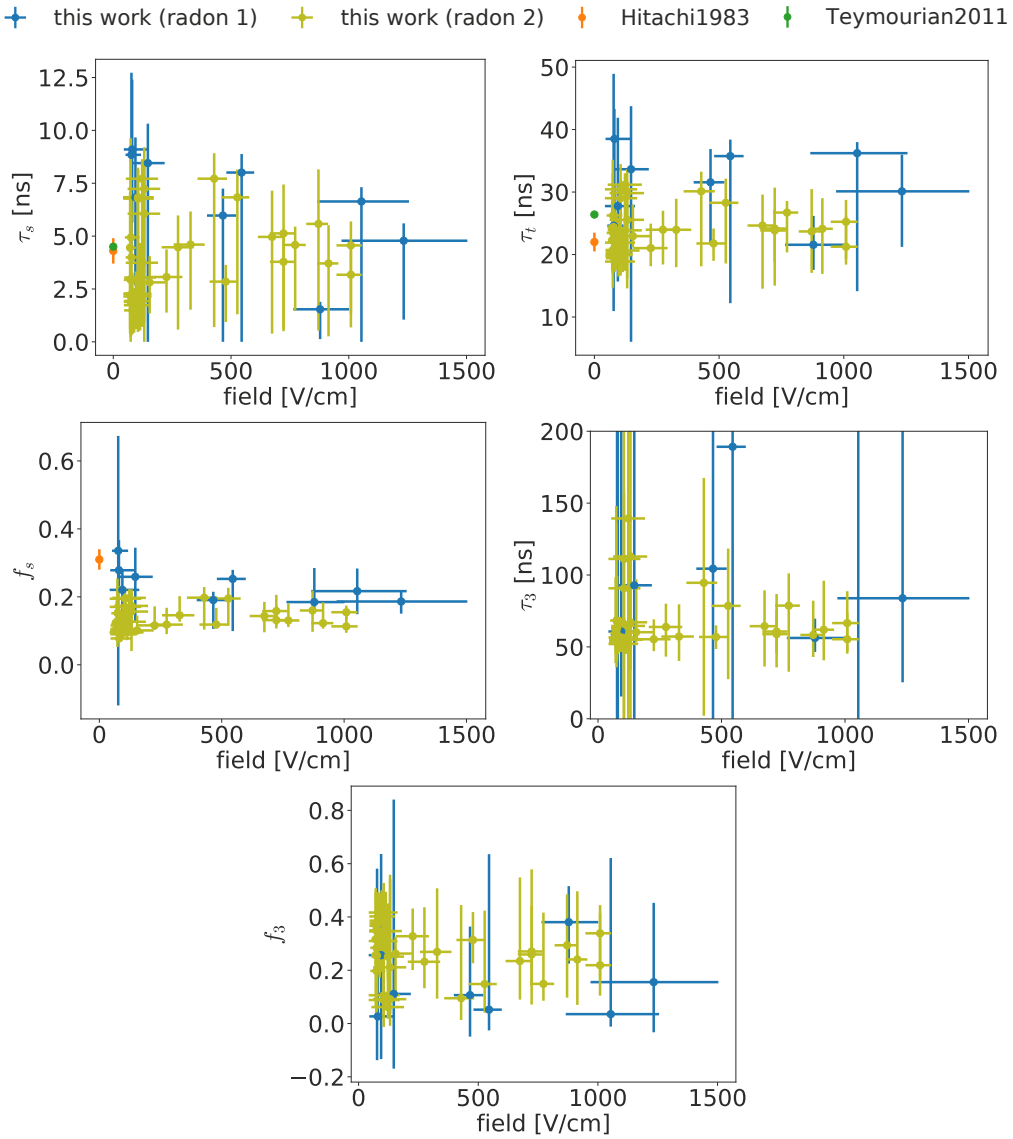

Figure 6.15: Parameter results from the radon runs. The data points used for comparison are taken from [22] (*Hitachi1983*) and [87] (*Teymourian2011*). Both references use ^{210}Po α-decays for measuring the Δt spectrum. Only data points for which an error is reported in the corresponding publication are used. Not all values for τ_3 are shown, as some of them have values and errors orders of magnitude larger than those of the shown τ_3 values.

7 Summary, conclusions and outlook

In this work, Chapter 1 illustrates the role of LXe detectors in BSM physics searches, focussing on dark matter and the neutrinoless double-beta decay. An overview regarding the properties of xenon and the microphysics responsible for charge and light signal generation in LXe to argue, why LXe is a well-suited medium for rare event searches. In addition, the working principle of xenon dual-phase TPCs is explained, as it is the type of LXe detector the setups utilized in this work belong to.

One of these detectors was XENON1T, presented in Chapter 2. At the time of writing, the limits it provided for SI WIMP-nucleon cross-sections at WIMP masses above 6 GeV are still world-leading, with a minimum of 4.1×10^{-47} cm^2 at 90 % confidence level for at WIMP mass of 30 GeV/c^2 [23]. At the time of writing, its upgrade, XENONnT [33], is in commissioning.

The analyses in Chapter 3 deal with the detector physics of the XENON1T LXe TPC. In Section 3.1, Fourier spectra of baseline waveforms are analyzed, based on a previous analysis [55], to assess the impact of HV low-pass filters, called filter boxes [35], on noise conditions and whether noise remained stable during science data taking. This is done for different frequency ranges which correspond to certain features in the spectrum. Some of these features can be traced back to the HV power supply and the V1724 digitizer modules based on signal channel and phase correlations. While some PMT signal cable operations resulted in visible noise jumps for some channels, noise was generally stable during both SR 0 and SR 1. The filter boxes successfully suppressed noise coming from the HV modules by up to 80 % and more depending on the signal channel, with the average being $\sim$ 51 %. Averaged over all frequencies, the total noise reduction amounts to $\sim$ 22 %. Based on the success of both the filter boxes and the identification of noise sources by analyzing Fourier spectra, both techniques are going to be utilized in XENONnT.

Section 3.2 is about the identification of gas events. Such events contain S2 signals from interactions that occur within the gas phase of the TPC and, for that reason, have to be removed for physics analyses. While a cut based on an S2's width in time already removes such events to some extent, another cut had been developed for the analysis of SR 0 and SR 1 data which uses the fraction of an S2 signal seen by the top PMT array. This fraction is called area fraction top (AFT) in the context of the XENON1T analysis. It was found, that the cut's performance outside the SI WIMP analysis ROI deteriorates towards higher energies. This is mainly caused by PMTs into which xenon leaked during operation of XENON1T. These have high afterpulses (APs) that modify the single PE response, which becomes relevant especially at large amounts of light seen. Because of this and the amount of xenon inside those PMTs growing over time, the selection space exhibits both an energy and a time dependence.

For this reason, the cut is updated in this work to be applicable over the entire energy range observed in XENON1T in light of analyses at higher energies compared to the SI WIMP one, such as setting limits for the neutrinoless double-beta decay. To achieve this, contributions of high AP PMTs to S2 signal sizes are discarded when calculating the selection parameters. The result of the redefinition is a selection which accepts 99 % of LXe single-site interactions and rejects $\sim$ 100 % of gas events above S2 sizes of 600 PE. The acceptance only shows a minor dependence on time and the location of the interaction site in the TPC for interactions which originated either at least 25 cm below the gate grid, or have an S2 smaller than 10^5 PE.

In addition, the gas event population investigated during analysis imply, that the top PMT array screening mesh could, in combination with PMTs that are set a potential lower than the mesh, locally generate an electric field pointing towards the space between screening mesh and anode. Ionization electrons from interactions between top array and screening mesh would then drift towards the anode and potentially result in a gas phase S2 signal. Should this hypothesis prove itself to be true, for example during the commissioning of XENONnT which also uses screening meshes, measures could be taken to reduce the amount of gas events. This would be important for S2-only analyses which sacrifice background separation for a lower recoil energy threshold, as no efficient gas event discrimination using an S2's width or AFT is possible at the lowest energies.

The final XENON1T detector physics analysis in this work (Section 3.3), evaluates to what degree it is possible to use S1 PSD for discriminating between ERs

and NRs in cases, where the usual discrimination based on the S2/S1 ratio cannot be applied. This is especially important for surface background originating from ^{210}Pb which plated-out onto the PTFE reflector panels of the TPC [23]. Ionization electrons generated by the β-decays of such ^{210}Pb are trapped by the PTFE surface and cause the S2/S1 ratio to attain values which would be more likely for a NR than an ER. Inspired by [60], the fraction of a signal's charge within its first 30 ns, called prompt fraction here, is used as a pulse shape parameter. It allows to reach up to 75 % rejection power against ERs at 50 % NR acceptance according to the prompt fraction distributions of ER and NR samples selected from calibration data. In addition, the prompt fraction is taken together with the S2/S1 ratio to train a classifier which yields a combined discrimination parameter. The analysis in this work indicates, that this parameter performs slightly better than the S2/S1 ratio on its own for S1 sizes below 50 PE. For larger sizes, the sensitivity of this analysis does not allow to decide if the combined parameter performs better or not compared to the S2/S1 ratio.

Considering the ^{210}Pb surface background and the fact, that PSD could provide up to a factor 3 reduction as reported by [59] at drift fields smaller than 100 V/cm, PSD could play a very important role for future LXe dual-phase TPCs. This is mainly because it has become more and more challenging to achieve fields at $\mathcal{O}$(100 V/cm) in recent experiments as they grow in detector size [63]. Also, while methods for removing ^{210}Pb and other radon daughters from PTFE surfaces have been investigated recently [100], they do not remove all of it.

The LXe scintillation pulse shape itself provides an avenue to a deeper understanding of the microphysics involved in LXe signal generation, as it depends, for example, on how many ionization electrons recombine after a particle interacts with LXe. This could help with building models for predicting scintillation and charge yield. Also, one could assess whether PSD is viable in a certain energy range or not.

In this work, the pulse shape is measured for various radionuclides using the HeidelbergXenon (HeXe) system, detailed in Chapter 4. The system contains a 100 g-scale LXe TPC which recently has been used for xenon purity studies [66] and the measurements in this thesis. The measurements presented herein were made while operating the TPC in single-phase mode. Two different digitizers with different sampling rates are available, with the measurements in this work using the CAEN V1743 which is capable of sampling at an effective rate of 3.2 GHz.

Chapter 4 describes the necessary preparations before measuring and analyzing the pulse shape. It is concerned with the calibration of the HeXe PMTs as well as with quantifying and correcting for raw data artefacts. The latter are caused by the time interleaving principle the V1743 utilizes to achieve its high sampling rate, and signal crosstalk between the PMT signal lines.

Finally, Chapter 6 describes the actual pulse shape measurements and their analysis. The LXe scintillation shape is measured for the 32.1 keV IC decay of ^{83m}Kr as well as for the α-decays of ^{222}Rn, ^{218}Po and ^{214}Po at varying field configurations, ranging from $\sim 70\,\mathrm{V/cm}$ up to $\sim 1200\,\mathrm{V/cm}$, using single photon sampling achieved by placing PTFE disks in front of the PMTs. For this, a FEA calculation of the electric field inside the TPC is used to determine the potentials to set the HV grids to in order to achieve a certain field configuration during measurement. Afterwards, the calculated field is weighted with photon detection probabilities, simulated via an optical MC of the TPC, to yield a better estimate for the probability for the electric field value in the region a photon came from. At the end, the measured photon arrival spectra are used to fit a two- respectively three-component model to them to extract the pulse shape parameters.

The shape parameters extracted from ^{83m}Kr data and their dependence on the electric field and stopping power generally agree well with previous publications, although there are indications that regions outside the TPC drift volume might bias the results. For the ^{222}Rn data, the parameters reasonably agree with other published values, but show inconsistencies which are attributed to having to use a different model function and to large systematic uncertainties caused by the digitizer artefacts. Still, it is, to the best knowledge of the author, the first measurement of the LXe α-particle scintillation pulse shape at such a wide range of field configurations. Despite the inconsistencies, it can be assumed based on the data, that the measured pulse shape for ^{222}Rn, ^{218}Po and ^{214}Po is constant up to $\sim 1200\,\mathrm{V/cm}$ within the sensitivity of this analysis. It is argued by the author, that measurements using HeXe would benefit from measuring the pulse shape in dual-phase operation employing both the V1724 and V1743 digitizer in parallel, which would allow an improved energy selection and to constrain the location an interaction came from. Also, it is possible to express a fit parameter from the utilized model function in terms of the other parameters, when reserving a subsample of the measured photon arrival time spectrum for an auxiliary measurement.

References

1. Aprile, E. & Doke, T. Liquid Xenon Detectors for Particle Physics and Astrophysics. *Rev. Mod. Phys.* **82**, 2053 (2010).
2. Chepel, V. & Araujo, H. Liquid noble gas detectors for low energy particle physics. *JINST* **8**, R04001 (2013).
3. Aghanim, N. *et al.* Planck 2018 results. VI. Cosmological parameters. *Astron. Astrophys.* **641**, A6 (2020).
4. Zwicky, F. Die Rotverschiebung von extragalaktischen Nebeln. *Helv. Phys. Acta* **6**, 110 (1933).
5. Rubin, V. C., Ford, W. K. J. & Thonnard, N. Extended rotation curves of high-luminosity spiral galaxies. IV. Systematic dynamical properties, Sa through Sc. *Astrophys. J. Lett.* **225**, L107 (1978).
6. Rubin, V. C., Thonnard, N., Ford, W. K. J. & Burstein, D. Rotational properties of 23 SB galaxies. *Astrophys. J.* **261**, 439 (1982).
7. Clowe, D., Gonzalez, A. & Markevitch, M. Weak lensing mass reconstruction of the interacting cluster 1E0657-558: Direct evidence for the existence of dark matter. *Astrophys. J.* **604**, 596 (2004).
8. White, S. D. M., Frenk, C. S. & Davis, M. Clustering in a neutrino-dominated universe. *Astrophys. J. Lett.* **274**, L1 (1983).
9. Bertone, G. The moment of truth for WIMP dark matter. *Nature* **468**, 389 (2010).
10. Jungman, G., Kamionkowski, M. & Griest, K. Supersymmetric dark matter. *Phys. Rept.* **267**, 195 (1996).
11. Planck collaboration. *The Legacy Explanatory Supplement* `https://wiki.cosmos.esa.int/planck-legacy-archive`. Accessed on 1 November 2020.
12. Lewin, J. D. & Smith, P. F. Review of mathematics, numerical factors, and corrections for dark matter experiments based on elastic nuclear recoil. *Astropart. Phys.* **6**, 87 (1996).

13. Avignone, F. T., Elliott, S. R. & Engel, J. Double beta decay, Majorana neutrinos, and neutrino mass. *Rev. Mod. Phys.* **80**, 481 (2008).

14. Anton, G. *et al.* Search for Neutrinoless Double- β Decay with the Complete EXO-200 Dataset. *Phys. Rev. Lett* **123**, 161802 (2019).

15. Veazey, W. *CRC handbook of chemistry and physics* ISBN: 9781482260977 (Chemical Rubber Pub. Co, Boca Raton, Fla).

16. Lorents, D. C. The physics of electron beam excited rare gases at high densities. *Physica B+C* **82**, 19 (1976).

17. Lenardo, B. *et al.* A Global Analysis of Light and Charge Yields in Liquid Xenon. *IEEE Transactions on Nuclear Science* **62**, 3387 (2015).

18. Kubota, S., Hishida, M. & Ruan(Gen), J.-z. Evidence for a triplet state of the self-trapped exciton states in liquid argon, krypton and xenon. *J. Phys. C Solid State* **11**, 2645 (1978).

19. Fujii, K. *et al.* High-accuracy measurement of the emission spectrum of liquid xenon in the vacuum ultraviolet region. *Nucl. Instrum. Meth. A* **795**, 293 (2015).

20. Dawson, J. V. *et al.* A study of the scintillation induced by alpha particles and gamma rays in liquid xenon in an electric field. *Nucl. Instrum. Meth. A* **545**, 690 (2005).

21. Hogenbirk, E., Decowski, M. P., McEwan, K. & Colijn, A. P. Field dependence of electronic recoil signals in a dual-phase liquid xenon time projection chamber. *JINST* **13**, P10031 (2018).

22. Hitachi, A. *et al.* Effect of ionization density on the time dependence of luminescence from liquid argon and xenon. *Phys. Rev. B* **27**, 5279 (1983).

23. Aprile, E. *et al.* Dark Matter Search Results from a One Ton-Year Exposure of XENON1T. *Phys. Rev. Lett.* **121**, 111302 (2018).

24. Akerib, D. S. Results from a Search for Dark Matter in the Complete LUX Exposure. *Phys. Rev. Lett.* **118**, 021303 (2017).

25. Cui, X. Dark Matter Results from 54-Ton-Day Exposure of PandaX-II Experiment. *Phys. Rev. Lett* **119**, 181302 (2017).

26. Althüser, L. *Light collection efficiency simulations of the XENON1T experiment and comparison to data* MA thesis (Westfälische Wilhelms-Universität Münster, 2017). https://www.uni-muenster.de/imperia/md/content/physik_kp/agweinheimer/theses/master_lutz_alth__ser.pdf.

27. Aprile, E. *et al.* The XENON1T Dark Matter Experiment. *Eur. Phys. J. C* **77**, 881 (2017).

28. Aprile, E. *et al.* Observation of two-neutrino double electron capture in ^{124}Xe with XENON1T. *Nature* **568**, 532 (2019).

29. Aprile, E. *et al.* Energy resolution and linearity of XENON1T in the MeV energy range. *Eur. Phys. J. C* **80**, 785 (2020).

30. Aalbers, J. *et al.* DARWIN: towards the ultimate dark matter detector. *JCAP* **11**, 017 (2016).

31. Agostini, F. *et al.* Sensitivity of the DARWIN observatory to the neutrinoless double beta decay of ^{136}Xe. *Eur. Phys. J. C* **80**, 808 (2020).

32. Aprile, E. *et al.* Excess electronic recoil events in XENON1T. *Phys. Rev. D* **102**, 072004 (2020).

33. Aprile, E. *et al.* Projected WIMP Sensitivity of the XENONnT Dark Matter Experiment. arXiv: 2007.08796 [physics.ins-det] (2020).

34. Aprile, E. *et al.* XENON1T Dark Matter Data Analysis: Signal Reconstruction, Calibration and Event Selection. *Phys. Rev. D* **100**, 052014 (2019).

35. Aprile, E. *et al.* The XENON1T Data Acquisition System. *JINST* **14**, P07016 (2019).

36. Aprile, E. *et al.* Lowering the radioactivity of the photomultiplier tubes for the XENON1T dark matter experiment. *Eur. Phys. J. C* **75**, 546 (2015).

37. Aprile, E. *et al.* Material radioassay and selection for the XENON1T dark matter experiment. *Eur. Phys. J. C* **77**, 890 (2017).

38. Aprile, E. *et al.* ^{222}Rn emanation measurements for the XENON1T experiment. arXiv: 2009.13981 [physics.ins-det] (2020).

39. Akerib, D. S. *et al.* Technical results from the surface run of the LUX dark matter experiment. *Astropart. Phys.* **45**, 34 (2013).

40. Levy, C. *Light Propagation and Reflection off Teflon in Liquid Xenon Detectors for the XENON100 and XENON1T Dark Matter Experiment* PhD thesis (Westfälische Wilhelms-Universität Münster, 2014). https://repositorium.uni-muenster.de/document/miami/42495273-2cc7-4632-99af-accf074921e7/diss_levy.pdf.

41. Neves, F. *et al.* Measurement of the absolute reflectance of polytetrafluoroethylene (PTFE) immersed in liquid xenon. *JINST* **12**, P01017 (2017).

42. Barrow, P. *et al.* Qualification Tests of the R11410-21 Photomultiplier Tubes for the XENON1T Detector. *JINST* **12**, P01024 (2017).

43. Phillips Scientific. *Model 776 data sheet* http://www.phillipsscientific.com/pdf/776ds.pdf. Accessed on 01 October 2020.

44. CAEN S.p.A. *V1724 User Manual (revision 32)* (2017). https://www.caen.it/products/v1724/. Accessed on 28 April 2020.

45. Aprile, E. *et al.* The pax data processor v6.8.0. *Zenodo.* doi:10.5281/zenodo.1195785 (2018). Code repository containing versions past v6.8.0 at <https://github.com/XENON1T/pax>, accessed on 01 October 2020.

46. Aprile, E. *et al.* Physics reach of the XENON1T dark matter experiment. *JCAP* **04**, 027 (2016).

47. Kastens, L. W., Bedikian, S., Cahn, S. B., Manzur, A. & McKinsey, D. N. A 83Krm Source for Use in Low-background Liquid Xenon Time Projection Chambers. *JINST* **5**, P05006 (2010).

48. Manalaysay, A. *et al.* Spatially uniform calibration of a liquid xenon detector at low energies using 83m-Kr. *Rev. Sci. Instrum.* **81**, 073303 (2010).

49. Lang, R. F. *et al.* A ^{220}Rn source for the calibration of low-background experiments. *JINST* **11**, P04004 (2016).

50. Marsh, J. W., Thomas, D. J. & Burke, M. High resolution measurements of neutron energy spectra from AmBe and AmB neutron sources. *Nucl. Instrum. Meth. A* **366**, 340 (1995).

51. Lang, R. F. *et al.* Characterization of a deuterium–deuterium plasma fusion neutron generator. *Nucl. Instrum. Meth. A* **879**, 31 (2018).

52. Cooley, J., Lewis, P. & Welch, P. The finite Fourier transform. *IEEE T. Acoust. Speech* **17**, 77 (1969).

53. Harris, F. J. On the Use of Windows for Harmonic Analysis with the Discrete Fourier Transform. *IEEE Proc.* **66**, 51 (1978).

54. Cooley, J., Lewis, P. & Welch, P. The Fast Fourier Transform and Its Applications. *IEEE T. Educ.* **12**, 27 (1969).

55. Aalbers, J. *Dark matter search with XENON1T* PhD thesis (Universiteit van Amsterdam, 2018). https://hdl.handle.net/11245.1/7dbf4ab7-b10a-46f2-a39a-c9daba6d07ad.

56. Aprile, E. *et al.* The XENON100 dark matter experiment. *Astropart. Phys.* **35**, 573 (2012).

57. Aprile, E. *et al.* Light Dark Matter Search with Ionization Signals in XENON1T. *Phys. Rev. Lett.* **123**. doi:10.1103/physrevlett.123.251801 (2019).

58. Ueshima, K. *et al.* Scintillation-only Based Pulse Shape Discrimination for Nuclear and Electron Recoils in Liquid Xenon. *Nucl. Instrum. Meth. A* **659**, 161 (2011).

59. Akerib, D. S. *et al.* Discrimination of electronic recoils from nuclear recoils in two-phase xenon time projection chambers. arXiv: 2004.06304 [physics.ins-det] (2020).

60. Akerib, D. S. *et al.* Liquid xenon scintillation measurements and pulse shape discrimination in the LUX dark matter detector. *Phys. Rev. D* **97**, 112002 (2018).

61. James, F. *Statistical Methods in Experimental Physics* 364 pp. ISBN: 9812705279 (World Scientific Publishing Company, 2006).

62. Hastie, T., Tibshirani, R. & Friedman, J. *The Elements of Statistical Learning* ISBN: 9780387848587 (Springer-Verlag GmbH, 2009).

63. Rebel, B. *et al.* High voltage in noble liquids for high energy physics. *JINST* **9**, T08004 (2014).

64. Cichon, D. *Identifying ^{222}Rn decay chain events in liquid xenon detectors* MA thesis (Ruprecht-Karls-Universität Heidelberg, 2015). doi:10.17617/2.2231457.

65. Bruenner, S. *Mitigation of ^{222}Rn induced background in the XENON1T dark matter experiment* PhD thesis (Ruprecht-Karls-Universität Heidelberg, 2017). doi:10.17617/2.2470353.

66. Rupp, N. *Radon Induced Background in the XENON1T Dark Matter Search Experiment and Studies on Xenon Purity in the HeXe System (working title)* PhD thesis (Ruprecht-Karls-Universität Heidelberg, 2020).

67. Jörg, F. *Investigation of coating-based radon barriers and studies towards their applicability in liquid xenon detectors* MA thesis (Ruprecht-Karls-Universität Heidelberg, 2017). http://hdl.handle.net/21.11116/0000-0002-4440-9.

68. National Instruments. https://www.ni.com/en-us/shop/labview.html. Accessed on 28 April 2020.

69. PostgreSQL Global Development Group. https://www.postgresql.org/. Accessed on 28 April 2020.
70. Nagios Enterprises. https://www.nagios.org. Accessed on 28 April 2020.
71. Jörg, F. *Max-Planck-Institut für Kernphysik (MPIK), Heidelberg* Private communication. 2020.
72. Paschen, F. Über die zum Funkenübergang in Luft, Wasserstoff und Kohlensäure bei verschiedenen Drucken erforderliche Potentialdifferenz. *Annalen Phys.* **273,** 69 (1889).
73. CAEN S.p.A. *V1743 User Manual (revision 2)* (2016). https://www.caen.it/products/v1743/. Accessed on 28 April 2020.
74. Freund, R. W. & Hoppe, R. H. W. *Stoer/Bulirsch: Numerische Mathematik 1* 424 pp. ISBN: 354045389X (Springer Berlin Heidelberg, 2007).
75. Saldanha, R., Grandi, L., Guardincerri, Y. & Wester, T. Model Independent Approach to the Single Photoelectron Calibration of Photomultiplier Tubes. *Nucl. Instrum. Meth. A* **863,** 35 (2017).
76. Bellamy, E. H. *et al.* Absolute calibration and monitoring of a spectrometric channel using a photomultiplier. *Nucl. Instrum. Meth. A* **339,** 468 (1994).
77. Dossi, R., Ianni, A., Ranucci, G. & Smirnov, O. J. Methods for precise photoelectron counting with photomultipliers. *Nucl. Instrum. Meth. A* **451,** 623 (2000).
78. CAEN S.p.A. *WaveCatcher Manual (revision 2)* (2016). https://www.caen.it/products/wavecatcher/. Accessed on 07 November 2020.
79. Maalmi, J. *Laboratoire de l'accélérateur linéaire (LAL), Saclay* Private communication. 2019.
80. COMSOL AB. *COMSOL Multiphysics* https://www.comsol.com. Accessed on 09 November 2020.
81. Agostinelli, S. *et al.* GEANT4–a simulation toolkit. *Nucl. Instrum. Meth. A* **506,** 250 (2003).
82. Cichon, D., Eurin, G., Jörg, F., Marrodán Undagoitia, T. & Rupp, N. Transmission of xenon scintillation light through PTFE. *JINST* **15,** 09 (2020).
83. Keto, J. W., Gleason, R. E. & Soley, F. K. Exciton lifetimes in electron beam excited condensed phases of argon and xenon. *J. Chem. Phys.* **71,** 2676 (1979).

84. Kubota, S., Suzuki, M. & Ruan(Gen), J.-z. Specific-ionization-density effect on the time dependence of luminescence in liquid xenon. *Phys. Rev. B* **21**, 2632 (1980).

85. Kubota, S., Hishida, M., Suzuki, M. & Ruan(Gen), J.-z. Liquid and solid argon, krypton and xenon scintillators. *Nucl. Instrum. Methods* **196**, 101 (1982).

86. Marrodán Undagoitia, T. *Measurement of light emission in organic liquid scintillators and studies towards the search for proton decay in the future large-scale detector LENA* PhD thesis (Technische Universität München, 2008). `http://nbn-resolving.de/urn/resolver.pl?urn:nbn:de:bvb:91-diss-20080725-667813-1-7`.

87. Teymourian, A. *et al.* Characterization of the QUartz Photon Intensifying Detector (QUPID) for Noble Liquid Detectors. *Nucl. Instrum. Meth. A* **654**, 184 (2011).

88. Takiya, H. *et al.* A measurement of the time profile of scintillation induced by low energy gamma-rays in liquid xenon with the XMASS-I detector. *Nucl. Instrum. Meth. A* **834**, 192 (2016).

89. Hogenbirk, E. *et al.* Precision measurements of the scintillation pulse shape for low-energy recoils in liquid xenon. *JINST* **13**, P05016 (2018).

90. Brun, R. & Rademakers, F. ROOT: An object oriented data analysis framework. *Nucl. Instrum. Meth. A* **389** (eds Werlen, M. & Perret-Gallix, D.) 81 (1997).

91. James, F. & Roos, M. Minuit - a system for function minimization and analysis of the parameter errors and correlations. *Comput. Phys. Commun.* **10**, 343 (1975).

92. Aprile, E. *et al.* Intrinsic backgrounds from Rn and Kr in the XENON100 experiment. *Eur. Phys. J. C.* **78**, 132 (2018).

93. Aprile, E. *et al.* Scintillation response of liquid xenon to low energy nuclear recoils. *Phys. Rev. D* **72**, 072006 (2005).

94. Bé, M.-M. *et al. Table of Radionuclides vol. 1-8* `http://www.nucleide.org/DDEP_WG/DDEPdata.htm`. Accessed on 09 November 2020.

95. Grushka, E. Characterization of exponentially modified Gaussian peaks in chromatography. *Anal. Chem.* **44**. PMID: 22324584, 1733 (1972).

96. Chernoff, H. & Lehmann, E. L. The Use of Maximum Likelihood Estimates in χ^2 Tests for Goodness of Fit. *Ann. Math. Statist.* **25**, 579 (1954).

97. Demtröder, W. *Experimentalphysik 3 - Atome, Moleküle und Festkörper* ISBN: 9783642039102 (Springer Berlin Heidelberg, 2010).

98. Seltzer, S. *Stopping-Powers and Range Tables for Electrons, Protons, and Helium Ions, NIST Standard Reference Database 124* en. 1993. doi:10.18434/T4NC7P.

99. Dyson, N. *Chromatographic Integration Methods* 201 pp. ISBN: 0854045104 (Royal Society of Chemistry, 1998).

100. Bruenner, S. *et al.* Radon daughter removal from PTFE surfaces and its application in liquid xenon detectors. arXiv: 2009.08828 [physics.ins-det] (2020).

Acknowledgements

First of all, I would like to thank my supervisor, PD Dr. Teresa Marrodán Undagoitia, for agreeing to provide guidance during my PhD years, lending her scientific knowledge, as well as for her continuous support, patience and helpful suggestions during this time. Without her, neither the realization of HeXe nor this thesis would have been possible. Also, I would like to thank Prof. Dr. Manfred Lindner for having accepted me into his excellent group at MPIK, which could not have been a better setting for my studies, and for giving support especially regarding political matters in science. I also want to express my gratitude to Prof. Dr. Stephanie Hansmann-Menzemer, who agreed to act as a referee for this thesis.

Special thanks go to Dr. Stefan Brünner, Dr. Guillaume Eurin, PD Dr. Teresa Marrodán Undagoitia, Florian Jörg, Natascha Rupp, and Dr. Andrii Terliuk who gave valuable comments to this thesis.

For the good times at MPIK, I would like to thank my colleagues from the Lindner group, especially those from the XENON subgroup, with whom I share many fond experiences. Among those are the people which have formed the core team of HeXe: Dr. Guillaume Eurin, Florian Jörg, and Natascha Rupp. Thanks for building and running the detector together and fighting through all the issues which came along the way, including some crazy nights when either something went wrong during opening and closing the cryostat, or the xenon needed until 3 AM to be recuperated. I also want to thank Dr. Stefan Brünner, Dr. Constanze Hasterok, Luisa Hötzsch, Dr. Daniel Mayani Parás, Veronica Pizzella, Dr. Hardy Simgen, Oliver Wack, Dr. Tim Wolf, and all the other people who have been part of the group during my time there.

Building a xenon TPC from the ground up is a feat which is not possible without technical support. For this reason, I would like to thank Hannes Bonet, Steffen Form, Benjamin Gramlich, Klaus Jänner, Michael Reißfelder, Jonas Westermann, and all other MPIK technicians for their amazing work.

I am also grateful for having been part of the XENON collaboration which allowed me to have many unique and fun experiences, among them analyzing

data and contributing to the dark matter search using one of the most sensitive detectors ever created up to now. Thanks to all current and past members of XENON for making this possible.

Zu guter Letzt möchte ich meinen Freunden sowie meiner Familie dafür danken, dass sie mich die letzten 30 Jahre über immer unterstützt haben. Insbesondere möchte ich hierbei meine Eltern erwähnen, ohne deren bedingungsloser Hilfe das Studium der Physik für mich nicht machbar gewesen wäre.